

**FIRST PRINCIPLES STUDY OF STRUCTURAL, ELECTRONIC AND
MECHANICAL PROPERTIES OF TERNARY Ru-Cr-X ALLOYS**

By

BHILA OLIVER MNISI

Submitted in accordance with the requirements
for the degree of

MASTER OF SCIENCE

In the subject

PHYSICS

at the

UNIVERSITY OF SOUTH AFRICA

SUPERVISOR: DR. M. M. TIBANE

Co-SUPERVISOR: PROF. P.E. NGOEPE

JUNE 2017

DECLARATION

(Student number 5579-223-5)

I declare that the thesis hereby submitted to the University of South Africa, for the degree of Master of Science in Physics is my own original work and has not been submitted before to any institution. Further, I have acknowledged all the resources that I have used.



.....

Bhila Oliver Mnisi

19-02-2018.....

Date

ABSTRACT

We have investigated the effect of doping on the structural, electronic and mechanical properties of A15 RuCr₃ and A15 Ru₃Cr alloys using density functional theory. Various transition metal dopants, namely V, Mn, Fe, Co, Zr, Mo, Pd, Pt and Re were introduced in the 2x2x2 supercells constructed from the optimized unit cells of RuCr₃ and Ru₃Cr binary alloys. The calculated lattice constants for the pure metals, doped and undoped Ru₄₈Cr₁₆ and Cr₄₈Ru₁₆ alloys were determined using the generalized gradient approximation. The results are in overall good agreement with the experimental and previous theoretical data. The relaxed lattice constants for the X doped Ru₄₈Cr₁₆ and Cr₄₈Ru₁₆ structures (X = V, Mn, Fe, Co, Zr, Mo, Pd, Pt and Re) remained the same as the unrelaxed structures because the supercells were produced from the optimized unit cells. All the studied undoped systems were predicted to be unstable, in agreement with the previous theoretical study. Stability of doped Ru₄₈Cr₁₆ and Cr₄₈Ru₁₆ compounds were investigated based on the heats of formation. In general, the Mn, Fe and Mo-doped compositions exhibited negative heats of formation whereas all the remaining dopants displayed positive heats of formation. The addition of Mn, Fe and Mo dopants to the unstable Ru₄₈Cr₁₆ and Cr₄₈Ru₁₆ tuned the heats of formation and enhanced the stability of the systems. The magnetic properties of the pure metals and their ternaries were studied, the metallic Mn was found to have a high-optimized magnetic moment of 5.0 μ B while the optimized magnetic moment for Zr was found to be -0.00059 μ B. Mn and Zr influence Ru-Cr systems to obtain high magnetization and low magnetization respectively. Densities of states were investigated to analyze the nature and stability of the alloys. It was found that all the Mn, Fe and Mo-doped Cr₄₈Ru₁₆ and Ru₄₈Cr₁₆ systems

show full-metallic behavior. Furthermore, the X-doped $\text{Cr}_{48}\text{Ru}_{16}$ compounds ($X = \text{Mn}, \text{Fe}$ and Mo) were found to be more stable than the X-doped $\text{Ru}_{48}\text{Cr}_{16}$ compounds. The observed results are due to Cr rich alloys having low density of states around Fermi energy than Ru rich alloys. This finding is consistent with the heats of formation results. Elastic properties were studied to determine the strength and further analyze the stability of the systems. The ratio of bulk to shear modulus, and Poisson's ratio are greater than 1.75 and 0.3 respectively indicating that the studied X-doped systems are ductile. In addition, the elastic constants revealed that the systems are mechanically stable. The Mn, Fe and Mo-doped $\text{Ru}_{48}\text{Cr}_{16}$ and $\text{Cr}_{48}\text{Ru}_{16}$ could be considered as corrosion resistant materials in high temperature applications.

DEDICATION

This work is dedicated to my family, my mom Mokgadi Mnisi, my brothers (Samora, Lamburg, Aubrey and Nimrod) and my sisters (Angie, Peggy and Rose) who played a huge role in supporting me. I also dedicate this work to my late father Abram Mnisi.

Thank you Mnisi wa pula

ACKNOWLEDGMENTS

I would like to acknowledge my supervisor, **Dr M.M. Tibane** for introducing me to the world of research, the courage and support she has given me throughout this project. My co-supervisor **Prof P. E. Ngoepe** thanks for showing confidence in me.

I would also like to thank **Dr Evans Benecha** for showing interest in my work, and valuable discussions about CASTEP code and its errors, which have been so useful and helpful towards the completion of my thesis. Also, I would like to thank the High Performance Computing (HPC) guys at UNISA **Prof E. Lombardi and Martin Prinsloo**. Many thanks to **Mr Oscar Monama** and his colleagues at the Council for Scientific and Industrial Research (CSIR), the Centre for High Performance Computing (CHPC) for giving me access to use their facilities to perform calculations.

Furthermore, I would like to thank members of the Department of Physics at UNISA for their immeasurable support. Most importantly my sincere appreciation to the National Research Foundation (NRF), Grow Your Own Timber (GYOT) and UNISA Masters and Doctoral Bursary for funding my masters work, and UNISA for giving me permission to study at their institution. Moreover I would like to acknowledge the support from my family, my mom, brothers and sisters who have been with me in paving my way to a brighter future from the beginning to the end of my studies. The encouragement I got from my fiancé Morongwa Bopape throughout the journey make me to be forever grateful.

And above all, I would like to thank the most High God for giving me wisdom, guidance and keeping me healthy to come this far.

THANK YOU ALL

TABLE OF CONTENTS

Chapter	Page
DECLARATION	ii
ABSTRACT.....	iii
DEDICATION	v
ACKNOWLEDGMENTS	vi
TABLE OF CONTENTS.....	viii
LIST OF TABLES.....	x
LIST OF FIGURES	xi
CHAPTER I.....	1
1.1 Overview	1
1.2 Overview of Ni-Al, Pt-Al and Cr-Ru alloys.....	3
1.3 Gas turbine engine.....	7
1.4 Phase diagrams of Pt-Cr, Pt-Ru and Cr-Ru.....	10
1.4.1 The Pt-Cr phase diagram.....	10
1.4.2 The Pt-Ru phase diagram.....	11
1.4.3 The Ru-Cr phase diagram.....	13
1.5 Structural characteristics of pure Pt, Cr, Ru, Fe, Mo, V, Mn and Co metals and their ternary alloys	14
1.5.1 Platinum and its alloys.....	14
1.5.2 Palladium and its alloys	15
1.5.3 Vanadium and its alloys.....	16
1.5.4 Zirconium and its alloys.....	17
1.5.5 Manganese and its alloys	18
1.5.6 Rhenium and its alloys.....	19
1.5.7 Molybdenum and its alloys.....	20
1.5.8 Cobalt and its alloys.....	21
1.5.9 Iron and its alloys.....	21
1.5.10 Chromium and its alloys	22
1.5.11 Ruthenium and its alloys.....	23
1.6 Objectives.....	24
1.7 Outline	25
CHAPTER 2	26
Theoretical methods	26

2.1	Introduction	26
2.2	Overview	26
2.3	Density functional theory	27
2.3.1	Local density approximation (LDA).....	30
2.3.2	Generalized gradient approximation (GGA)	31
2.4	Plane wave pseudo-potential (PWPP) method.....	32
2.4.1	Pseudo-potential (PP) method.....	32
2.4.2	Plane wave (PW) basis.....	34
2.4.3	Cambridge serial total energy package (CASTEP)	36
2.4.4	Heats of formation	36
2.4.5	Brillouin zone sampling.....	37
2.4.6	Periodic boundary condition (PBC).....	38
CHAPTER 3		40
Structural and thermodynamic properties		40
3.1.	Introduction	40
3.2	Structural properties of metallic Ru, Cr and X.....	40
3.3.	Binary and ternary alloys	43
3.3.1	Introduction.....	43
3.3.2	Computation model.....	43
3.3.3	Computational method.....	49
3.3.4	Cutoff energy and k-points convergence	49
3.3.5	Geometry optimization	51
3.3.6	Lattice constants and heats of formation for the A15 RuCr ₃ and Cr ₃ Ru Alloys.....	52
3.3.7	Thermodynamic properties for the doped and undoped Ru ₄₈ Cr ₁₆ and Cr ₄₈ Ru ₁₆ supercells.....	53
3.3.7.1	First-row transition metal doping	55
3.3.7.2	Second-row transition metal doping.....	58
3.3.7.3	Third-row transition metal doping.....	60
3.3.8.	Magnetic Moments	62
3.3.8.1	Magnetic moments of the X-doped Ru ₄₈ Cr ₁₆ system.....	64
3.3.8.2	Magnetic moments of the X-doped Cr ₄₈ Ru ₁₆ system.....	67
CHAPTER 4		71
Electronic properties.....		71
4.1	Introduction	71
4.1.1	Methodology	71
4.1.2	Density of states for pure metals.....	73
4.1.3	Density of states for the undoped Cr ₄₈ Ru ₁₆ and Ru ₄₈ Cr ₁₆ Alloys	81
4.1.4	Density of states for the X- doped Cr ₄₈ Ru ₁₆ and Ru ₄₈ Cr ₁₆ Alloys	83
Chapter 5.....		89
Elastic constants		89
5.1	Introduction	89

5.1.1 Elastic constants of Pure metals and undoped Ru ₄₈ Cr ₁₆ and Cr ₄₈ Ru ₁₆ systems	91
5.1.2 Elastic constants of X-doped Ru ₄₈ Cr ₁₆ and Cr ₄₈ Ru ₁₆ systems	92
5.1.3 Elastic moduli of Pure metals, undoped and six X doped Cr ₄₈ Ru ₁₆ , Ru ₄₈ Cr ₁₆ structures, (X =Fe,Mn and Mo)	94
Chapter 6	98
Conclusion and Recommendations	98
6.1. Conclusion	98
6.2. Recommendation	98
REFERENCES	105

LIST OF TABLES

Table	Page
Table 3.1 : Computed lattice constants, cut-off and total energies for metallic Cr, Ru and X (X = V, Mn, Fe, Co, Zr, Mo, Pd, Re and Pt) Table 3.1: Computed lattice constants, cut-off and total energies for metallic Cr, Ru and X (X = V, Mn, Fe, Co, Zr, Mo, Pd, Re and Pt)	41
Table 3.2 : The atomic positions (Wyckoff notation) in the A15 Ru ₃ Cr and Cr ₃ Ru crystal structures	44
Table 3.3 : Calculated lattice constants and heats of formation of Ru ₃ Cr and Cr ₃ Ru in the A15 phase.....	52
Table 3.4 : Calculated heats of formation of V, Mn, Fe and Co doped Ru ₄₈ Cr ₁₆ and Cr ₄₈ Ru ₁₆ alloys.....	54
Table 3.5 : Calculated heats of formation of Pd, Zr and Mo doped Ru ₄₈ Cr ₁₆ and Cr ₄₈ Ru ₁₆ alloys.....	58
Table 3.6 : Calculated heats of formation of Pt and Re doped Ru ₄₈ Cr ₁₆ and Cr ₄₈ Ru ₁₆ alloys.....	60
Table 3.7 : Effect of smearing width on the magnetic moment (per unit cell) of one Mn doped Cr ₄₈ Ru ₁₆ alloy	63
Table 3.8 : Calculated magnetic moments (per atom) of individual atoms in ternary structures	64
Table 3.9 : Calculated magnetic moments (per unit cell) of X doped Ru ₄₈ Cr ₁₆ alloys....	65
Table 3.10 : Calculated magnetic moments (per unit cell) of X doped Cr ₄₈ Ru ₁₆ alloys...	68
Table 5.1 : Calculated elastic constant C _{ij} in GPa of Pure metals, A15Ru ₃ Cr, A15Cr ₃ Ru and structures doped with Mo ₆ , Mn ₆ and Fe ₆ atoms	91
Table 5.2 : The calculated average bulk (B), shear (G) and young (E) modulus and Poisson's ratio (ν) of Pure metals, Ru ₃ Cr, Cr ₃ Ru system and 2x2x2 supercell of each structure doped with Fe ₆ , Mo ₆ and Mn ₆ atoms	94

LIST OF FIGURES

Figure	Page
Figure 1.1 : A global commercial aircraft turbine engine.....	7
Figure 1.2 : Turbine blade showing holes for cooling.....	8
Figure 1.3 : Phase diagram of Pt-Cr by Oikawa [34]	11
Figure 1.4 : Phase diagram of Ru-Pt.....	12
Figure 1.5 : Phase diagram of Ru-Cr [49].....	13
Figure 1.6 : Pure platinum metal.....	14
Figure 1.7 : Pure palladium metal.....	15
Figure 1.8 : Pure vanadium metal.....	16
Figure 1.9 : Pure zirconium metal.....	17
Figure 1.10 : Pure manganese metal.....	18
Figure 1.11 : Pure rhenium metal	19
Figure 1.12 : Pure molybdenum metal.....	20
Figure 1.13 : Pure cobalt metal.....	21
Figure 1.14 : Pure iron metal	22
Figure 1.15 : Pure chromium metal	22
Figure 1.16 : Pure ruthenium metal	23
Figure 2.1 : Schematic representation of all electron potential (solid line) and pseudo-potential (dotted line) with the corresponding pseudo wave function (ψ_{pseudo}) and the valence wave function (ψ_{v}) [114].....	34
Figure 3.1 : (a) Cr_3Ru structure: atoms are represented by balls of different colours, green (Ru) and grey (Cr), (b) Ru_3Cr structure: green balls (Cr) and grey balls (Ru).	44
Figure 3.2 : Supercell, (a) Bulk $\text{A15Ru}_3\text{Cr}$ unit cell, (b) A $2 \times 2 \times 2$ supercell of $\text{A15Ru}_3\text{Cr}$ and (c) structure of Mn doped into supercell of $\text{A15Ru}_3\text{Cr}$. Blue, light green and gray spheres represent Mn, Ru and Cr respectively.....	46
Figure 3.3 : The schematic diagram of the Ru rich supercells used in the calculations. Each supercell contain 64 atoms (a) $\text{Ru}_{47}\text{MnCr}_{16}$, (b) $\text{Ru}_{46}\text{Mn}_2\text{Cr}_{16}$, (c) $\text{Ru}_{45}\text{Mn}_3\text{Cr}_{16}$, (d) $\text{Ru}_{44}\text{Mn}_4\text{Cr}_{16}$, (e) $\text{Ru}_{43}\text{Mn}_5\text{Cr}_{16}$ and (f) $\text{Ru}_{42}\text{Mn}_6\text{Cr}_{16}$ ternary alloys: Ru, Cr and Mn atoms are represented by green, grey and red balls respectively.	47
Figure 3.4 : The schematic diagram of the Cr rich supercells used in the calculations. Each supercell contain 64 atoms (a) $\text{Cr}_{47}\text{MnRu}_{16}$, (b) $\text{Cr}_{46}\text{Mn}_2\text{Ru}_{16}$, (c) $\text{Cr}_{45}\text{Mn}_3\text{Ru}_{16}$, (d) $\text{Cr}_{44}\text{Mn}_4\text{Ru}_{16}$, (e) $\text{Cr}_{43}\text{Mn}_5\text{Ru}_{16}$ and (f) $\text{Cr}_{42}\text{Mn}_6\text{Ru}_{16}$ ternary alloys: Ru, Cr and Mn atoms are represented by green, grey and red balls respectively.	48
Figure 3.5 : (a) Total energy against cutoff energy and (b) total energy (eV/atom) against the number of k-points for $\text{Ru}_{48}\text{Cr}_{16}$ supercell doped with different concentrations of Mn (substitution of one to six Ru atoms by Mn atoms).....	50
Figure 3.6 : The heats of formation (in eV/atom) against the number of dopants atoms for (a) X-doped $\text{Ru}_{48}\text{Cr}_{16}$ and (b) X-doped $\text{Cr}_{48}\text{Ru}_{16}$	61

Figure 4.1 : Periodic table for transition metals.....	72
Figure 4.2 : The calculated partial and total density of states for metallic Cr. Fermi energy corresponds to the solid line (E_f).....	74
Figure 4.3 : Partial and total density of states (DOS) of pure Ru metal. A solid line shows the Fermi energy (E_f).....	75
Figure 4.4 : Partial and total DOS of pure metallic Mn.....	76
Figure 4.5 : Partial and total density of state (DOS) for metallic Fe. A solid line presents the Fermi energy (E_f).....	78
Figure 4.6 : Total and partial density of states for pure Mo metal. Zero energy corresponds to Fermi energy.....	79
Figure 4.7 : Total and partial DOS of transition metal V. The Fermi energy (E_f) indicates zero energy.....	80
Figure 4.8 : Total and partial DOS for undoped (a) $Ru_{48}Cr_{16}$ and (b) $Cr_{48}Ru_{16}$ structures. The Fermi energy indicates zero energy.....	81
Figure 4.9 : Total and partial density of states for (a) $Ru_{42}Cr_{16}Fe_6$ and (b) $Cr_{42}Ru_{16}Fe_6$ alloys.....	85
Figure 4.10: Total and partial DOS for (a) $Ru_{42}Cr_{16}Mo_6$ and (b) $Cr_{42}Ru_{16}Mo_6$ alloys. A solid line represents the Fermi energy (E_f).....	86
Figure 4.11: The partial and total density of states for (a) $Ru_{42}Cr_{16}Mn_6$ and (b) $Cr_{42}Ru_{16}Mn_6$ alloys. A solid line indicates the Fermi energy.....	87
Figure 4.12: Partial and total density of states for (a) $Ru_{42}Cr_{16}V_6$ and (b) $Cr_{42}Ru_{16}V_6$ alloys. The position of the Fermi level is at 0 eV.....	88

CHAPTER I

Introduction

In this chapter, we give a brief overview of the fundamental theory and experimental work done on transition metals X, to name few Cr, Ru Pt, Zr and Mn, Cr and their alloys. We further give a brief information about the gas turbine engine. The background will provide broader understanding of this research project. The importance of the transition metals and alloys are briefly summarized and lastly we state the objectives and outline of the study.

1.1 Overview

Substantial research based on alloy development has been encouraged due to the huge demand of material capable of withstanding high temperatures in engine industries. The need for high efficiency in gas turbine engines become more important as fuel becomes more costly. The engines are affected by many factors such as high temperature oxidation, hot corrosion [1] and the individual component efficiencies that influence the performance and the overall efficiency of the engine. The development of the new alloys having both the high temperature strength and high temperature corrosion resistant is another area of research that has drawn considerable interest. Transitional metals (TMs) alloys such as platinum, chromium, ruthenium and nickel alloys show a unique number of diverse applications globally and aid as a noble source for the growth in modern theory

of solids [2]. The current materials at solid state displaying high melting points are requested for high temperature structural usages [3].

Gas turbine engines are affected by the environmental threats that decrease the speed of the engines. High-pressure turbine sections obtained in modern gas turbine engine is outlined as one of the most aggressive environments [4-5]. However, when the engine starts to operate just after combustion had took place, and then highly oxidizing gas enters the turbine. Nevertheless, this only happen when the melting point of the super-alloy turbine blade is exceeded by 200°C. This result in the failure of thermal barrier coating in sustaining the temperature and thus cause the blades of the engines to melt [6-7].

Various researchers have studied the properties of binary metal alloys such as hardness, strength and ductility of the materials. The information serves as a guide for selection of suitable high temperature alloys for gas turbine engine applications. Previous study by Tibane M.M et.al [8] computed the heats of formation in the composition of AB, AB₃ and A₃B where A is Ru and B is Cr. The stability study was based on five phases (L₁₂, A₁₅, tP₁₆, DO_C and DO_C') of Ru₃Cr and RuCr₃. In addition, the AB composition with two phases B₂ and L₁₀ were explored. The study predicted positive heats of formation for all the studied Ru-Cr structures, indicating the instability of the studied Ru-Cr binary alloys. The components coated with RuCr can be hazardous for engine industrial usage. However, the computed heats of formation are positive but closer to zero, suggesting the possibility of stability which may be achieved by adding materials to Ru-Cr alloys.

Addition of transition metals (TM) to alloys could enhance the stability of the alloys and improve its strength even at elevated temperatures [9].

1.2 Overview of Ni-Al, Pt-Al and Cr-Ru alloys

This section gives an overview of the binary and ternary alloys consisting of Ni, Pt, Al Ru and Cr materials.

Nickel based super alloys can have cobalt, chromium, rhenium, aluminium and other elements as alloy additions. These alloys serve as an important source to gas turbine engines. The efficiency of the gas turbine engines are influenced by the increase in temperature of the working material where the material's temperature used is limited by its high melting point. The NBSAs have been utilized in the engine industry as blades and vanes since the late 1940's. The good accomplishment of the NBSAs lies to the fact that they possess exceptionally well characteristics of high melting points and resistant in oxidation [10].

The Ni_3Al structure based on the NBSAs is the one that has been studied the most. Furthermore, this alloy has a good ductility in both single and polycrystalline form when their stoichiometry is regulated appropriately. Single crystalline is the material's crystal lattices in the whole samples that is continuous with no grain boundaries and are formed mostly by solidification process, whilst polycrystalline has a columnar grain structure with many grain boundaries that cause defects. Within Ni_3Al , Al is located at the corners and Ni situated on the faces of the cube. Two reasons for choosing to use single

crystalline NBSAs instead polycrystalline NBSAs is that they have a very good creep and fatigue properties [11].

More-over NBSAs are known to have remarkable properties; nowadays 85% of its melting temperature is utilized [10]. In search of possible materials, ceramics were the first candidates to be considered based on niobium, molybdenum and tungsten. In addition, ceramics are suffering from oxidation, creep at low temperatures and lower toughness [12]. In addition, due to the way they are processed it is much expensive than NBSAs.

These NBSAs have superb mechanical properties this is because they have a microstructure that consist of so many small precipitates in a softer matrix. However, NBSAs has a restricted temperature operation to the turbine engines, owing to the melting point of nickel (1543°C) and strengthening dissolution at ~1150°C. This set the current temperature of ~1100°C a limit to NBSAs [13].

This led to the development and study of Pt-based alloys due to their noble corrosion resistance and high melting points. Platinum-based alloys are high in expenditure and display low mechanical resistance at elevated temperatures. In addition, these alloys go hand in hand with the Platinum group metals (PGMs) such as (Platinum, ruthenium, rhodium, osmium, palladium and iridium). These metals are employed in automotive industries as catalysts, in glass manufacturing environment, in spacecraft for increasing the resistance of the rocket engine nozzles.

Platinum based-alloys with their properties can be applied in the chemical industry and can be used as a replacement to Ni super-alloys for high temperature components in the

turbine engines due to having an analogous FCC structure as Nickel. In addition, platinum (1796°C) has high melting point than nickel (1543°C) thus mean platinum has the potential to work better than nickel. Furthermore, during the study of corrosion and oxidation in Pt-based alloys, it was obtained that Pt-based alloys properties are superior to NBSAs [14] however, it is cost effective and high in density but platinum can be recycled as to compensate its expensiveness [15].

In platinum-based alloys, the most studied structure is Pt₃Al. Many researchers had a breakthrough in comparing the Pt-based alloys having high temperature mechanical strength compared with NBSAs. Compounds of L1₂ Pt-based alloys, which are Pt₃Cr, Pt₃Ti, and Pt₃Sn shows a similar temperature dependence of strength whilst the Pt₃Al indicates a normal dependence [15]. The Pt-Al system has been shown to have FCC structure analogous to the NBSAs [16]. This according to Wolff, will aid as the most important candidate for high temperature applications [17].

Furthermore, in checking the oxidation resistance characteristic, researchers obtained that Pt-Al-X ternary system is the best with that property more than the other systems [16, 18]. For Pt-Cr binary, work has been carried out showing that the phase diagrams of the structures were fruitfully analysed. They found that Pt₃Cr is similar to L1₂ AuCu₃ FCC structure and has an ordered cubic A15-type structure occurring at a slightly off-stoichiometric composition of 20 at.%, existing below 1130°C using the energy dispersive X-ray spectroscopy [19].

Later on chromium (Cr) and ruthenium (Ru) had attracted interest to researchers due to their properties of high melting point, oxidation and corrosion resistance. When the Cr

reacts with other conventional materials they form strong alloys making the Cr to have good ductility In addition Cr (1863°C) is high in melting point than Pt (1796°C). However, Cr is easily oxidised and it exhibit a BCC crystal structure that is known to forbid close packing [20]. For (Ru), its interest lies on being an alloying material [21]. The Ru material increases the liquidus and solidus temperatures NBSAs. This property of Ru can be able to recover the temperature capabilities of these materials.

The Cr-Ru system was very deprived owing to being slow in diffusion rate and easy oxidation occurring at Cr when annealed at a particular temperature. This makes it problematic for experimentalists to study Cr-Ru system owing to lack of thermodynamical data of this system [22]. The enthalpy of formation was calculated for Cr_2Ru by Mediema ´s model and found to be -15kJ/mol [23]. The investigation carried on where Ru-Cr binary alloys been studied using the first principle calculations to predict the phase stability based on the structural, thermo-dynamical, elastic, electronic and dynamic properties.

1.3 Gas turbine engine

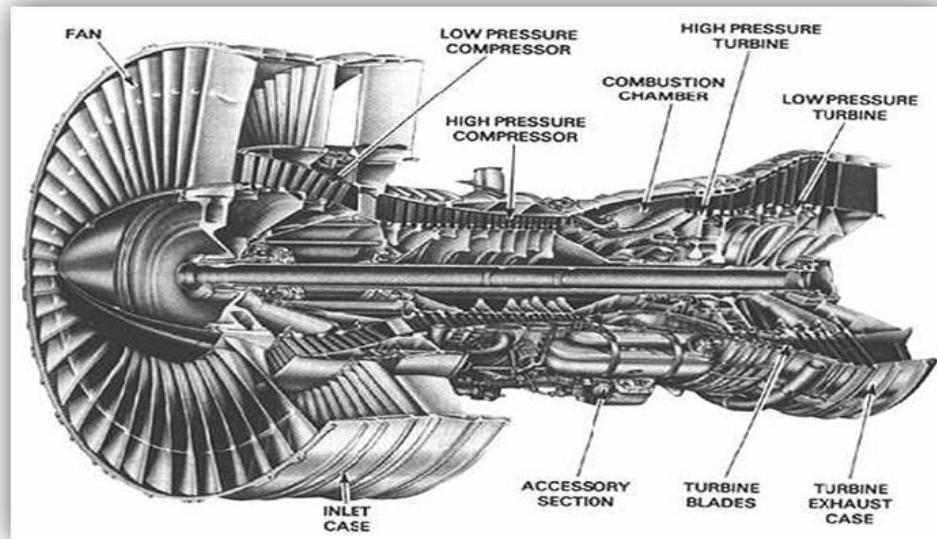


Figure 1.1 : A global commercial aircraft turbine engine

A gas turbine as shown in Figure 1.1 is a type of internal combustion engine that uses air instead of water for cooling. It consists of a shaft, turbine blade, combustor air inlet. The turbine blade is found just after the combustor in the turbine stage. The main role of the combustor is to add energy to the system to power the turbine [24]. In coming to the turbine blade that are responsible for energy extraction from the high temperature and high pressure gas produced by the combustor, normally it consist of three to four rows shown in Figure 1.2 below:-

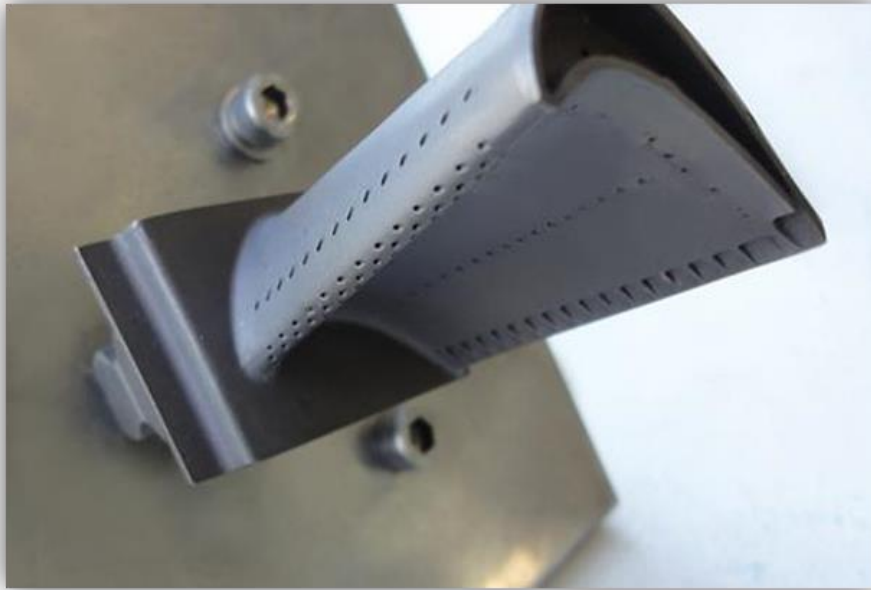


Figure 1.2 : Turbine blade showing holes for cooling

When the hot gas expands from the combustor through the turbine stage it knockout the first row of the blade since it is the one exposed to severe high temperatures coming from the hot gases. However, this first row is the one in need of coating in order for the turbine engine to be efficient. [11].

In designing the turbine engine one has to consider the turbine entry temperature (TET) [25]. This is where the hot gases are entering the turbine arrangement. In addition inside the turbine, the gas stream extracts the temperature that falls as the mechanical work [7]. When offering ways to shield the turbine blades from high temperature gases, thermal barrier coating (TBC) is considered. This coating consists of 4 layers namely: the bond coat, substrate, ceramic top coat and thermally grown oxide (TGO).

The ceramic top coat layer is good for insulating the blade and has low thermal conductivity. This layer is specifically designed to bear thermal cycles. The (TGO) is a type of an oxide that is formed when the bond coat reacts with the ceramic top coat in very high temperatures and it is 1-10 μ m in thickness. The bond coat is well known as a metallic layer containing oxidation resistance characteristic and it is 75-150 μ m. Moreover it is able to grip the ceramic top coat to the substrate. Mostly this layer is built upon nickel and platinum materials.

More advancement in engine materials serves as the important aspects in a progress of a flight or an aircraft. Major interest is on the super-alloys for cooling turbine blade systems and by so doing, the service temperature will meet a 20 $^{\circ}$ C increase and even more. This is because the turbine blades are affected by oxidation and hot corrosion as well [26]. The super-alloys identified were the Nickel based super-alloys owing to its high melting points. However, they are well known as high temperature materials that exhibit unique resistance to mechanical and chemical degradation at temperatures near their melting points [7].

The backgrounds of the jet engine together with the based-alloys are more connected in terms of their developments since the more the based-alloys are improved the more the efficiency of the engines. In the modern generation of aero-aircrafts when they take off, their turbine entry temperature (TET) will exceed 1800K [27]. However, components in the turbine engines are able to withstand this temperature and this is due to the air-cooling them from time to time. More progress has been made in increasing the TETs for the last 40 years [28-29] due to a high demand of power and improved fuel consumption in turbines. In addition, turbine components can be made to operate at high TET by

insulating the metal surface for the metal temperature to be minimized [30]. Furthermore, this formed a basis of the initialization of the thermal barrier coatings [31].

1.4 Phase diagrams of Pt-Cr, Pt-Ru and Cr-Ru

This section gives a brief overview of the Pt-Cr, Pt-Ru and Cr-Ru phase diagrams, and lastly the structural characteristics of the metallic Pt, Cr, Ru, Fe, Mo, V, Mn and Co metals and their ternary alloys

In the previous years, experimental work was a key for improvement and research. However, ways to study the phase diagrams led to the development of alloys [32]. When computational methods became accessible, made the study of phase diagrams to be enhanced employing the method of calculation of phase diagrams (CALPHAD) which had developed by Larry Kaufman [33]. This method is accountable for the formation of databases of many systems like nickel based super-alloys (NBSAs).

1.4.1 The Pt-Cr phase diagram

The Cr-Pt phase diagram in Figure 1.3 displays a broad homogeneity range from ~29 to 100 at.% of Pt solid solution at 1530°C. Waterstrat [35] has found the temperature and composition of the two eutectics. In addition, it has been obtained that Cr₃Pt melts congruently [36]. Recently thermo-calculation method was used to calculate the Cr-Pt phase diagram [37], which was observed to agree very well with the one of Müller [38] and Waterstrat [35] phase diagrams. Moreover, the whole composition range from 50-85 at.% CrPt₃ still remain cubic [35,39-42].

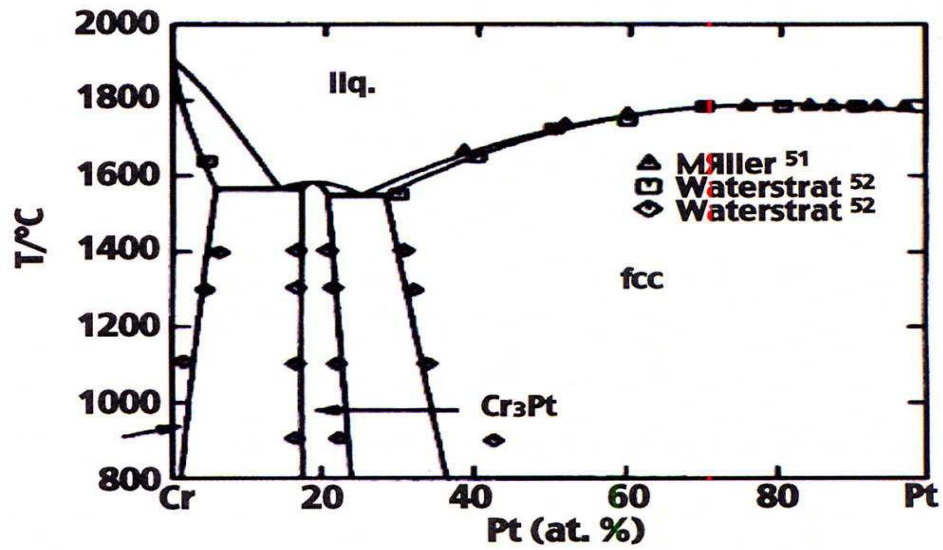


Figure 1.3 : Phase diagram of Pt-Cr by Oikawa [34]

At 1500°C in Massalski's phase diagram shows a Cr-rich side specified on the temperature of the eutectic and Pt-rich side is at 1530°C. However Oikawa's diagram showed that the Cr-rich is probably higher [43]. When Pt is added in small amounts, it increases the Neel temperatures of pure Cr from 311.5 to 440K at 0.6 at.% Pt [44] and 583K at 2at % Pt [45] and 460K at 5at.% pt [46].

1.4.2 The Pt-Ru phase diagram

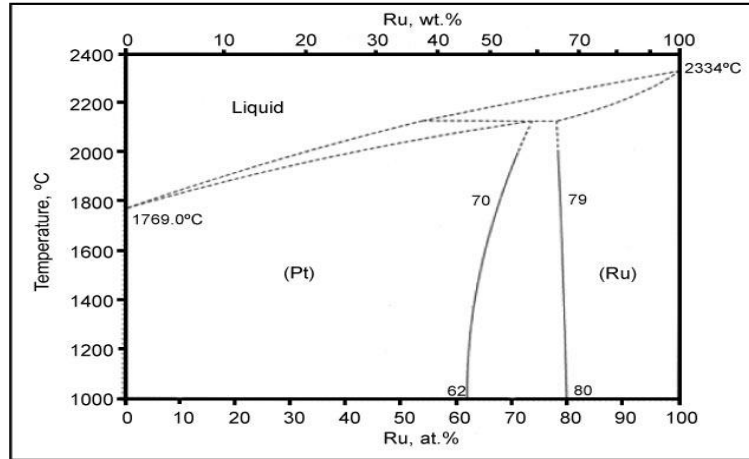


Figure 1.4 : Phase diagram of Ru-Pt

The Pt-Ru phase diagram in Figure 1.4 shows the absence of phases but only the end-member solid solution (Pt) and (Ru). At 1000°C, 62% Ru dissolves in (Pt). In addition a region between ~62 and ~80 at.% Pt shows the existence of two-phase region of (Pt) and (Ru). Moreover at 2120°C a peritectic (a reaction in a phase diagram where the previous precipitates phase react with the liquid to produce new solid phase) reaction occurs and forms Pt while a Ruthenium solid solution at ~80 at.% Pt was observed. However, there is still a limited data on the solidus and liquidus curves. The calculated diagram of Spencer [47] was in good agreement with the ASM diagram [48].

1.4.3. The Ru-Cr phase diagram

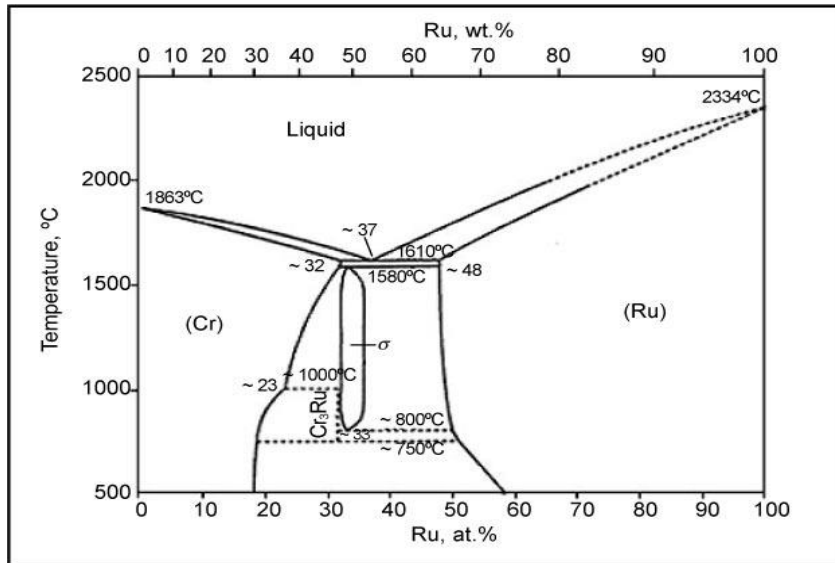


Figure 1.5 : Phase diagram of Ru-Cr [49]

Figure 1.5 present the phase diagram of Ru-Cr. The two intermediate phases of Cr₂Ru (from 32-36 at.% Ru) and Cr₃Ru (from 25±2 at.% Ru) are shown. The metallographic and x-ray diffraction techniques were used to establish this structure. At about 31.5at.% Ru the Cr₃Ru phase exists due to long annealing times that are required to reach equilibrium and a slow kinetics has been shown below 1000°C . Moreover, the phase of Cr₃Ru was found to be stable from 750 to 1000°C [50-55]. A peritectic point of Cr solution is visible at 37% Ru around 1600°C, where the reaction between the previous precipitate and the liquid takes place to form the new solid phase. According to the diagram, at room temperature two or more structures occur from 18 to 58% of Ru concentration. However, the liquidus and solidus curves of Cr-Ru are based on the work of Shurin AK [56-57]. The Cr-Ru

system is very challenging to investigate due to slow diffusion that grade from its large atoms and high melting point.

The Massalski phase diagram [49] was found to be similar to the one of Shunk [58] and it is built on the microstructural development of Ru-Cr alloys. The existence of Cr_3Ru into the Cr-Ru phase diagram can be explained by the inhomogeneity cause when heat treatment and solidification occur and solid solution data [49] were the α -chromium and RuCr_3 occur. This is due to the formation of grain boundaries from the precipitates. All of these happen when the volume fraction of the Cr_3Ru increase with increasing Ru content [59].

1.5 Structural characteristics of pure Pt, Cr, Ru, Fe, Mo, V, Mn and Co metals and their ternary alloys

1.5.1 Platinum and its alloys



Figure 1.6 : Pure platinum metal

Platinum is a metal that belongs to the platinum group minerals (PGMs) and it is the third highest in density within that group. It is silvery-white in colour, ductile and malleable

[60]. This metal is highly resistant to corrosion and oxidation when subjected to high temperatures [61]. However, platinum is a rare metal in the earth's crust and occurs with copper and nickel ores in the same chemical deposit. In addition, this metal possesses a face centred cubic crystal structure [62]. In addition Pt has elastic properties as follows: Young's modulus = 168 GPa, Shear modulus = 61 GPa, Bulk modulus = 230 GPa, Poisson ratio = 0.38, Mohs hardness = 4-4.5 [62-63].

This material is applied in various ways in the industry, like making jewellery due to its high resistance to tarnish, in the automotive industries being used as catalysts, in glass manufacturing environment and in spacecraft for increasing the resistance of the rocket engine nozzles. Platinum alloys are usually applied to gas turbine engines [64, 19].

1.5.2 Palladium and its alloys



Figure 1.7 : Pure palladium metal

Palladium (Pd) is a chemical element forming part of the platinum group minerals (PGMs) which are Ruthenium, Osmium, Iridium, Platinum and Rhodium. However Pd is

a very scarce metal with low melting point as compared with the other PGMs. Palladium tend to occur not mixed with the other metal. In addition, it has an FCC structure just like platinum [64]. This element is applied extensively in the automotive industry as the catalytic converters in vehicles [65], furthermore, it is also used as medicine especially in dentistry and plays a major role in manufacturing of LCD television screens, computer, ceramic capacitors and cell phones [66]. Palladium is normally alloyed with Gold, Copper and Silver. These alloys can be used as ball bearing, springs, surgical instruments and electrical contacts. Meanwhile ruthenium when added to palladium it acts as a solid strengthener [67].

1.5.3 Vanadium and its alloys



Figure 1.8 : Pure vanadium metal

Vanadium is a transitional metal that is hard, silvery grey, malleable and ductile. It is found in combined form of chemicals naturally. It occurs in 65 different minerals and fossil fuel deposits [68-69]. This metal possesses a base centred cubic structure similarly

to chromium. In addition, vanadium in steel can be applied in axles, bicycle frames and gears. The Vanadium metal has advantage being recycled and reused. Major uses of vanadium are when it acts as an alloy. Vanadium has high melting point thus mean when added to other material can form relatively high strength at elevated temperatures, good fabric-ability and lastly a good corrosion resistant alloy. Furthermore this metal forms a solid solution with Cr more than other materials therefore it has the most potential to ductilize Cr when used as an alloying agent [70-71]. The vanadium metal can act as materials for fusion blanket systems like coating and welding [72].

1.5.4 Zirconium and its alloys



Figure 1.9 : Pure zirconium metal

Zirconium is a chemical element that is grey-white, lustrous and robust transitional metal. This metal is highly resistant to corrosion and it has a high melting point. In addition it is found in a silicate mineral iron ($ZrSiO_4$) and has a 130kg concentration within the earth's crust. Zirconium alloys shows extra-ordinary properties like high melting temperature,

high thermal, electrical conductivity and hardness. Furthermore, because of zirconium alloys properties they become very essential in the high temperature applications [73-75]. Zirconium material possess two phases of different crystal structure: when the temperature is below 860°C it has an α phase characterized by hexagonal close packed (HCP) and when the temperature is above 860°C it has a β phase of a base centred cubic (BCC) [76]. This material is compound forming with Rhenium alloys [77].

1.5.5 Manganese and its alloys



Figure 1.10 : Pure manganese metal

Manganese is a chemical element that is pinkish-grey transitional metal. When manganese is exposed to heat and air it tarnishes. This material is found in substantial ores were one of it is manganese dioxide in the form of pyrolusite. In addition manganese is applied in dry cell batteries as a filler and brown/black pigment in paints. In the earth's crust manganese is the 12th most abundant and it has the low melting point compared to the material discussed above. Furthermore, it possesses a BCC crystal structure and has

the potential to produce many alloys. When manganese is added to ferrite compound it raises its strength and the hardness of steel [78-79].

1.5.6 Rhenium and its alloys



Figure 1.11 : Pure rhenium metal

Rhenium is a chemical element having the highest melting point. This material however is applied as catalysts due to its high resistance to chemical poisoning and mostly in turbine blades as nickel-based super-alloys for high temperature applications and occur as a by-product of copper and molybdenum ore's extraction. In addition, Rhenium possesses a hexagonal close packed (hcp) crystal structure and it has a paramagnetic ordering [80-82]. In adding Rhenium to alloys, has played an important role as to improve the high temperature properties. [83]. Furthermore, when Rhenium is added to NI-Cr-Al alloy is has stabilizing effect to spheroidal morphology of the γ' precipitates [84]. Few percentage of Rhenium to nickel-based super-alloys recovers the strength properties of

the alloy and has a Rhenium effect, meaning there is a simultaneous increase in plasticity and strength of the metal [77].

1.5.7 Molybdenum and its alloys



Figure 1.12 : Pure molybdenum metal

Molybdenum (Mo) is a chemical element that has the sixth-highest melting point of any element. In addition, Mo readily forms stable and hard carbides in alloys and appears as a by-product of tungsten and copper mining. Moreover, it is used as alloys for stainless steel and has the ability to withstand the extreme temperatures without expanding or softening. Mo is used in steel alloys due to its high corrosion resistance and weldability. When Mo is added to Rhenium system, a specific configuration phase was obtained to be stable at low temperatures [77]. This material has a BCC crystal structure and possesses a paramagnetic ordering [85-87].

1.5.8 Cobalt and its alloys



Figure 1.13 : Pure cobalt metal

Cobalt (Co) is a chemical element that has an oxidation resistant characteristic because of passivating oxide film it is having. This material is produced as a by-product of copper and nickel mining [88]. In alloy application, Co is used as a metal in preparing magnetic, wear-resistant and high strength alloys. Moreover Co possesses a ferromagnetic ordering that occurs at two crystallographic structures: which are HCP and FCC and the difference between the two states is the transition temperature structure is 450 °C [89]. Furthermore, Cobalt as alloy is predicted to improve the workability of super-alloys [90].

1.5.9 Iron and its alloys

Iron (Fe) is a chemical element that is soft, low cost and high strength. In the earth's crust Fe is the fourth common element. Furthermore, it is very important when mixed with other metals forming alloys used in steel formation for cutlery. In addition, it is applicable

in the construction of hulls of ships.



Figure 1.14 : Pure iron metal

This material undergoes a phase change from bcc to FCC in the temperature from 912°C to 1400°C and it is a ferromagnetic material in nature [91-92]. The magnetic properties of iron being added to rhenium were studied and found that the predicted ground state shown reduced magnetic moments as compared with the pure elements [77].

1.5.10 Chromium and its alloys



Figure 1.15 : Pure chromium metal

Chromium is a chemical element which is hard, lustrous and brittle. It has an average concentration of 100ppm and it is the 22nd most abundant element in the earth's crust. This element has a high melting point of 1863°C. In addition this characteristic helps the element to resist corrosion and hardness. Chromium metals possess antiferromagnetic ordering at room temperature and below. Furthermore, it has a BCC crystal structure and does not allow atoms to pack together closely. The BCC unit cell has a close packing of 0.68 [93]. This material when added to manganese it enhances the hardness of steel. In addition, when 5% of chromium or more is mixed with manganese makes the steel to be air hardening by decreasing the quenching speed. In heat application, steel with chromium possess high critical temperatures [94-97].

1.5.11 Ruthenium and its alloys



Figure 1.16 : Pure ruthenium metal

Ruthenium is a chemical element belonging to the platinum group minerals in the periodic table. It is a rare metal and it is mostly abundant element in the earth's crust. This element is inert to most other elements. Ruthenium is used mostly for wear resistant electrical contacts and as an alloying agent to Pd and Pt in metallurgical industry for high temperature application. Ruthenium is also used in in the production of dental alloys as coating for oxidation resistance. In addition, this element has HCP crystal structure with a melting point between 2300°C and 2450°C. The magnetic ordering of Ruthenium is paramagnetic [98].

1.6 Objectives

In this thesis, we investigate the effect of transition metal dopants on the stability of previously studied RuCr_3 and Cr_3Ru alloys. The primary objective of this work is to search for beneficial dopants that could enhance the stability of the alloy coatings that are used to cover the gas turbine engines that are operating at high temperatures. The fundamental physical properties of transition metal ternary alloys are not fully explored. The discovered ternaries may improve the environmental threats that are encountered by the engines. A stable coating for a gas turbine engine is required to reduce hot corrosion and oxidation. To meet the objectives of this work we investigate the effect of dopants on the structural, electronic and mechanical properties of the A15 RuCr_3 and A15 Cr_3Ru alloys. We will consider the following dopants: Zr, Mn, V, Mo, Pt, Pd, Co, Fe and Re. We will predict the stability based on the heats of formation of Ru-Cr-X (where X

represent the dopant). In addition, we will also predict stability based on the electronic properties and elastic properties. We will compute the elastic constants (C_{11} , C_{12} and C_{44}), elastic moduli, ratio of the bulk/shear modulus (B/G), as a proxy for ductility. All the calculation will be carried out using the density functional theory within the generalized gradient approximation and plane wave pseudo-potentials. We will employ the Cambridge serial total energy package (CASTEP) code for calculations and compare with the previous results.

1.7 Outline

This work consists of six chapters: In chapter one, we outline a brief introduction of Ni and Pt and their application. Moreover gives the theory of Ru-Cr, Pt-Cr, Pt-Ru alloys and their phase diagrams. Furthermore, the dopants used are described in this work individually. Chapter 2 outlines the methodology used in the current study. The density functional theory is used, were the plane wave pseudopotentials, generalized gradient approximation (GGA), local density approximation (LDA) and CASTEP software are analysed in order for the prediction of electronic, structural, elastic and mechanical properties. In Chapter 3 we present the results from the CASTEP software in the form of tables and graphs of lattice constants, heats of formation and magnetic moments. In chapter 4 the total density of states (DOS) and partial density of states (DOS) are analysed. More-over chapter 5 discuss the calculations of elastic constants. The results obtained will be compared with previous experimental and theoretical work. Chapter 6 summarize the whole work; give a conclusion and future work for the study. And lastly, the references used in the study.

CHAPTER 2

Theoretical methods

2.1 Introduction

In this chapter, we outline the ab-initio methods used in this study. The investigation in this thesis is based on the density functional theory (DFT) in a plane-wave pseudopotential framework. The Cambridge Serial Total Energy Package (CASTEP) [99] computational scheme was used to perform the calculations. CASTEP employs the DFT plane-wave pseudopotential methods, which perform first-principle quantum mechanics calculations that explore the properties of crystals and surfaces in various materials such as metals, minerals, semiconductors and ceramics. We will briefly outline the computational simulation using the ab-initio methods. We will further discuss the DFT, which predicts the ground state energy that is essential to predict the structural, magnetic and electronic properties in a vast class of materials.

2.2 Overview

Computer simulation techniques will be used to model our structures of interest and this will help to investigate properties of materials. The simulator inside the computer will model the real system and study the system's behaviour and all this is done on the computer. This theoretical study is accurate and it is comparable with the experimental work. Moreover the wide most used technique is the ab initio method.

Ab initio on its own has a group of methods that tackle lots of properties like lattice parameter and band structures. The methods are Density Functional Theory (DFT), Car-Parinello ab initio Molecular Dynamics, Semi-Empirical methods and Hatree-Fock method. However, we will focus more on Density Functional theory because it is cheap and easy to use.

2.3 Density functional theory

Density functional theory (DFT) was born in 1960 under the invention of Kohn and Hohenburg and Kohn and Sham [100] in freezing the electron-electron interaction in a system. This is a theory well known to connect the ground state properties to the charge density. In addition, density functional theory reduces the strong interactions like complex electron-electron system and when the atomic nuclei are present, it maps it onto a single particle moving in an effective non-local potential.

Furthermore in DFT Hohenberg-Kohn verified that the total energy of many-electron system in an external potential is a distinctive functional of the electron density for a given location of an atomic nuclei. The ground state energy is outlined as the minimum value of the total energy functional on the system; additionally the density that produces this minimum value is the precise ground state density. Moreover the total energy is expressed as

$$E = E[\rho_o(r), R_\alpha(r)] \tag{2.1}$$

Where E is the total energy depending on the type of organisation of the atomic nuclei, R_α denotes the positions of the nuclei in the system and $\rho_o(r)$ is the electron density. This equation forms a wide array of essential tools for structural, electronic and magnetic properties at an atomic-scale. The Hohenberg-Kohn theorem outlines the possibility in applying the ground state density for the calculation of properties for a system; however, it does not grant a way to find the ground state energy. Then Kohn-Sham equations saw a path that can address the situation [101] by introducing different type of wave functions of single particle orbitals for the treatment of interaction and kinetic energy. The total energy equation (2.1), can be written by expressing the functional in terms of three terms as follows:

$$E[\rho] = T_o[\rho] + U[\rho] + E_{xc}[\rho] \quad (2.2)$$

The symbol T_o displays the sum of the kinetic energies of all independent particles, $U[\rho]$ is the classical coulomb energy having the electrostatic energy from the columbic attraction and $E_{xc}[\rho]$ is the exchange correlation energy responsible of the remaining complicated electronic contribution to the total energy. Density functional theory substitutes the real electrons by the effective electrons having similar mass, density distribution and charge. The effective electrons are independent when moving inside the effective potential however there is a correlation between the real and the effective electrons. More over when the effective electron is described by the single particle wave function ψ_i its kinetic energy will be as follows

$$T_o = \sum n_i \int \psi_i^*(r) \left[-\frac{\hbar^2}{2m} \nabla^2 \right] \psi_i(r) dr \quad (2.3)$$

The number of electrons in state i is denoted by n_i and ∇^2 is the gradient operator, $\psi_i(r)$ is the wave function describing the independent particles and. The coulomb energy that is classical having the electrostatic energy coming from the columbic attraction can be show below as.

$$U[\rho] = U_{en}[\rho] + U_{ee}[\rho] + U[\rho]_{ion-ion} \quad (2.4)$$

Where $U_{en}[\rho]$ are the columbic attraction nuclei and electrons, $U[\rho]_{ion-ion}$ the repulsion between the nuclei and classical repulsion between the electrons and $U_{ee}[\rho]$ which is the columbic electron-electron repulsion. However, Kohn-Sham energy functional can be minimized by a set of wave functions given by an equation below

$$\left[-\frac{\hbar^2}{2m} \nabla^2 + V_{ion}(r) + V_H(r) + V_{XC}(r) \right] \psi_i(r) = \varepsilon_i \psi_i(r) \quad (2.5)$$

Where ε_i shows the Kohn-Sham's eigenvalue, V_{ion} is the total spatial electron-ion potential, ψ_i is the wave function of a state i and V_H as the Hatree-fock potential which can be given as

$$V_H(r) = e^2 \int \frac{\rho(r')}{|r-r'|} dr' \quad (2.6)$$

Whilst the exchange-correlation potential, V_{XC} is given by the functional derivative shown below

$$V_{xc}(r) = \frac{\delta E_{xc}[\rho(r)]}{\delta \rho(r)} \quad (2.7)$$

Where $\rho(r)$ is the electron density and can be given by

$$\rho(r) = 2 \sum |\psi_i(r)|^2 \quad (2.8)$$

Hence, the total Kohn-Sham total energy functional is given by

$$E = 2 \sum_{occ} \varepsilon_i + U_{ion-ion} - \frac{e^2}{2} \iint \frac{\rho(r)\rho(r')}{|r-r'|} dr dr' + E_{xc}[\rho(r)] - \int \rho(r) V_{xc} dr \quad (2.9)$$

However still the exchange correlation remains to be unknown but it can be solved in applying the approximation method that follows below.

2.3.1 Local density approximation (LDA)

Many schemes have been established in order to approximate the exchange-correlation energy. Local density approximation is the easiest approach in explaining the exchange correlation energy of an electronic system. This approach can be applied in pseudo-potential calculations for total-energy of the system [102-103]. LDA assumes that the exchange-correlation energy rely only on the local electron density around each volume element dr given and can be expressed as

$$E_{xc}[\rho] \approx \int \rho(r) \varepsilon_{xc}[\rho(r)] dr \quad (2.10)$$

Main emphases of LDA is that in any crystal, a surface or a molecule having an atomic arrangement consist of an electron density $\rho(r)$ at each point r in space. The Local

Density Approximation (LDA) when it comes to the results for slow varying density systems like; nearly-free-electron metals it is more accurate and in addition it communicates nicely with semiconductors and insulators. However, LDA in strong correlated systems where independent particle picture is not considered it produces inaccurate results and moreover the LDA with regard to the ground state energy and bulk modulus it obtains wrong values due to the bond lengths and lattice constants being underestimated [104]. Moreover, as for band gap values for these systems is less estimated as compared to the experimental work available [105]. To increase the accuracy of the result in LDA the GGA approximation comes into play and it is discussed below.

2.3.2 Generalized gradient approximation (GGA)

Generalized gradient approximation for Exchange functional having accurate expressions in DFT involves many applications globally [106-109]. This approximation advances the lacking in Local Density Approximation (LDA). The Generalized Gradient Approximation (GGA) takes care of the exchange-correlation energy density, consisting of density $\rho(\mathbf{r})$ and its gradient $\nabla\rho(\mathbf{r})$, whilst the local density approximation depends on the electron density. The GGA-functional uses Perdew and Wang (PW91) [110]. In this work we have used the PBE form of the GGA. Moreover GGA outlines more accuracy of the ground state energies, bulk modulus and band gap values than the Local Density Approximation (LDA), however it has some drawbacks as well which needs to be looked at for more improvement. The GGA exchange correlation energy is given as follows:

$$E_x^{GGA} C(n) = \int dr \rho(r) \varepsilon_{xc}^{GGA} [\rho(r), \|\nabla \rho(r)\|] \quad (2.11)$$

The symbol ε_{xc} is the exchange correlation energy and $\nabla \rho(r)$ is the gradient term.

2.4 Plane wave pseudo-potential (PWPP) method

Plane-wave pseudo-potential method has attained a lot of attention in studying many properties of materials globally. The method tends to make DFT simple by working only with the valence electrons under the assumption that there is no effect in chemical changes to their charge density.

2.4.1 Pseudo-potential (PP) method

Electrons in matter are differentiated into two ways: those further away from the nucleus are the valence electrons and those that are closer to the nucleus are core electrons. The localization of the core electrons in closed inner atomic shells are very strong [111], more-over DFT wave functions best describes the features of core electrons showing more oscillation in the core state than the valence electrons in the valence state. This result is because of the orthogonal requirement. Plane wave set are normally needed for the description of the core regions, however this might be costly and computationally challenging.

The Kohn-Sham equations are used in the pseudo-potential approach for solving only valence electrons whilst the scattering potential from the core are described at a particular radius by pseudo-potential. In addition, this minimizes the total number of wave functions to be calculated, and will put more emphases on valence electrons calculations.

The full wave function close to the nuclei tends to lose data when the core electrons are treated by pseudo-potential. This might influence negatively other properties. i.e. the electric field gradient [112].

In solid state physics, electronic state near the Fermi level is related with the properties in question. However, most of the properties are mostly dominated by valence electrons. This bring to our attention that the core states and the core orbitals are generally irrelevant for the properties of interest and thus means that they can be disregarded or substituted. So the main task of the PP approach is to substitute the strong interaction potential that has core electrons that are bounded tightly with much weak effective potential [113]. Moreover, the PP must have similar scattering properties to the original potential in a core region. Furthermore, this PP does not have nodes since it is a smooth pseudo-wave function. Figure 2.1 below of the pseudo-potential and the true potential is shown.

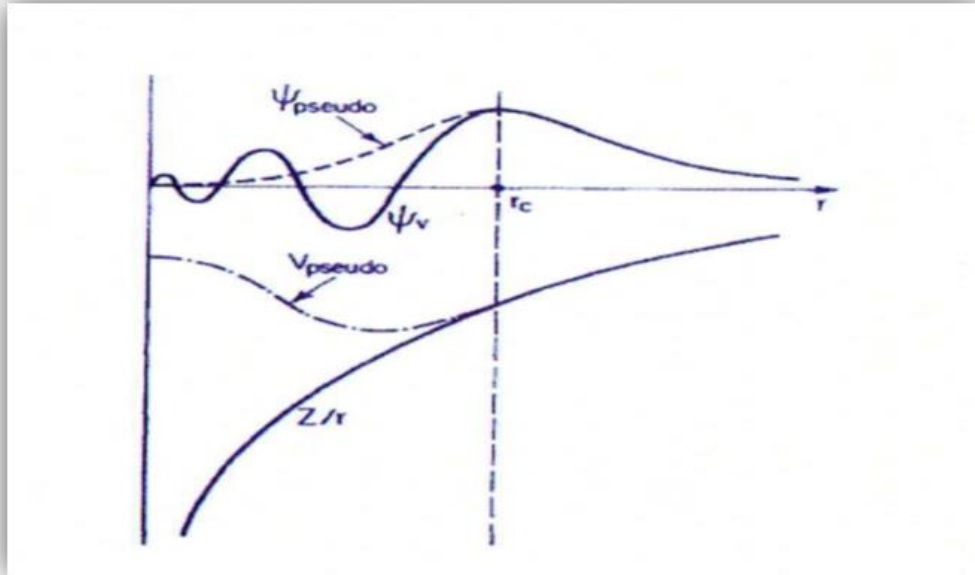


Figure 2.1 : Schematic representation of all electron potential (solid line) and pseudo-potential (dotted line) with the corresponding pseudo wave function (ψ_{pseudo}) and the valence wave function (ψ_v) [114]

The PP is drawn presenting the similar phase shifts between the pseudo wave functions and the ion and core electrons for the valence wave function. Furthermore, the total phase shift produced by the core electrons and the ion is π greater for each node contained in the core region by valence functions, than the production of phase shift by valence and ion electrons. Whilst on the outer side of the core region there is a similarity of two potentials and the scattering from the two potential cannot be distinguished.

2.4.2 Plane wave (PW) basis

Orbitals can be defined by the plane waves (PW) or linear combination of atomic orbitals (LCAO). The PW method has an exponential function as

$$\eta^{PW} = e^{\overline{ikr}} \quad (2.12)$$

Where \vec{k} represents the wave vector and is related to the electron 's momentum. However, these functions are scattered across space and are not based around the nucleus. These functions need the periodic boundary conditions in order to calculate the infinite periodic systems well and cheap. The PW basis set uses an infinite, continuous basis set in expanding the electronic wave functions of the system. In addition, this method is best described by Bloch 's theorem stating that: the discrete PW basis set can expand the electronic wave function at each k-point by the following expression:

$$\psi_{ki}(r) = e^{ik \cdot r} f_i(r) \quad (2.13)$$

Where $f_i(r)$ is a function that describes how periodic a solid is. However, the equation (3.8) contains two parts namely: the wavelike and the cell-periodic part. More-over $f_i(r)$ can be written as

$$f_i(r) = \sum_G C_{i,G} e^{iGr} \quad (2.14)$$

The symbol G displays the reciprocal lattice vectors of the periodic cell. In addition, each electronic wave function can be written as the summation of PW as follows below

$$\psi_{ki}(r) = \sum_G C_{i,k+G} e^{i(k+G) \cdot r} \quad (2.15)$$

$C_{i,k+G}$ represents the coefficients of the PW which are set to be unknowns. This rely more

to kinetic energy that is definite and can be outlined as $\left[\frac{\hbar^2}{2m} \right] |K + G|^2$

For the expansion of the PW to converge it relies on the energy cut-off. In addition, the energy cut-off produces a finite set when introduced by the discrete PW basis set. In this work, we use plane-wave pseudopotential code that will be discussed in the next section.

2.4.3 Cambridge serial total energy package (CASTEP)

CASTEP code [99] is a package used in performing the DFT calculations, and has the ability to simulate interfaces, solids and surfaces for a wide range of materials such as semiconductors, ceramics, metals etc. This code deals with the weak pseudo-potential for materials by using the plane wave (PW) method. First principle calculation can simulate lot of properties like optical, electronic and mechanical that have assembly of electrons and nuclei within the DFT formalism; in addition, it does not need experimental input. CASTEP is well known to tackle problems in engineering, chemistry, material science and solid state. It is able to calculate the stresses, the forces of an atom in a unit cell taking place and heats of formation that is to be discussed below. However, CASTEP also has limitations that are associated with LDA i.e the underestimation of band gaps in insulators.

2.4.4 Heats of formation

Heat of formation is the change in enthalpy from the formation of 1mole of the compound from its constituent elements with all substances in their standard states at 1 atmosphere. The heats of formation can be illustrated by the following equation:

$$\Delta H_f = E_{AxByCz} - xE_A - yE_B - ZE_C \quad (2.16)$$

Where for a given lattice (bcc, fcc and hcp), E_A , E_B , E_C and $E_{A_xB_yC_z}$ are the equilibrium total energy of constituent elements A , B , C and compound ($A_xB_yC_z$). Atomic concentration A , B and C are highlighted by x , y and z . The lower the heat of formation, the more stable the structure becomes. Heats of formation are able to approximate stability of phases which are not obtainable experimentally and offer ways to envisage phase diagrams. Based on the ab-initio calculations, heats of formation have been an accomplishment in predicting the stability of alloys and paving a good way in the construction of phase diagrams [115-118]. Hence investigating the relative stability of binary, ternary or quaternary alloys, considering the formation energy for individual structures may be the best way to tackle alloys. The results of the heats of formation for the studied crystal structures will be discussed in detail in the subsequent chapter.

2.4.5 Brillouin zone sampling

The average or the mean of the Brillouin zone [119] in a particular wave-vector's periodic function involves many crystal calculations known to be complex and difficult. The Brillouin zone sampling approach uses the finite number of k -points that contains small errors in the wave-function and it applies the Hamiltonian's eigenvalue for small changes of k [120]. The first Brillouin zone contains infinite k -points and for an infinite system there exist a finite number of occupied eigenstates of the Hamiltonian for each k -point. This scheme was initialized by Monkhorst Pack [121] based on a principle of metal

system needing a very fine k-point sampling unlike the semiconductors which require few k-points. The primitive reciprocal lattice vector k can be written with respect to the set of vectors q as

$$K = n_1b_1 + n_2b_2 + n_3b_3 \quad (2.17)$$

Where b_1, b_2, b_3 are the reciprocal lattice vectors and n_i are integers defined by the following expression:

$$n_i = \frac{(2r - q - 1)}{2q} \quad r = 1, 2, 3, \dots, q \quad (2.18)$$

These k-points play a major role in the electronic potential on the bulk solids. To obtain accurate results, the wave functions are supposed to be calculated in all the k-points in the brillioun zone. In principle, the electron wave-functions remain constant when a small change in the k-point space distance occur [111]. When calculation are performed with the finite, mesh of the k-points gives inaccurate results [122] that is why firstly the set of k-points must be determined by the position of the k-points and the shape of the brillioun zone in order to calculate only the electronic states of a material in question [123-124].

2.4.6 Periodic boundary condition (PBC)

The PBC are mainly used in molecular dynamics simulation to avoid problems with boundary effects caused by finite size. Surface effects are being tackled by the PBC, however in this investigation we are not interested with the surface effects. The applied simulation being used in this investigation will be for small number of particles. In the PBC approach the particles are enclosed in a box and there is a replication to infinity by rigid translation in all three Cartesian directions which fills the space completely. When

one of the particles is located at a point \mathbf{r} in the box, this can be assumed that this particle really represents an infinite set of particles located at

$$\mathbf{r} = l\mathbf{a} + m\mathbf{b} + n\mathbf{c} \quad (2.19)$$

Where l, m, n are integers and $\mathbf{a}, \mathbf{b}, \mathbf{c}$ are vectors that correspond to the edges of the box. The key point is that in the box each particle i are thought as interacting with their images in nearby boxes together with other particles j in the box and thus means interactions can go through box boundaries. In fact now the surface effects from the system are eliminated.

CHAPTER 3

Structural and thermodynamic properties

3.1. Introduction

In this chapter we present the structural properties of the Ru, Cr, undoped and transition metal doped A15 Ru_3Cr and Cr_3Ru alloys obtained by using computational methods that are outlined in chapter 2. The computed lattice constants of the Ru, Cr, their binary and ternary alloys Ru-Cr-X are compared with the available experimental and theoretical data. In addition, we present the lattice constants of the studied dopants. We also discuss the heats of formation and the magnetic moments of the binary and ternary alloys. We analyse the effect of dopants on lattice constants and heats of formation of $\text{Ru}_{48}\text{Cr}_{16}$ and $\text{Cr}_{48}\text{Ru}_{16}$ alloys.

3.2 Structural properties of metallic Ru, Cr and X

Density functional theory is well known to define the ground state properties of metals accurately. The ground state structures of Ru, Cr and the dopants X (X = V, Mn, Fe, Co, Zr, Mo, Pd, Re and Pt) were computed by using the self-consistent DFT calculations. The energy cut-off convergence for the plane-wave expansion of the wave function; and k-points convergence for the number of k-points to sample the k-space in the plane wave expansion are considered to make DFT calculations more accurate.

Table 3.1 : Computed lattice constants, cut-off and total energies for metallic Cr, Ru and X (X = V, Mn, Fe, Co, Zr, Mo, Pd, Re and Pt)

Metal	Lattice constants a (Å)			E _{cut-off} (eV)	E _{Total} (eV)	
	LDA	GGA	Exp		LDA	GGA
Cr	2.791	2.850	2.884[127]	600	-2465.381	-2467.739
Ru	2.681	2.726	2.706[128]	600	-2604.726	-2602.167
V	2.544	2.600	-	600	-1976.151	-1976.512
Mn	7.718	7.718	-	1100	-639.285	-645.083
Fe	2.328	2.379	2.866[129]	1100	-859.958	-864.896
Co	2.454	2.477	2.507[130]	1000	-1038.615	-1042.898
Zr	3.143	3.229	-	1600	-1282.935	-1281.093
Mo	2.701	2,734	-	600	-1935.303	-1936.899
Pd	2.714	2.781	-	600	-800.640	-798.763
Re	2.735	2.774	-	1500	-2464.955	-2459.620
Pt	2.771	2.826	3.924[131]	600	-721.127	-718.170

In order to determine the appropriate energy cut-off for Ru, Cr and X, we performed single energy calculations where we kept the k-points fixed while varying the plane-wave energy cut-off. We used the ultrasoft pseudopotential of Vanderbilt [125] in order to substitute the inactive core electrons close to the nucleus. These pseudopotential requires less computational resources than the norm-conserving potentials [126]. For the exchange correlation functional we used both the local density (LDA) and the generalized gradient (GGA) approximations. The cut-off energies of Ru, Cr and X are shown in Table 3.1.

From the single point calculation, the cutoff energy of 600 eV was chosen for metallic Ru, Cr, V, Mo, Pd and Pt. The cutoff energy of Mn and Fe was set to be 1100 eV.

Lastly, the energy cutoffs of 1000 eV, 1500 eV and 1600 eV were selected for metallic Co, Re and Zr respectively. The kinetic energy cut-off is influenced by the atomic species of the material. The results of calculated lattice constants of Ru, Cr and X dopants using the LDA and GGA approximations are listed in Table 3.1, along with the available theoretical and experimental data. For all the studied metals except for Mn, we find that the LDA yield slightly smaller lattice constants than the GGA results. These findings show the well-known tendency of GGA and LDA to respectively overestimate and underestimate lattice constants. The experimental lattice constants are closer to the GGA results than LDA.

The k-points are the number of points used to sample the Brillouin zone in the k-space for the plane wave expansion. We performed the k-point convergence tests. We have carried out total energy calculation at fixed cutoff energy for all the studied metals while varying the number of k-points. We increased the number of k-points until the total energy converged to within 1 meV per atom. The Brillouin zone integrations were performed using the Monkhorst-Pack scheme [132]. The k-points for Mn, Ru, and Cr were chosen to be $3 \times 3 \times 3$, $28 \times 28 \times 2$ and $4 \times 4 \times 4$ respectively.

3.3. Binary and ternary alloys

3.3.1 Introduction

In this section, we explore the two binary alloys composed of the metallic Ru and Cr; which forms the basis of this study. We will also present the transition metal doped alloys. In this section, we outline the computational models and briefly describe the computational technique used in this study. The most relevant results obtained for the structural, thermodynamic and magnetic properties will be presented and discussed.

3.3.2 Computation model

a) Undoped binary alloys: A15 Ru₃Cr and Cr₃Ru

The Ru₃Cr and Cr₃Ru are the A15 type structures of space group Pm-3N (number 223). The A15 phases are described as a series of intermetallic compounds with a formula A₃B; where A is a transitional metal and B can be any element. In the case of Ru₃Cr, Ru and Cr represent the A and B respectively. The A15 unit cells of Ru₃Cr and Cr₃Ru are shown in Figure 3.1. A special characteristic of the A15 crystal structure is that the A atoms form mutually orthogonal linear chains that run throughout the crystal lattice. Furthermore, the A15 structures are close-packed structures in which the size directs their stability [133].

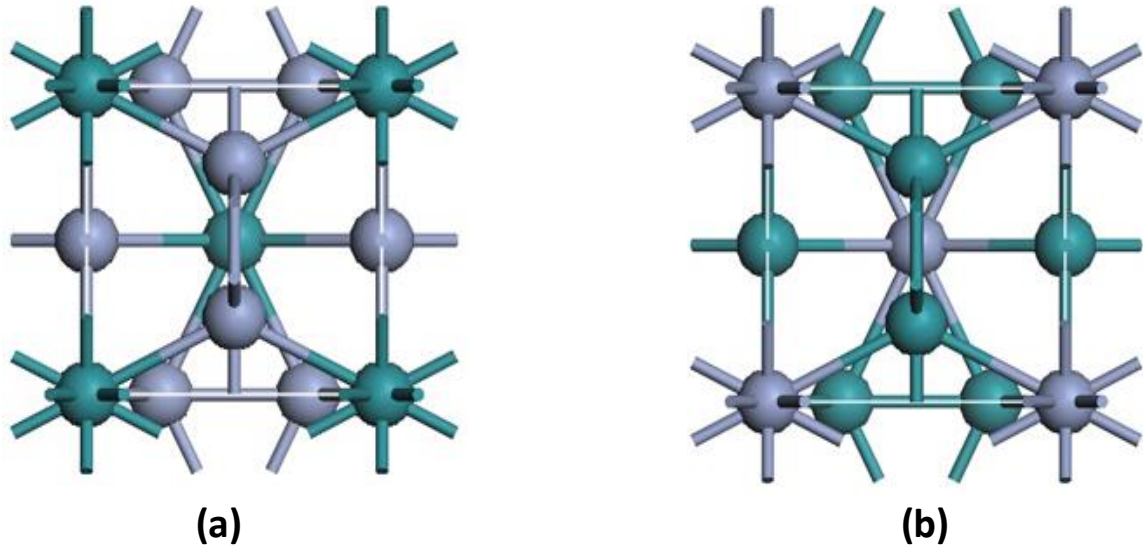


Figure 3.1 : (a) Cr_3Ru structure: atoms are represented by balls of different colours, green (Ru) and grey (Cr), (b) Ru_3Cr structure: green balls (Cr) and grey balls (Ru).

Table 3.2 : The atomic positions (Wyckoff notation) in the A15 Ru_3Cr and Cr_3Ru crystal structures.

System	Atoms	Positions	x	y	z
Ru_3Cr	Cr	3a	0.25	0.0	0.50
	Ru	1a	0	0	0
Cr_3Ru	Cr	1a	0	0	0
	Ru	3a	0.25	0.0	0.50

In Cr_3Ru (Fig.3.1 (a)), the Ru atoms are located at the corners and in the centre of the cube, while the Cr atoms are arranged in pairs on the cube faces. The spatial positions of Cr and Ru atoms are respectively 3a (0.25, 0.0, 0.50) and 1a (0, 0, 0) as listed in Table

3.2. The Ru_3Cr in Figure 3.1(b) has the same structure as the Cr_3Ru , the difference being in the position of the Cr and Ru atoms. In Ru_3Cr the Ru atom occupies the 3a site, while the Cr atom is on the 1a site as shown in Table 3.2.

b) Supercells and Transition metal doped alloys

In this section, we show the unit cell, supercells of the transition metal doped $\text{Ru}_{48}\text{Cr}_{16}$ and $\text{Cr}_{48}\text{Ru}_{16}$. The $2 \times 2 \times 2$ supercells were constructed from the optimized structures of A15 Ru_3Cr and Cr_3Ru phases as shown in Figure 3.2. A supercell is made of the repetition of unit cells in a crystal lattice in order to avoid interactions between the neighboring atoms since the atoms are arranged periodically.

Our simulated supercells contain 64 atoms. We doped the supercell with one to six transition metal dopant atoms X (where X = V, Mn, Fe, Co, Zr, Mo, Pd, Re and Pt). We will introduce the Mn doped alloys for illustration purposes. Figure 3.3 illustrates the Ru rich alloys; $\text{Ru}_{47}\text{MnCr}_{16}$, $\text{Ru}_{46}\text{Mn}_2\text{Cr}_{16}$, $\text{Ru}_{45}\text{Mn}_3\text{Cr}_{16}$, $\text{Ru}_{44}\text{Mn}_4\text{Cr}_{16}$, $\text{Ru}_{43}\text{Mn}_5\text{Cr}_{16}$ and $\text{Ru}_{42}\text{Mn}_6\text{Cr}_{16}$ generated by CASTEP package. The Ru atoms are substituted by one to six Mn atoms as shown in figure 3.3 (a-f).

The crystal structures of Cr rich ternary alloys are shown in Figure 3.4. The following structures were modeled: $\text{Cr}_{47}\text{MnRu}_{16}$, $\text{Cr}_{46}\text{Mn}_2\text{Ru}_{16}$, $\text{Cr}_{45}\text{Mn}_3\text{Ru}_{16}$, $\text{Cr}_{44}\text{Mn}_4\text{Ru}_{16}$, $\text{Cr}_{43}\text{Mn}_5\text{Ru}_{16}$ and $\text{Cr}_{42}\text{Mn}_6\text{Ru}_{16}$ structures. The structures in Figures 3.4 (a –f) indicate the Cr rich alloys doped with different concentration of Mn atoms.

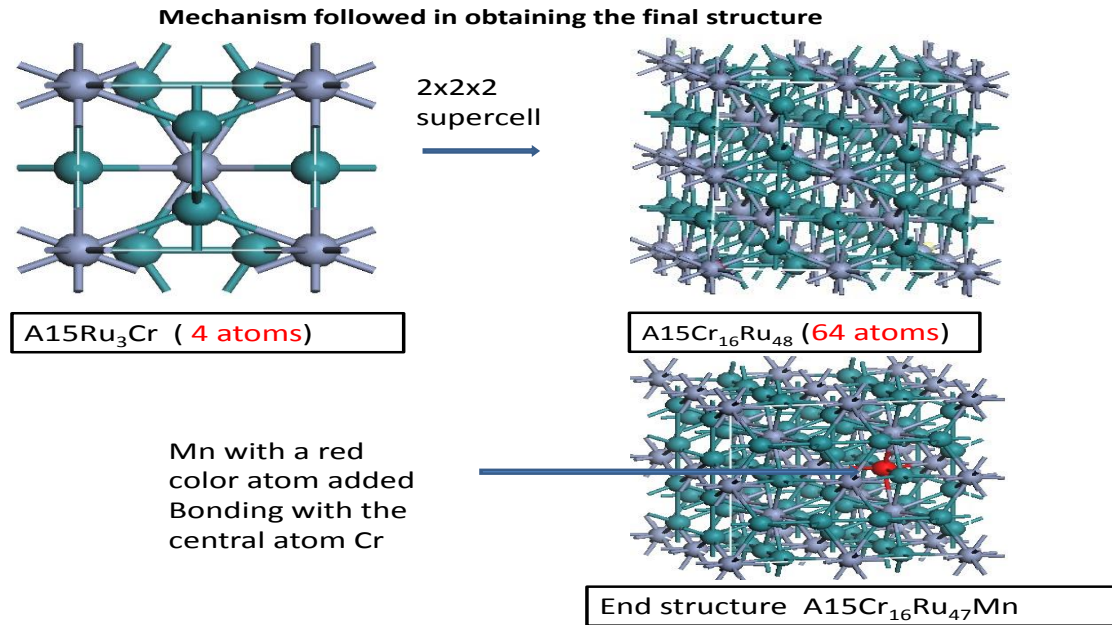


Figure 3.2 : Supercell, (a) Bulk $A_{15}Ru_3Cr$ unit cell, (b) A $2 \times 2 \times 2$ supercell of $A_{15}Ru_3Cr$ and (c) structure of Mn doped into supercell of $A_{15}Ru_3Cr$. Blue, light green and gray spheres represent Mn, Ru and Cr respectively

At first, the CASTEP simulator allows one to model a structure of interest. In this case, $A_{15}Ru_3Cr$ was modelled and the single point energy calculation was computed in order to optimize the k-points and kinetic energy cut-off. After that, we performed a geometry optimization to relax the equilibrium lattice parameter and to find the ground state energy. Furthermore, we built a $2 \times 2 \times 2$ supercell on the relaxed structure and substitute Ru by Mn atom.

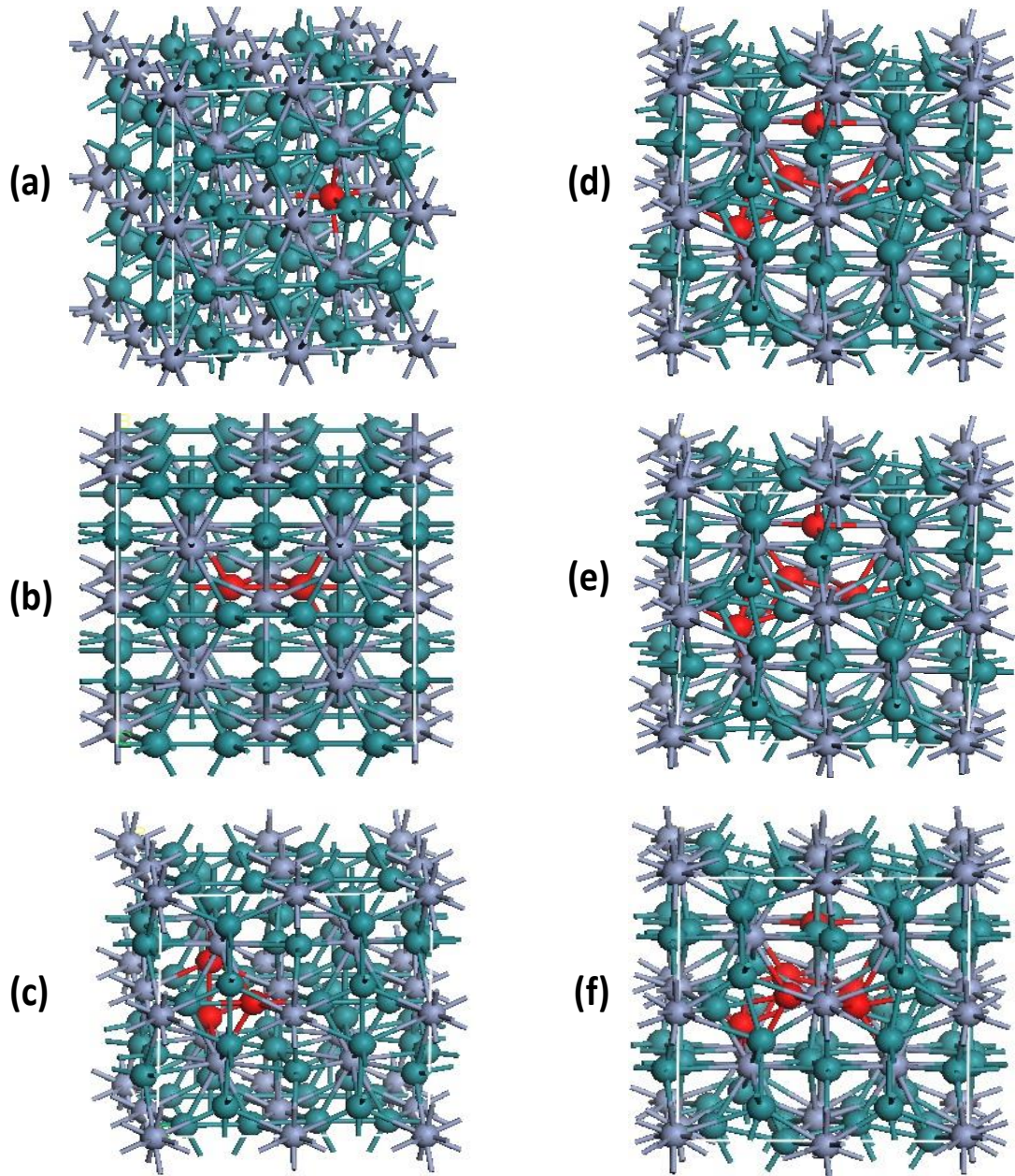


Figure 3.3 : The schematic diagram of the Ru rich supercells used in the calculations. Each supercell contain 64 atoms (a) $\text{Ru}_{47}\text{MnCr}_{16}$, (b) $\text{Ru}_{46}\text{Mn}_2\text{Cr}_{16}$, (c) $\text{Ru}_{45}\text{Mn}_3\text{Cr}_{16}$, (d) $\text{Ru}_{44}\text{Mn}_4\text{Cr}_{16}$, (e) $\text{Ru}_{43}\text{Mn}_5\text{Cr}_{16}$ and (f) $\text{Ru}_{42}\text{Mn}_6\text{Cr}_{16}$ ternary alloys: Ru, Cr and Mn atoms are represented by green, grey and red balls respectively.

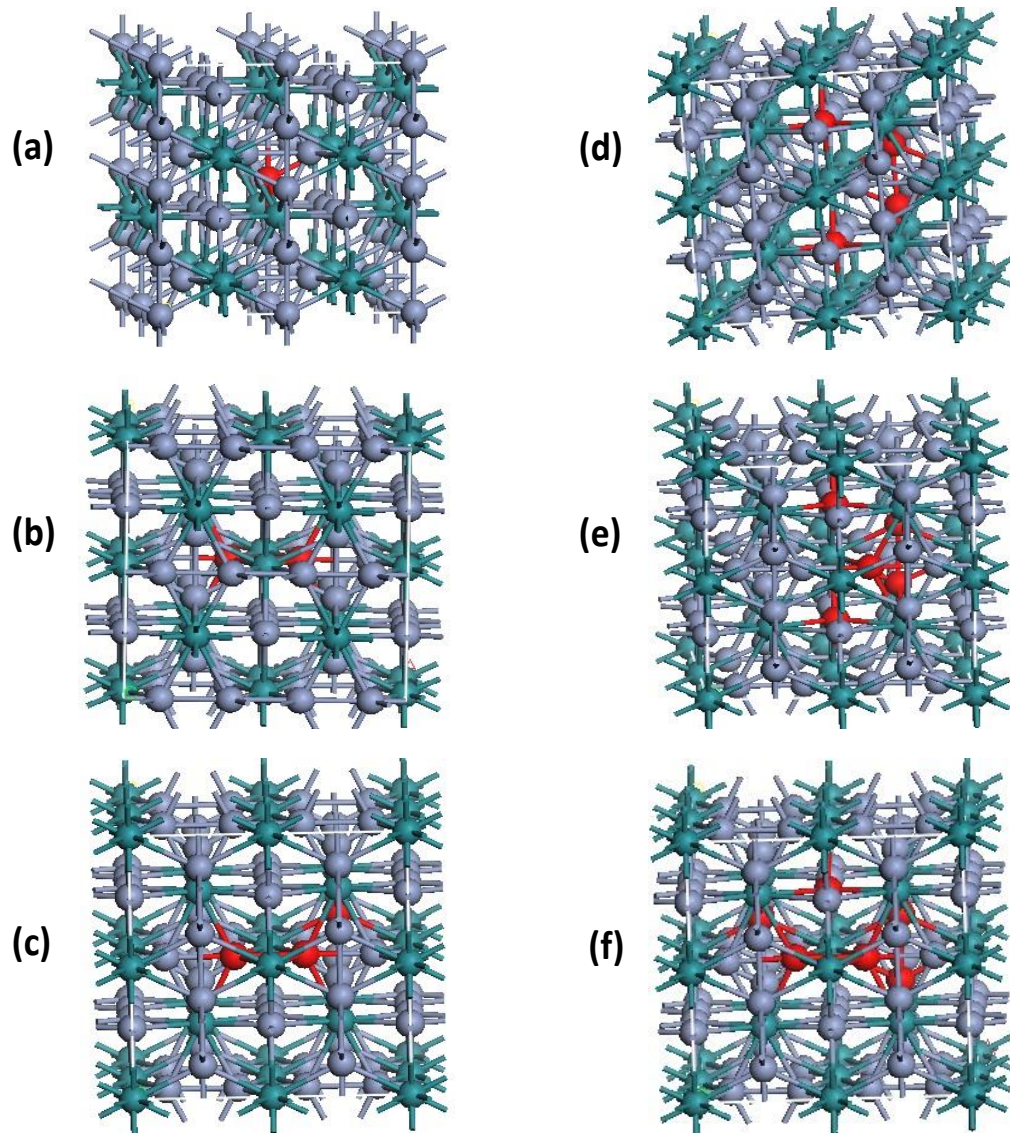


Figure 3.4 : The schematic diagram of the Cr rich supercells used in the calculations. Each supercell contain 64 atoms (a) $\text{Cr}_{47}\text{MnRu}_{16}$, (b) $\text{Cr}_{46}\text{Mn}_2\text{Ru}_{16}$, (c) $\text{Cr}_{45}\text{Mn}_3\text{Ru}_{16}$, (d) $\text{Cr}_{44}\text{Mn}_4\text{Ru}_{16}$, (e) $\text{Cr}_{43}\text{Mn}_5\text{Ru}_{16}$ and (f) $\text{Cr}_{42}\text{Mn}_6\text{Ru}_{16}$ ternary alloys: Ru, Cr and Mn atoms are represented by green, grey and red balls respectively.

3.3.3 Computational method

The use of computer simulation techniques is becoming more important in the understanding of the microscopic behaviour of materials. The First principles calculations were carried out to determine the cutoff energy and k-points for the A15 phases (Ru_3Cr and Cr_3Ru) and the supercells of the doped, transition metal undoped $\text{Ru}_{48}\text{Cr}_{16}$ and $\text{Cr}_{48}\text{Ru}_{16}$ alloys. The calculations were performed using theoretical lattice constants in the framework of DFT by CASTEP code. All the density-functional theory (DFT) calculations are executed using a plane-wave basis set with the projector augmented plane wave (PAW) method as implemented in the CASTEP code. The generalized gradient approximation is employed for the exchange-correlation functional. Structural, thermodynamical and magnetic calculations based on density functional theory (DFT) implemented in CASTEP code have been investigated for A15 Ru_3Cr and Cr_3Ru , undoped binary and RuCrX ternary systems.

3.3.4 Cutoff energy and k-points convergence

In order to determine the appropriate cutoff energy for the studied crystal structures, we carried out single point energy calculations where we increased cutoff energy and monitored the convergence of energy of approximately 1 meV/atom. The cutoff energy of 500 eV was chosen for both the binary and ternary alloys. As an illustration, Figure 3.5 (a) show the curves of total energy against cutoff energy of $\text{Ru}_{48}\text{Cr}_{16}$ supercell doped

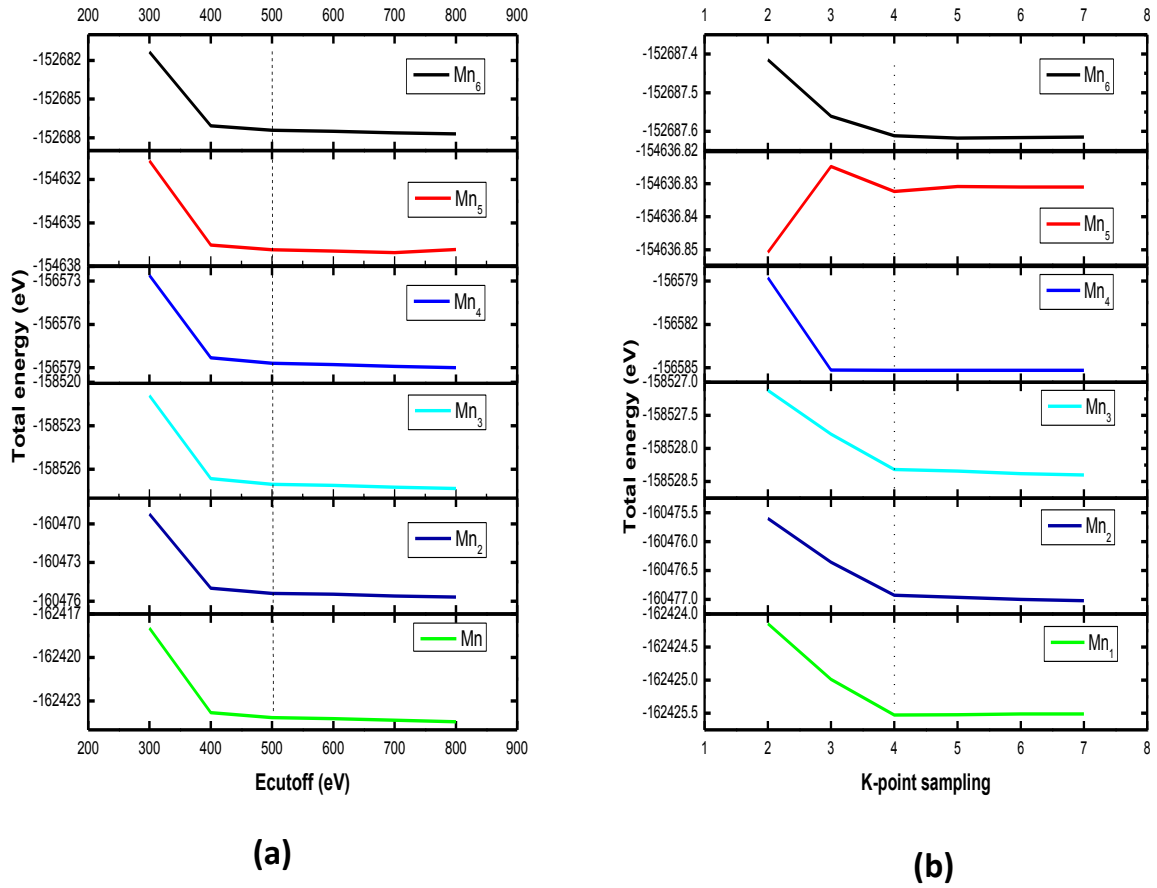


Figure 3.5 : (a) Total energy against cutoff energy and (b) total energy (eV/atom) against the number of k-points for Ru₄₈Cr₁₆ supercell doped with different concentrations of Mn (substitution of one to six Ru atoms by Mn atoms)

with different concentrations of Mn (substitution of one to six Ru atoms by Mn atoms). We further performed the k-points convergence tests , where we carried out total energy calculations at fixed cutoff energy of 500 eV for each structure the number of k-points was varied. 20 x 20 x 20 mesh points in k-space based on Monkhorst-Pack scheme for Ru₃Cr and Cr₃Ru A15 phases sampled the Brillouin zone. In Figure 3.5 (b) we show the convergence of the total energies with respect to the number of k-points for Ru₄₈Cr₁₆

supercell doped with different concentrations of Mn. The total energy with respect to the number of k-points was considered converged when the energy change per atom was within 1 meV per atom. The k-points were chosen to be $4 \times 4 \times 4$ for doped and undoped $\text{Ru}_{48}\text{Cr}_{16}$ and $\text{Cr}_{48}\text{Ru}_{16}$ systems. The selected parameters are sufficient in leading to well converged total energy and geometrical configurations.

3.3.5 Geometry optimization

The first step in any ab-initio calculation is to find the optimised geometry of the crystalline structure. Geometry optimization is the way of finding the minimum energy of a system. Optimization plays a role in producing a relaxed structure, to ensure accurate examination of the system's properties. In order to check the accuracy of the calculations, we first optimized the structures of A15 Ru_3Cr and Cr_3Ru , and the doped and undoped $\text{Ru}_{48}\text{Cr}_{16}$ and $\text{Cr}_{48}\text{Ru}_{16}$ supercells at a fixed cutoff energy of 500 eV. In addition, the optimization was done using the GGA-PBE functional within the CASTEP code. The lattice constants of both the binary and ternary alloys were allowed to vary. The calculations were carried out until a good convergence was obtained. The minimized total energies of the structures were used to calculate the heats of formation and magnetic moments that we will discuss in the next section.

3.3.6 Lattice constants and heats of formation for the A15 RuCr₃ and Cr₃Ru Alloys

Table 3.3 : Calculated lattice constants and heats of formation of Ru₃Cr and Cr₃Ru in the A15 phase.

System	Prototype notation	a (Å)	a (Å)	a (Å)	ΔH _f (eV/atom)	ΔH _f (eV/atom)
		LDA	GGA	previous work	this work	previous work
Ru ₃ Cr	Cr ₃ Si	4.694	4.777	4.788[8]	0.39	0.3225[8]
Cr ₃ Ru	Cr ₃ Si	4.537	4.623	4.623[8]	0.085	0.0796[8]

Firstly, we computed the equilibrium structural properties lattice constants and heats of formation of the binary. The calculated lattice constants, heats of formation are shown in Table 3.3. For comparison, we have included the results from a theoretical investigation of heats of formation for Ru₃Cr and Cr₃Ru using first principles calculations [8]. Our computed LDA lattice constants for both systems are slightly lower than the GGA results. It is owing to the GGA approximation, which always overestimates the results. It is evident that the lattice constant is lower in Cr rich than Ru rich alloy. We note here that the values of the GGA lattice constants are in good agreement with the theoretical results than the LDA. The heats of formation for Ru₃Cr and Cr₃Ru are predicted as 0.39 eV/atom and 0.085 eV/atom respectively. As seen, our results agree with the previous theoretical values of 0.3225 eV/atom and 0.0796 eV/atom for Ru₃Cr and Cr₃Ru respectively. The obtained positive values indicate that the Ru₃Cr and Cr₃Ru in the A15 phase are unstable. However, the values are closer to zero, especially for Cr₃Ru, in complete agreement with

the theoretical work by M. M Tibane et.al [8]. Since the values are closer to zero, it may be possible to reduce heats of formation of the Ru_3Cr and Cr_3Ru by doping the systems with metallic dopants. We will discuss deeply the effect of doping in the next section.

3.3.7 Thermodynamic properties for the doped and undoped $\text{Ru}_{48}\text{Cr}_{16}$ and $\text{Cr}_{48}\text{Ru}_{16}$ supercells

Researchers are devoted to improve the stability of high temperature materials by alloying with other elements and mechanical alloying. With the motivation of finding promising ternary alloys from A15 Ru_3Cr and Cr_3Ru binary alloys with improved physical properties in comparison with other ternary alloys, the present section focuses on the composition dependence of the thermodynamic properties of RuCrX ternary alloys by performing ab initio calculations, based of augmented plane-wave within DFT implemented in CASTEP code. These DFT simulations are beneficial to improve our understanding of the effects of substitution on the properties of binary alloys, and of the design of advance materials. We investigate the thermodynamic properties that are usually the basis of solid-state science and industrial applications. The study of the thermodynamic properties of materials is of importance to extend our knowledge on their specific behaviours when undergoing severe constraints of high pressure and high temperature environment [134].

In this section we research the effects of transition metals X (X = Zr, Mn, V, Mo, Pt, Pd, Co, Fe and Re) on the heats of formation of the undoped $2 \times 2 \times 2$ Ru₄₈Cr₁₆ and Cr₄₈Ru₁₆ supercells (constructed from the unstable A15 Ru₃Cr and Cr₃Ru respectively). The Ru or

Table 3.4 : calculated heats of formation of V, Mn, Fe and Co doped Ru₄₈Cr₁₆ and Cr₄₈Ru₁₆ alloys.

System	Heats of Formation (ΔH_f)				Atomic percentage
	V	Mn	Fe	Co	at.%
Ru ₄₇ Cr ₁₆ X	0.272	0.138	-6.491	0.259	1.56
Ru ₄₆ Cr ₁₆ X ₂	0.227	-0.022	-13.278	0.245	3.13
Ru ₄₅ Cr ₁₆ X ₃	0.176	-0.193	-20.079	0.206	4.69
Ru ₄₄ Cr ₁₆ X ₄	0.163	-0.329	-26.842	0.198	6.25
Ru ₄₃ Cr ₁₆ X ₅	0.160	-0.468	-33.610	0.195	7.81
Ru ₄₂ Cr ₁₆ X ₆	0.169	-0.593	-40.370	0.191	9.38
Cr ₄₇ Ru ₁₆ X	0.047	-0.079	-6.707	0.050	1.56
Cr ₄₆ Ru ₁₆ X ₂	0.040	-0.212	-13.468	0.053	3.13
Cr ₄₅ Ru ₁₆ X ₃	0.032	-0.345	-20.986	0.053	4.69
Cr ₄₄ Ru ₁₆ X ₄	0.025	-0.478	-26.991	0.053	6.25
Cr ₄₃ Ru ₁₆ X ₅	0.018	-0.612	-33.752	0.055	7.81
Cr ₄₂ Ru ₁₆ X ₆	0.011	-0.745	-40.513	0.055	9.38

Cr atom/s in the $2 \times 2 \times 2$ Ru₄₈Cr₁₆ or Cr₄₈Ru₁₆ supercell structure were replaced by different doping concentrations of X. The heats of formation of the transition metal doped alloys were calculated using the First-principles calculation, and discussed in more detail in the following sections.

3.3.7.1 First-row transition metal doping

a) Ru-Rich Ternary Alloys

Firstly, we carried out structural optimization of $2 \times 2 \times 2$ $\text{Ru}_{48}\text{Cr}_{16}$ supercell and then we introduced dopants into the optimized material. The heats of formation for the studied bulk $\text{A15 Ru}_3\text{Cr}$ and the undoped $\text{Ru}_{48}\text{Cr}_{16}$ supercell were calculated to be 0.39 eV/atom and 0.294 eV/atom respectively. When Ru atom in the $\text{Ru}_{48}\text{Cr}_{16}$ supercell structure was replaced by one X atom ($X = \text{V, Mn, Fe and Co}$), it was observed that heats of formation decreased from 0.294 eV/atom to 0.272 eV/atom, 0.138 eV/atom, -6.491 eV/atom and 0.259 eV/atom respectively, as presented in Table 3.4. Based on these findings, it can be clearly seen that the introduction of transition metal atom has an influence in decreasing the heat of formation of the undoped $\text{Ru}_{48}\text{Cr}_{16}$. We further investigated the effect of dopants by substituting two, three, four, five and six Ru atoms in the supercell by V, Mn, Fe and Co dopants, which corresponds to the atomic percentage of 3.13%, 4.69%, 6.25%, 7.81% and 9.38% respectively. The results are presented in Table 3.4, the last column represent the atomic percentage of the dopants. We obtained positive heats of formation for $\text{Ru}_{48}\text{Cr}_{16}$ supercell doped with one to six Co or V atoms; we observed a decrease in heats of formation with increasing Co doping concentration. Similar trend was observed when the supercell was doped with one to five V atoms, however, when the system was doped with six V atoms we noted an increased heat of formation.

The calculated heats of formation for all the studied Mn doped system are lower than the original undoped $\text{Ru}_{48}\text{Cr}_{16}$ with ΔH_f of 0.294 eV/atom. We predicted the positive heat of formation when one Mn atom replaced Ru atom in $\text{Ru}_{48}\text{Cr}_{16}$, however the negative heats

of formation were obtained for the supercell doped with two to six Mn atoms. For two, four and six Mn doped systems, the ΔH_f were computed as -0.022 eV/atom, -0.329 eV/atom and -0.593 eV/atom respectively. All studied Mn doped supercells were predicted to be stable except for one Mn doped system. The stability of ternary Ru rich alloy has improved with increasing Mn concentration.

Heats of formation for Fe doped supercell at all concentrations are negative, indicating that the Fe doped systems are stable. As in the case of Mn doped system, the level of stability was enhanced as we increase the number of Fe atoms as shown in Table 3.4. The heats of formation for the two, four and six Fe doped systems are -13.278 eV/atom, -26.842 eV/atom and -40.370 eV/atom respectively. Fe has a significant decrease in ΔH_f as compared to other studied first-row transition metal dopants. The six Fe doped system has relatively lower heat of formation when compared to all studied Ru rich doped systems as shown in Table 3.4. The lower the heat of formation of the system, the more stable it becomes. From the previous statement, we conclude that the six Fe doped $\text{Ru}_{48}\text{Cr}_{16}$ atom is the most stable Ru rich structure as compared to the studied 1st row transition metal dopants. The decrease in the heats of formation for two to six X doped $\text{Ru}_{48}\text{Cr}_{16}$ supercell follow the order of $\text{Fe} < \text{Mn} < \text{V} < \text{Co}$, whereas for one X doped system we noted a decreasing order of $\text{Fe} < \text{Mn} < \text{Co} < \text{V}$.

b) Cr- Rich Ternary Alloys

In addition we also calculated the heats of formation of $\text{Cr}_{48}\text{Ru}_{16}$ doped with one to six atoms of Co, V, Mn and Fe, in this case Cr atoms were substituted by the dopants. The results are presented in Table 3.4. It is important to mention that the studied heats of

formation for the bulk A15 Cr₃Ru and the undoped Cr₄₈Ru₁₆ supercell were obtained to be 0.085 eV/atom and 0.055 eV/atom respectively. For Cr rich ternaries, the heats of formation for V, Mn or Fe-doped systems decrease with increasing dopant concentration. However, we observed that the values of ΔH_f for Cr rich ternaries are lower as compared to the Ru rich ternaries. For example, ΔH_f for two, four and six Mn-doped Cr₄₈Ru₁₆ we obtained -0.212 eV/atom, -0.478 and -0.745 respectively, whereas for two, four and six Mn-doped Ru₄₈Cr₁₆ we obtained -0.022 eV/atom, -0.329 eV/atom and -0.593 eV/atom respectively.

Co doped Cr₄₈Ru₁₆ system exhibits a different trend compared to the V, Mn or Fe-doped systems. Heats of formation for V, Mn or Fe-doped systems are lower as compared to the undoped Cr₄₈Ru₁₆. In Table 3.4 we noted that the heats of formation for one to four Co doped are lower than the undoped system, in addition the two to four Co doped system has yielded the same value of $\Delta H_f = 0.053$ eV/atom. For five Co-doped, ΔH_f increased to 0.055 eV/atom, the heats of formation for the undoped Cr₄₈Ru₁₆ and five Co-doped system are equal. The value later increased further to $\Delta H_f = 36.549$ eV/atom for six Co doped system. For Cr rich ternaries, we obtained negative heats of formation for all studied Mn and Fe-doped systems, indicating that the structures are stable. Fe and Mn enhance the stability of the systems. The decrease in the heats of formation for all the studied X doped Cr₄₈Ru₁₆ supercell follow the order of Fe < Mn < V < Co.

From Table 3.4 it is apparent that the Fe doped Cr rich alloys are more stable than the Ru rich alloys. The results indicate that the six Fe doped Cr₄₈Ru₁₆ is the most stable structure

compared to all the studied first-row transition metal doped systems. There are no available theoretical reports about the properties of our studied transition doped $\text{Ru}_{48}\text{Cr}_{16}$ and $\text{Cr}_{48}\text{Ru}_{16}$ alloys to our knowledge.

3.3.7.2 Second-row transition metal doping

Table 3.5 : calculated heats of formation of Pd, Zr and Mo doped $\text{Ru}_{48}\text{Cr}_{16}$ and $\text{Cr}_{48}\text{Ru}_{16}$ alloys.

System	Heats of Formation (ΔH_f)			Atomic percentage
	Pd	Zr	Mo	at.%
$\text{Ru}_{47}\text{Cr}_{16}\text{X}$	0.263	0.266	-14.860	1.56
$\text{Ru}_{46}\text{Cr}_{16}\text{X}_2$	0.264	0.245	-30.014	3.13
$\text{Ru}_{45}\text{Cr}_{16}\text{X}_3$	0.222	0.194	-44.877	4.69
$\text{Ru}_{44}\text{Cr}_{16}\text{X}_4$	0.227	0.198	-60.320	6.25
$\text{Ru}_{43}\text{Cr}_{16}\text{X}_5$	0.241	0.192	-75.453	7.81
$\text{Ru}_{42}\text{Cr}_{16}\text{X}_6$	0.267	0.195	-90.587	9.38
$\text{Cr}_{47}\text{Ru}_{16}\text{X}$	0.065	0.065	-15.074	1.56
$\text{Cr}_{46}\text{Ru}_{16}\text{X}_2$	0.073	0.081	-30.201	3.13
$\text{Cr}_{45}\text{Ru}_{16}\text{X}_3$	0.081	0.093	-45.329	4.69
$\text{Cr}_{44}\text{Ru}_{16}\text{X}_4$	0.092	0.100	-40.410	6.25
$\text{Cr}_{43}\text{Ru}_{16}\text{X}_5$	0.097	0.129	-75.585	7.81
$\text{Cr}_{42}\text{Ru}_{16}\text{X}_6$	0.065	0.146	-90.710	9.38

Similar studies were conducted on $\text{Ru}_{48}\text{Cr}_{16}$ and $\text{Cr}_{48}\text{Ru}_{16}$ alloys doped with Pd, Zr or Mo. The calculated heats of formation and atomic percentages are presented in Table 3.5. The heats of formation for all studied Pd and Zr doped systems were positive which are

expected to be unstable. In Ru rich ternaries, the heats of formation increased from one Pd doped to two Pd doped system, then decrease in three Pd doped system, and later increase from four to six Pd doped system. Whereas in Cr rich ternaries, the heats of formation increased from one Pd doped to five Pd doped system, then reduced in six Pd doped alloy as shown in Table 3.5. Heats of formation for Zr doped Ru rich system decreased from one Zr doped to three Zr doped system, then increased in four Zr doped system, then reduced in five Zr doped and lastly increased in six Zr doped system. For Cr rich ternaries, the heats of formation for Zr doped system increase with the increasing Zr concentration.

The calculations predicted the negative heats of formation for all studied Mo-doped systems. However, we obtained lower heats of formation for Cr rich Mo-doped as compared to Ru rich Mo-doped systems, except for the four Mo doped structure. For example ΔH_f of two, four and six Mo doped $\text{Ru}_{48}\text{Cr}_{16}$ are -30.014 eV/atom, 60.320 eV/atom and -90.587 eV/atom respectively. Whereas for two, four and six Mo doped $\text{Cr}_{48}\text{Ru}_{16}$ the calculated heats of formation were -30.201 eV/atom, -40.410 eV/atom and -90.710 eV/atom respectively, as listed in Table 3.5. When the content of Mo is increased, the heats of formation decreased compared with the original structure. Mo doped structures are the only stable structures as compared to all studied second-row transition metal doped structures. We predicted the six Mo doped $\text{Cr}_{48}\text{Ru}_{16}$ as the most stable structure amongst all the studied Mo, Zr and Pd doped systems. The decrease in the heats of formation for all the studied X (second row) doped $\text{Ru}_{48}\text{Cr}_{16}$ and $\text{Cr}_{48}\text{Ru}_{16}$ supercell

follow the order of Mo < Zr < Pd, except for one X doped Cr₄₈Ru₁₆ system which follow the order of Mo < Zr = Pd.

3.3.7.3 Third-row transition metal doping

Table 3.6 : calculated heats of formation of Pt and Re doped Ru₄₈Cr₁₆ and Cr₄₈Ru₁₆ alloys.

System	ΔH_f (eV/atom)		System	ΔH_f (eV/atom)		at. %
	Pt	Re		Pt	Re	
Ru ₄₇ Cr ₁₆ X	0.280	0.276	Cr ₄₇ Ru ₁₆ X	0.058	0.056	1.56
Ru ₄₆ Cr ₁₆ X ₂	0.265	0.252	Cr ₄₆ Ru ₁₆ X ₂	0.067	0.060	3.13
Ru ₄₅ Cr ₁₆ X ₃	0.209	0.217	Cr ₄₅ Ru ₁₆ X ₃	0.071	0.062	4.69
Ru ₄₄ Cr ₁₆ X ₄	0.217	0.214	Cr ₄₄ Ru ₁₆ X ₄	0.078	0.064	6.25
Ru ₄₃ Cr ₁₆ X ₅	0.224	0.214	Cr ₄₃ Ru ₁₆ X ₅	0.084	0.066	7.81
Ru ₄₂ Cr ₁₆ X ₆	0.263	0.218	Cr ₄₂ Ru ₁₆ X ₆	0.094	0.073	9.38

Lastly, we investigated the effect of Pt and Re on the heats of formation of Ru₄₈Cr₁₆ and Cr₄₈Ru₁₆ alloys. The results are listed in Table 3.6. Our calculations predicted positive heats of formation for the entire Pt and Re doped systems indicating the instability of the alloys. The calculated heats of formation of two, four and six Pt doped Ru₄₈Cr₁₆ are 0.265 eV/atom, 0.217 eV/atom and 0.263 eV/atom respectively. For comparison purposes, we obtained 0.067 eV/atom, 0.078 eV/atom and 0.094 eV/atom for Pt doped Cr₄₈Ru₁₆ alloys. It is apparent that in all cases the values for Ru rich ternary alloys were higher as compared to the Cr rich ternary alloys. The heats of formation for both the Pt and Re doped Cr₄₈Ru₁₆ present a regular increase with increasing dopant concentration, in addition, the values for Re doped Cr₄₈Ru₁₆ are positive but closer to zero. Attempts to improve the stability of Cr₄₈Ru₁₆. However, by introducing Pt or Re dopants to Cr₄₈Ru₁₆ system have been less successful.

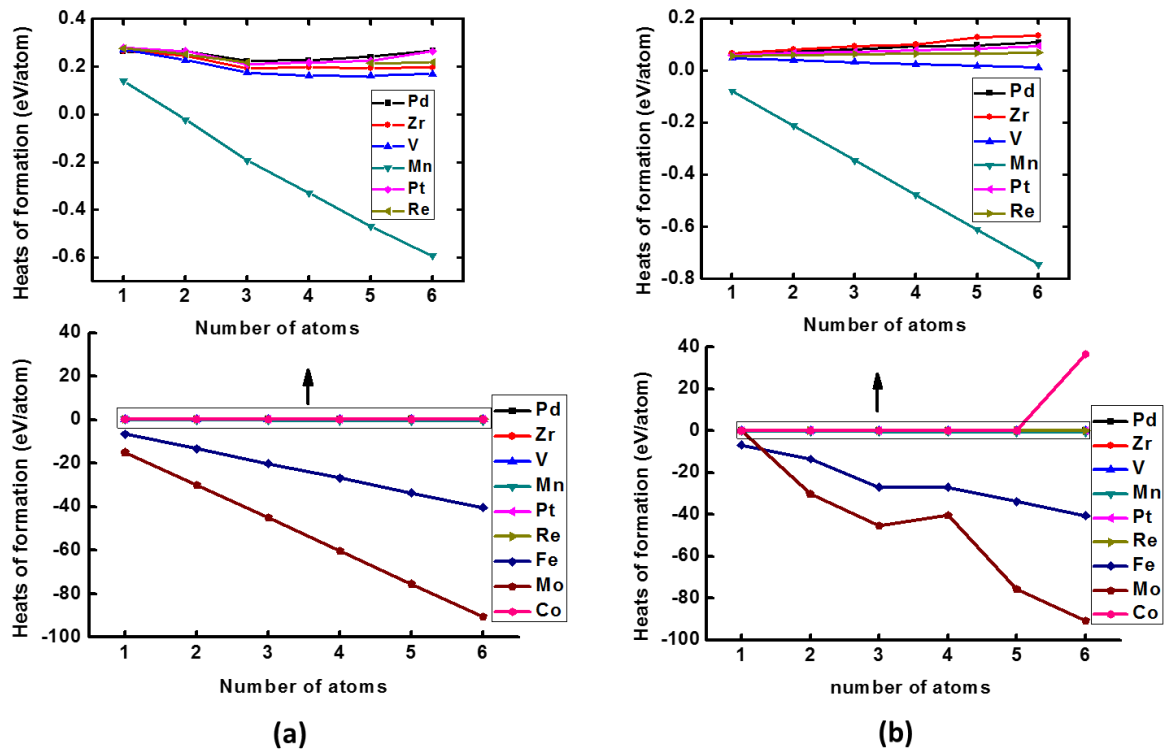


Figure 3.6 : The heats of formation (in eV/atom) against the number of dopant atoms for (a) X-doped $\text{Ru}_{48}\text{Cr}_{16}$ and (b) X-doped $\text{Cr}_{48}\text{Ru}_{16}$.

In Figures 3.6(a) and (b) we show the overall comparison of the heats of formation against the number of X atoms for all the X doped $\text{Ru}_{48}\text{Cr}_{16}$ and $\text{Cr}_{48}\text{Ru}_{16}$ respectively. The data is presented using two graphs due to scale effects. In both Figures, the upper graphs represent the Pd, Zr, V, Pt, Mn and Re-doped systems. It can be clearly seen from the upper graphs that the heats of formation for X doped Ru rich systems are higher than those of Cr rich systems are. In addition we notice negative heats of formation on the graph of Mn doped structures only (in Fig 3.6 (a) and (b)) indicating that the structures are stable. The six Mn doped Cr rich structure was found to be more stable (with the heat of formation of -0.745 eV/atom) compared to all studied Pd, Zr, V, Pt, Mn and Re-doped

systems. The main graphs present data for the heats of formation for Pd, Zr, V, Pt, Mn, Re, Mo, Co and Fe doped $\text{Ru}_{48}\text{Cr}_{16}$ and $\text{Cr}_{48}\text{Ru}_{16}$ systems respectively. The plots clearly show negative heats of formation for the Fe and Mo doped structures. However, the Mo doped Cr rich structures generally have the lowest heats of formation compared to all studied X doped $\text{Ru}_{48}\text{Cr}_{16}$ and $\text{Cr}_{48}\text{Ru}_{16}$ systems. Comparing the heats of formation of the more stable six Mn, six Fe or six Mo doped $\text{Cr}_{48}\text{Ru}_{16}$, which were calculated as -0.745 eV/atom, -40.513 eV/atom and -90.710 eV/atom, it has turned out that the six Mo doped $\text{Cr}_{48}\text{Ru}_{16}$ is the most stable structure compared to all the X-doped $\text{Ru}_{48}\text{Cr}_{16}$ and $\text{Cr}_{48}\text{Ru}_{16}$ systems. Despite few fluctuations, which require further research, our results seem to confirm more general conclusion that an increasing amount of Fe, Mn and Mo in the ternary alloys have stabilising effect on the properties.

3.3.8. Magnetic Moments

Overview

The magnetic moment of a material consists of contributions from spin and orbit polarization. The total spin magnetic moment in μB is the difference between the number of spin-up occupied states and the spin-down occupied states. The symbol μB is the Bohr magneton, the units for expressing magnetic moment of an electron caused by either its orbital or spin angular momentum [135-136].

In the current study, we used CASTEP code to calculate the magnetic moments of the systems. Magnetism originates from the spin and orbital magnetic moment of an electron. There are different types of magnetism in materials; however, for this section we define the ferromagnetism, anti-ferromagnetism and ferrimagnetism.

Table 3.7 : Effect of smearing width on the magnetic moment (per unit cell) of one Mn doped Cr₄₈Ru₁₆ alloy

Smearing width (eV)	Magnetic moment (μ B)
0.3	0.02
0.2	0.00
0.1	0.12
0.01	1.78
0.001	2.00
0.0005	2.00
0.00025	2.33

The coupling between spins [137] can form ordered magnetic systems such as ferromagnetic, anti-ferromagnetic and ferrimagnetic. In ferrimagnets the magnetic moments of two sublattices in a system are not equal and result in a net magnetic moment, whilst in antiferromagnets the two sublattice moments are exactly equal but opposite, resulting in a net moment of zero. Lastly, in ferromagnets, the atomic moments exhibit very strong interaction produced by the electronic exchange forces and result in the parallel or anti-parallel alignment of atomic moments. Ferromagnets have a parallel alignment of moments that gives rise to a net magnetisation.

Table 3.8 : Calculated magnetic moments (per atom) of individual atoms in ternary structures

Metals	Magnetic moments (μB)	
	this work	previous work
Ru	-0.000015	
Cr	0.000050	$\pm 1.21[139]$
Re	0.0005	
V	-0.032	
Fe	2.299	4.00[115]
Co	1.627	3.00[140]
		1.55[141]
		1.58[142]
Zr	-0.000059	
Mn	5.0	5.0[140]
Mo	0.00018	

3.3.8.1 Magnetic moments of the X-doped $\text{Ru}_{48}\text{Cr}_{16}$ system

The magnetic moments of X (X = Zr, Mo, V, Mn, Fe, Co, Pt, Pd, Re) doped $\text{Ru}_{48}\text{Cr}_{16}$ have been investigated by first-principles calculations using the pseudopotentials plane wave method. CASTEP code has been used to calculate the magnetic moments, which is the total integrated spin density calculated with a smearing width of 0.001 eV. It is important to mention that the magnetic moment is sensitive to the smearing width.

We performed smearing width tests on one Mn doped $\text{Cr}_{48}\text{Ru}_{16}$ alloy, where we varied the width from 0.3 μB to 0.000025 μB . For each value, we then determined the magnetic moment, the results are provided in Table 3.7. The tests were performed in order to analyse the effect of smearing width on the magnetic moment of the system.

Table 3.9 : Calculated magnetic moments (per unit cell) of X doped Ru₄₈Cr₁₆ alloys.

System	Magnetic moments (μB)								
	Zr	Mo	V	Mn	Fe	Co	Pt	Pd	Re
Ru ₄₇ Cr ₁₆ X	-0.041	0.012	0.167	0.468	0.257	0.038	-0.250	-0.09	-0.248
Ru ₄₆ Cr ₁₆ X ₂	-0.341	-0.010	-0.056	0.359	0.159	0.029	-0.984	-	-0.002
Ru ₄₅ Cr ₁₆ X ₃	-0.007	-0.126	-0.003	0.384	0.826	0.030	0.033	-0.022	-0.371
Ru ₄₄ Cr ₁₆ X ₄	-0.125	-0.058	-0.006	0.274	0.246	-0.254	0.980	-	-0.008
Ru ₄₃ Cr ₁₆ X ₅	-0.05	-0.012	-0.124	0.569	-0.645	0.145	0.127	-0.092	-0.015
Ru ₄₂ Cr ₁₆ X ₆	-0.145	-0.098	-0.013	-0.002	0.285	0.115	-0.067	-	-0.004

From the Table 3.8, it can be noted that a decrease in the smearing width leads to an increased accuracy of the magnetic moment. We obtained the same value when the smearing widths of 0.001 eV and 0.0005 eV were considered. The magnetic moment does not change significantly beyond 0.01 μB smearing width [138].

The magnetic moments for X doped Ru₄₈Cr₁₆ systems were calculated using a smearing width of 0.001 eV. We also computed the magnetic moments of the individual atoms in ternary structures in order to have a better understanding of magnetism; Table 3.8 presents the atomic moments of studied alloys constituencies. Table 3.9 provides a detail comparison of the calculated magnetic moment for different doping concentration. For each dopant, six magnetic moments corresponding to one, two, three, four, five and six X dopants were calculated.

We obtained negative magnetic moments for all the studied Zr and Re doped systems as seen in Table 3.8. The values reveal a striking variation of magnetic moment with various dopants and doping concentration.

For low content of Mo, magnetic moment decreases from 0.012 μB to 0.010 μB and -0.0126 μB for one, two and three Mo atoms doped systems respectively, then increases from four Mo doped (-0.058 μB) to five Mo doped (-0.012 μB) structures, then finally decrease for six Mo doped alloy (-0.098 μB). It is predicted that the 4d Mo electron substitution in 4d Ru will lead to anti-ferromagnetic coupling between Cr-Mo because of their half-filled 4d orbitals. A study was carried out by G.L. High et al using electrical resistivity measurements to show that $(\text{Cr}_{1-x}\text{Ru}_x)_{78}\text{Mo}_{22}$ is always paramagnetic at all temperatures in a range of $0 \leq x \leq 1$ concentration of at % Ru and becomes antiferromagnetic in an array of $1 \leq x \leq 10$ concentration at % Ru [143].

In Mn doped systems, we detected high and low magnetization in one Mn doped (0.012 μB) and three Mn doped (-0.126 μB) systems respectively. The positive magnetic moments were obtained for one to five Mn doped systems, however a negative value was obtained for six Mn doped alloy. Positive values indicate that the most significant contribution comes from Mn with a moment of 5.0 μB that is higher than 4.0 μB , indicating that Mn is highly magnetized [144]. Whereas, a negative magnetic moment is due to Ru major contribution of -0.000015 μB as compared to Mn (5.0 μB) and Cr (0.000050 μB) as listed in Table 3.9.

In comparison to the magnetic moments of the other studied dopants in Table 3.9, it is noted that the Mn doped systems have high magnetic point at one Mn doped (0.468 μB), two Mn doped (0.359 μB) and five Mn doped (0.569 μB) systems.

In addition, we computed high magnetic moments for three Fe doped (0.826 μB) and six Fe doped (0.285 μB) systems. The calculated values for all the studied Fe doping concentrations are positive except for the five Fe doped alloy (-0.645 μB). The positive values are due to Fe spin contribution of 2.299 μB (listed in Table 3.9), this value does not compare well with the experimental value of 4 μB . Negative value is an indication that Ru contributed more than Cr and Fe; which caused an antiferromagnetic coupling between Fe-Cr due to their half-filled d-orbital [145]. Recent investigation highlighted that negative iron as antiferromagnetic system; based on the assumption that Fe has negative neighboring ions in a face centered cubic lattice.

Five Co doped $\text{Ru}_{48}\text{Cr}_{16}$ is highly magnetized (0.145 μB) whereas four Co doped system has low magnetization character of -0.254 μB . Lastly, an overall comparison of X doped $\text{Ru}_{48}\text{Cr}_{16}$ shows that four Pt doped system has the highest magnetic moment (0.980 μB) as compared to all dopants and for all concentrations. Hence, we assume that the coupling between Pt-Cr in Pt doped $\text{Ru}_{48}\text{Cr}_{16}$ structure can influence the system to behave like a ferrimagnetic material.

3.3.8.2. Magnetic moments of the X-doped $\text{Cr}_{48}\text{Ru}_{16}$ system

Table 3.10 : Calculated magnetic moments (per unit cell) of X doped Cr₄₈Ru₁₆ alloys.

System	Magnetic moments (μB)								
	Zr	Mo	V	Mn	Fe	Co	Pt	Pd	Re
Cr ₄₇ Ru ₁₆ X	0.993	2.100	0.249	2.001	0.244	1.005	1.530	1.995	2.980
Cr ₄₆ Ru ₁₆ X ₂	0.002	2.511	0.247	1.219	0.008	0.006	1.005	-0.441	0.499
Cr ₄₅ Ru ₁₆ X ₃	0.785	2.023	0.321	0.401	0.240	0.774	0.818	0.600	0.444
Cr ₄₄ Ru ₁₆ X ₄	0.374	0.068	0.000	0.700	1.109	1.444	-0.01	-0.121	0.502
Cr ₄₃ Ru ₁₆ X ₅	0.349	2.025	0.622	-0.091	0.748	0.232	0.255	-0.014	1.009
Cr ₄₂ Ru ₁₆ X ₆	0.338	0.919	0.303	-0.059	0.448	0.021	-0.129	-0.118	1.128

We further performed a number of calculations for the magnetic moments of the X-doped Cr₄₈Ru₁₆. The results are shown in Table 3.10, our computed magnetic moments for X (Zr, Mo, V, Pd, and Re) doped Cr₄₈Ru₁₆ are higher than the corresponding X doped Ru₄₈Cr₁₆. The values for five and six Mn doped, four and six Pt doped, two and six Co doped and one to three Fe doped Cr₄₈Ru₁₆ are lower than the Ru rich doped systems. From the two statements above, one can conclude that the studied Cr rich ternary alloys are generally more magnetic than the Ru rich ternaries. Our calculations predicted the positive magnetic moments for all the studied concentration of Zr, Mo, V, Fe, Co and Re doped Cr₄₈Ru₁₆ systems. The results for Zr and Re doped Cr₄₈Ru₁₆ are in contrast to the Ru rich system in Table 3.9 that indicated negative values for Zr and Re doped materials. Magnetic moments of Mo doped system increased from one to two Mo doped, and then decreased for three and four Mo doped, increased again for five Mo doped then finally

decrease for six Mo doped system. The two Mo doped is high in magnetization (2.511 μB) while four Mo doped system has low magnetization (0.068 μB). The positive values for all Mo doped systems are positive due to more contributions from Mo and Cr, we predict that Mo-Ru can couple ferromagnetically [146].

A zero magnetization was observed for four V doped Cr rich system. For low content of Mn (one to three Mn doped), it is evident that the addition of Mn content decreases the magnetic moment. The six Mn doped system is highly magnetized with a moment of 2.001 μB , while the five Mn doped system has a low magnetization character at -0.091 μB . The positive values for all Fe doped systems are influenced by high contribution of Fe as compared to Cr and Ru. Fe-Ru was predicted to couple Ferro-magnetically.

The results in Table 3.10 gives the magnetic moment of 1.444 μB and 0.006 μB for four Co doped and two Co doped systems respectively. We previously determined magnetic moment of atomic Co as 1.627 μB , this value does not compare well with the experimental value of 3 μB , however, there is a good agreement with theoretical values of 1.55 μB and 1.58 μB as indicated in Table 3.8. One, two, three and five Pt doped Cr rich systems have higher magnetic moments than the Pt doped Ru rich systems. These findings are influenced by highly magnetized antiferromagnetic Cr with a partial moment of 0.00005 μB .

One Pt doped system has high magnetization (1.53 μB) whereas six Pt doped show a sign of low magnetization character with -0.129 μB . When Pt bond with Cr they can form

alloy composition in a continuous mode between 100% Pt and 100% Cr. It was observed that Pt₃Cr alloy possess ferrimagnetism at a curie temperature of 170 °C [147].

The overall results of the comparison of the magnetic moments of all X-doped Cr₄₈Ru₁₆ indicate the high obtained magnetic moments as we increase the doping concentration as follows: One Re doped (2.980 μB), two Mo doped (2.511 μB), three Mo doped (2.023 μB), four Co doped (1.444 μB) five Mo doped (2.025 μB) and six Re doped (1.128 μB). One Re doped system is highly magnetized as compared to all X doped Cr₄₈Ru₁₆ systems. In the next chapter, we discuss the density of states in order to observe the d orbitals contribution of each metal around the Fermi energy.

CHAPTER 4

Electronic properties

4.1 Introduction

Density of states (DOS) of a system is defined as the number of different states at a particular energy level that electrons are allowed to occupy. A high DOS at a specific energy level means that there are many states available for occupation. A DOS of zero means that no states can be occupied at that energy level. The Fermi level is one of the important concepts in the solid-state physics of metals, its position of the Fermi level with the relation to the band energy levels is a crucial factor in determining the stability or the instability of the metal alloys. In this chapter, we discuss in more detail the DOS of metallic Ru, Cr, Fe, Pt, V and Mo. In addition, we will also discuss the DOS of six Fe, V, Mn and Mo doped $\text{Ru}_{48}\text{Cr}_{16}$ and $\text{Cr}_{48}\text{Ru}_{16}$ alloys to provide more information about the investigated systems.

4.1.1 Methodology

Calculations have been performed within the DFT and the pseudo-potential approach, using the CASTEP package. The smearing width of 0.1 eV was used to ensure the convergence of the self-consistence procedure and eradicate discontinuity in the energy variation as the electron band passes the Fermi level. The ultra-soft pseudopotential was used to describe the electron-core interaction. The DOS calculations

3 IIIB 3B	4 IVB 4B	5 VB 5B	6 VIB 6B	7 VIIB 7B	8 VIII 8	9 VIII 8	10 VIII 8	11 IB 1B	12 IIB 2B
21 Sc Scandium 44.956	22 Ti Titanium 47.88	23 V Vanadium 50.942	24 Cr Chromium 51.996	25 Mn Manganese 54.938	26 Fe Iron 55.933	27 Co Cobalt 58.933	28 Ni Nickel 58.693	29 Cu Copper 63.546	30 Zn Zinc 65.39
39 Y Yttrium 88.906	40 Zr Zirconium 91.224	41 Nb Niobium 92.906	42 Mo Molybdenum 95.94	43 Tc Technetium 98.907	44 Ru Ruthenium 101.07	45 Rh Rhodium 102.906	46 Pd Palladium 106.42	47 Ag Silver 107.868	48 Cd Cadmium 112.411
57-71	72 Hf Hafnium 178.49	73 Ta Tantalum 180.948	74 W Tungsten 183.85	75 Re Rhenium 186.207	76 Os Osmium 190.23	77 Ir Iridium 192.22	78 Pt Platinum 195.08	79 Au Gold 196.967	80 Hg Mercury 200.59
89-103	104 Rf Rutherfordium [261]	105 Db Dubnium [262]	106 Sg Seaborgium [266]	107 Bh Bohrium [264]	108 Hs Hassium [269]	109 Mt Meitnerium [268]	110 Ds Darmstadtium [269]	111 Rg Roentgenium [272]	112 Cn Copernicium [277]

Figure 4.1 : Periodic table for transition metals

were performed for Ru = [Kr] 4d⁶ 5s², Cr = [Ar] 3d⁵ 4s¹, V = [Ar] 3d³ 4s², Mn = [Ar] 3d⁵ 4s², Fe = [Ar] 3d⁶ 4s² and Mo = [Kr] 4d⁵ 5s¹. The studied metals belong to the 1st and 2nd rows of the transition metals in the periodic table as shown in Figure 4.1. V, Cr, Mn and Fe belong to the 1st row, while Mo and Ru belong to the 2nd row. We will also present the DOS of the predicted thermodynamically stable structures; the six Mn, Fe and Mo doped Ru Rich and Cr Rich alloys. Mo and Cr possess half- filled d-orbital that have high chance of attaining stability when alloyed with other materials. The six V doped system will be presented for a comparison purpose.

4.1.2 Density of states for pure metals

The density of state for metallic Cr is displayed in Figure 4.2. From the DOS we can clearly depict the continuity of the density of states, there is no band gap found at the Fermi level as the valence and conduction bands overlap significantly near the Fermi level. These observations indicate that Cr exhibit the metallic character. The d states contribute more to the DOS of Cr than the s and p states. The high peak of the valence band DOS is located at ≈ 2.0 eV. The main peak of the valence band DOS is higher than the peaks of the conduction band DOS.

Figure 4.3 shows the calculated density of states of Ru. The main contribution in both the valence and conduction bands emanate from the d-states. The total DOS of metallic Ru consist of a Fermi level that falls into a pseudo-gap hence this metal may have stability characteristics [148,149,150].

From the DOS of metallic Mn is Figure 4.4 we note fewer bands below the Fermi as compared to a visible large number of bands in the conduction region. There is an overlap between the valence and conduction bands. The main peak of the total and partial DOS of Mn is located at the Fermi level; this is due to the 3d-Mn electrons. However, the bands at the Fermi level may be broken by doping. The states around 2.3 eV and 4.1 eV are the p electrons of the Mn atoms in the conduction band. The total DOS indicate two broad peaks at ≈ 3.5 eV and 7.6 eV in the conduction region. In conclusion, we observed a semi-metal character for Mn material.

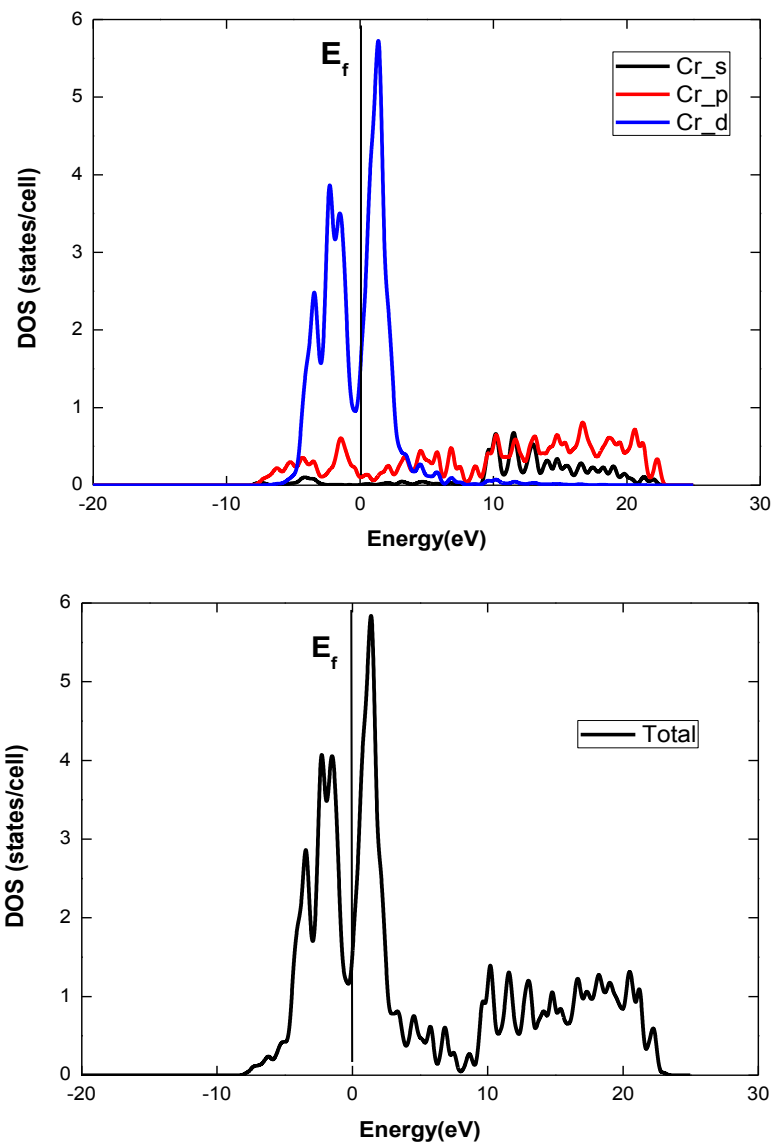


Figure 4.2 : The calculated partial and total density of states for metallic Cr. Fermi energy corresponds to the solid line (E_f).

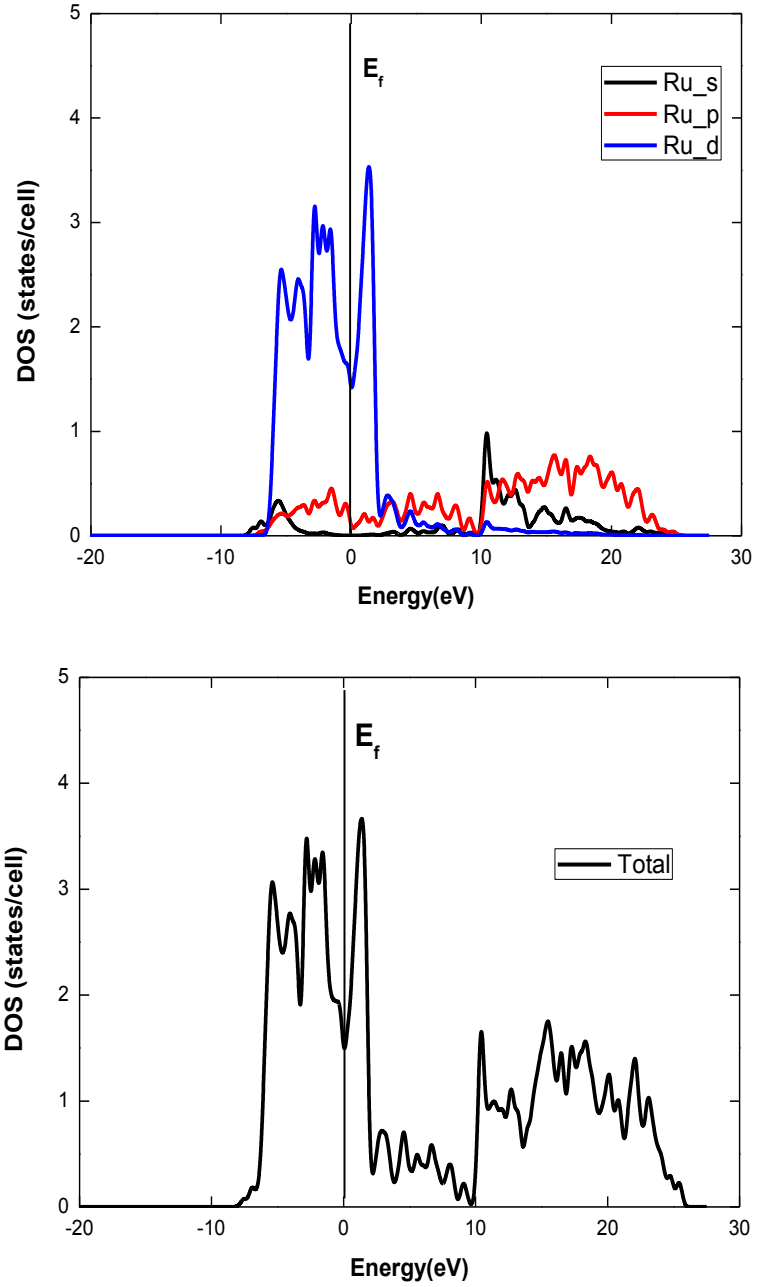


Figure 4.3 : Partial and total density of states (DOS) of pure Ru metal. A solid line (E_f) shows the Fermi energy.

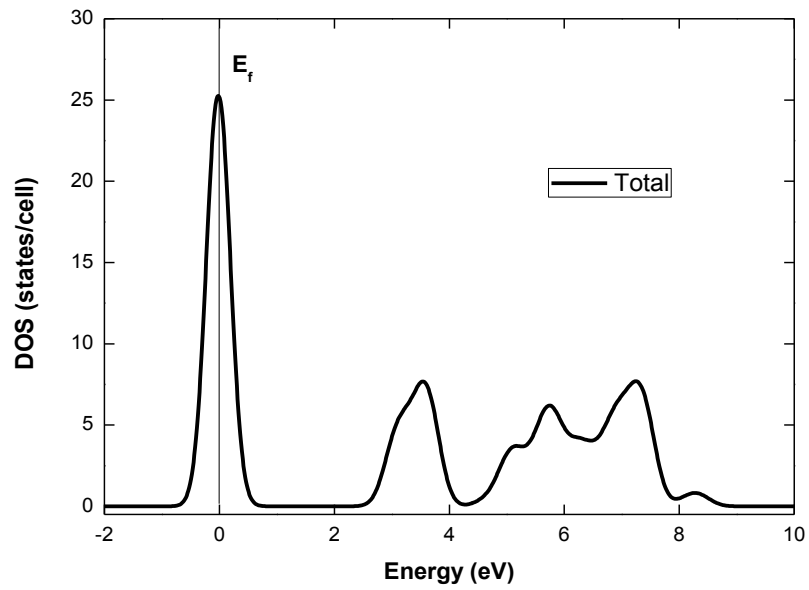
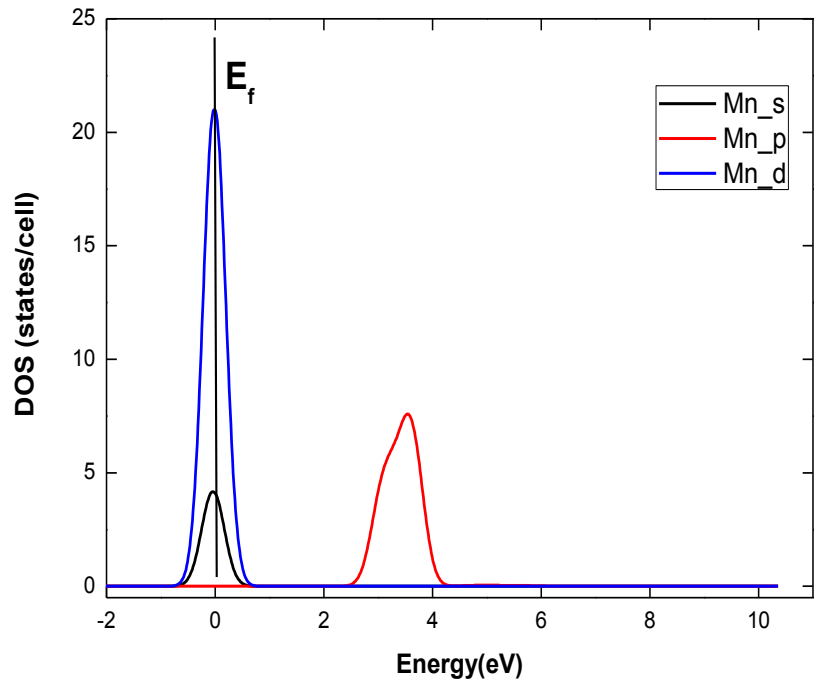


Figure 4.4 : Partial and total DOS of pure metallic Mn.

Figure 4.5 presents the DOS of metallic Fe. The Fermi energy level (E_f) falls on a largest peak located in the conduction side as shown by the DOS of metallic Fe. This can imply that the Fe metal exhibit the ductility characters [151-152]. We note a very small contribution of the Fe s and p states as compared to the d states. High DOS near the Fermi energy level is observed; this is due to the d-state contribution.

Figure 4.6 shows the calculated DOS of metallic Mo. Both the valence and conduction bands are mainly dominated by the Mo d-states. The main peak in the conduction band is slightly higher than the main peak in the valence band. We observed interesting features from the density of states of Mo; the narrow dip and broad dip were observed in the DOS at valence band and conduction band respectively. The Fermi level falls on a smaller peak together with the broad dip indicating the material's stable behavior [151-152].

From the DOS of metallic V in Figure 4.7 we note that not all the bonding states are filled as the E_f lies on the left of the narrow pseudo-gap [151-157]. The V d-states stretch from -3 eV to 5 eV. The contribution from the V s and p states is low. We observed a smaller main peak in the valence band compared to the conduction band. There is a visible separation of two d-state peaks by the narrow dip (pseudo-gap). We will discuss the density of states of the binary and ternary alloys in the next sections.

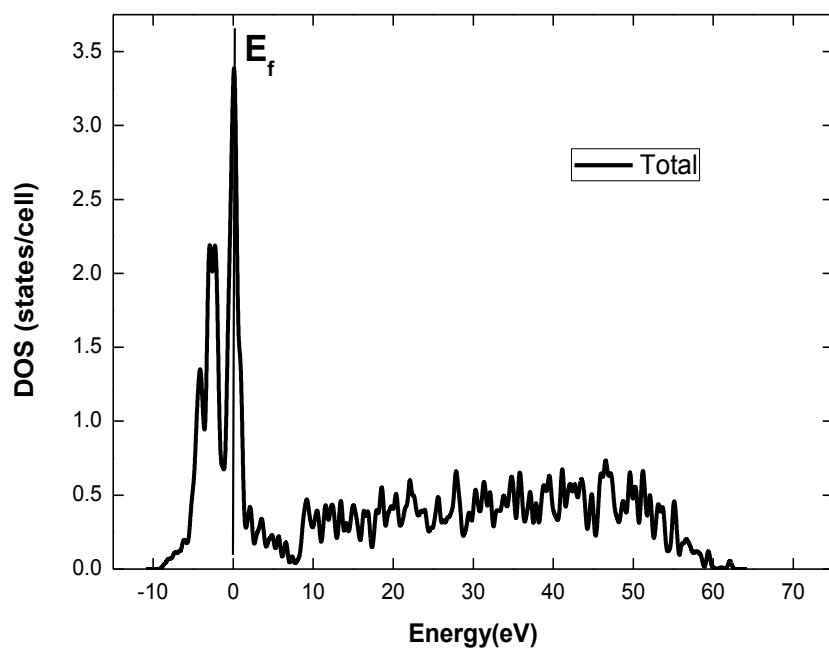
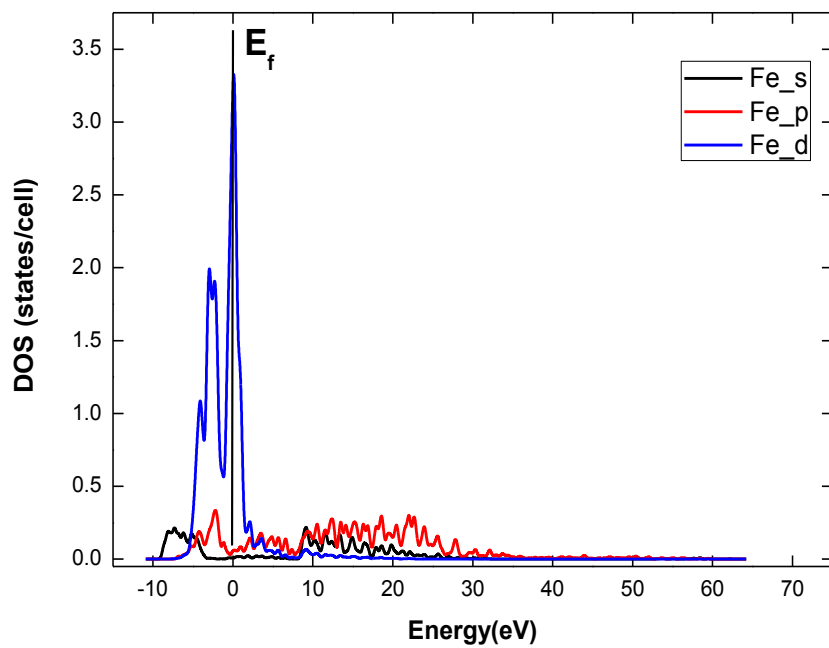


Figure 4.5 : Partial and total density of states (DOS) for metallic Fe. A solid line presents the Fermi energy (E_f).

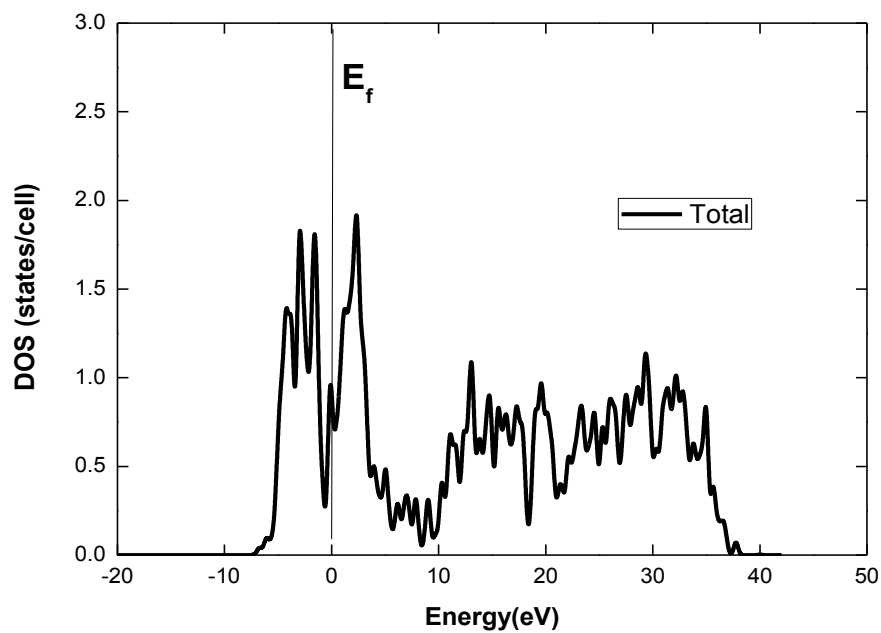
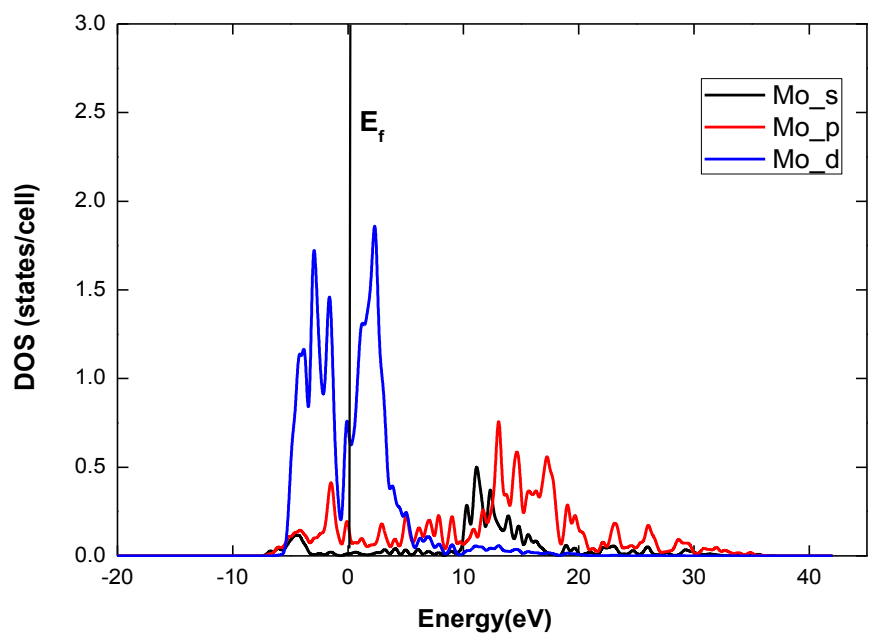


Figure 4.6 : Total and partial densities of states for pure Mo metal. Zero energy corresponds to Fermi energy.

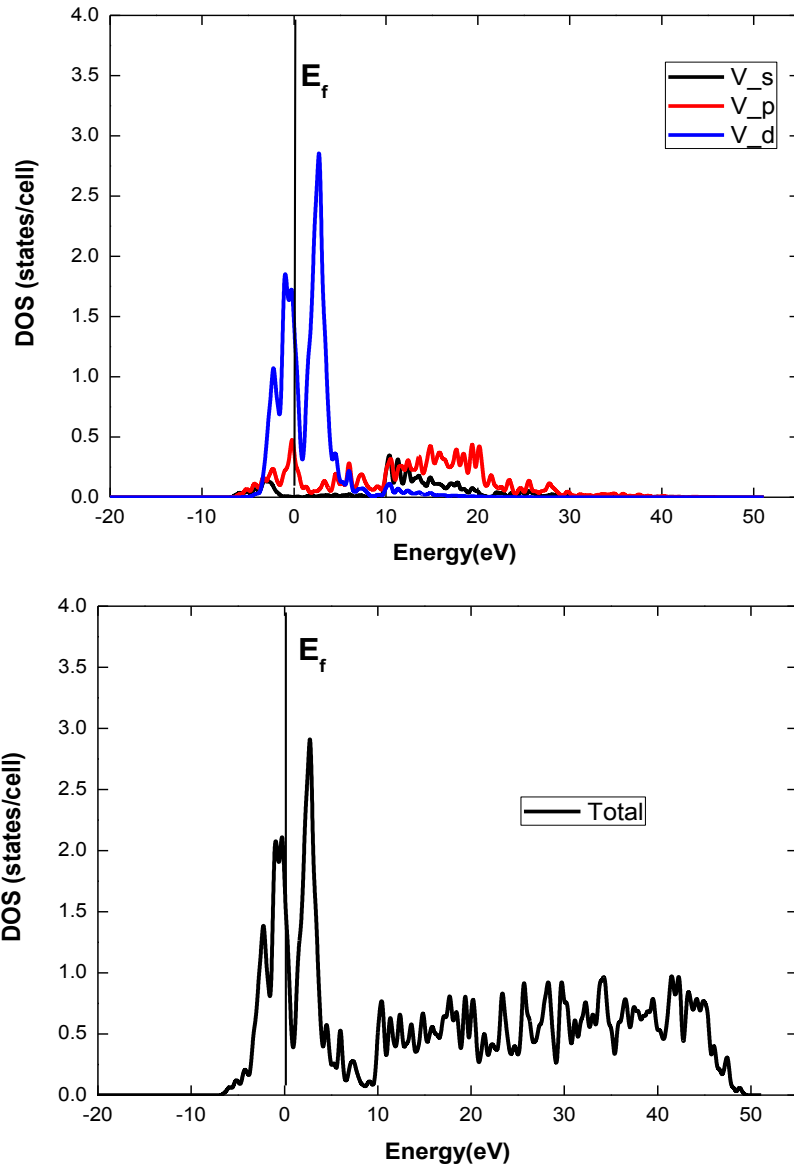


Figure 4.7 : Total and partial DOS of transition metal V. The Fermi energy (E_f) indicates zero energy.

4.1.3 Density of states for the undoped $\text{Cr}_{48}\text{Ru}_{16}$ and $\text{Ru}_{48}\text{Cr}_{16}$ Alloys

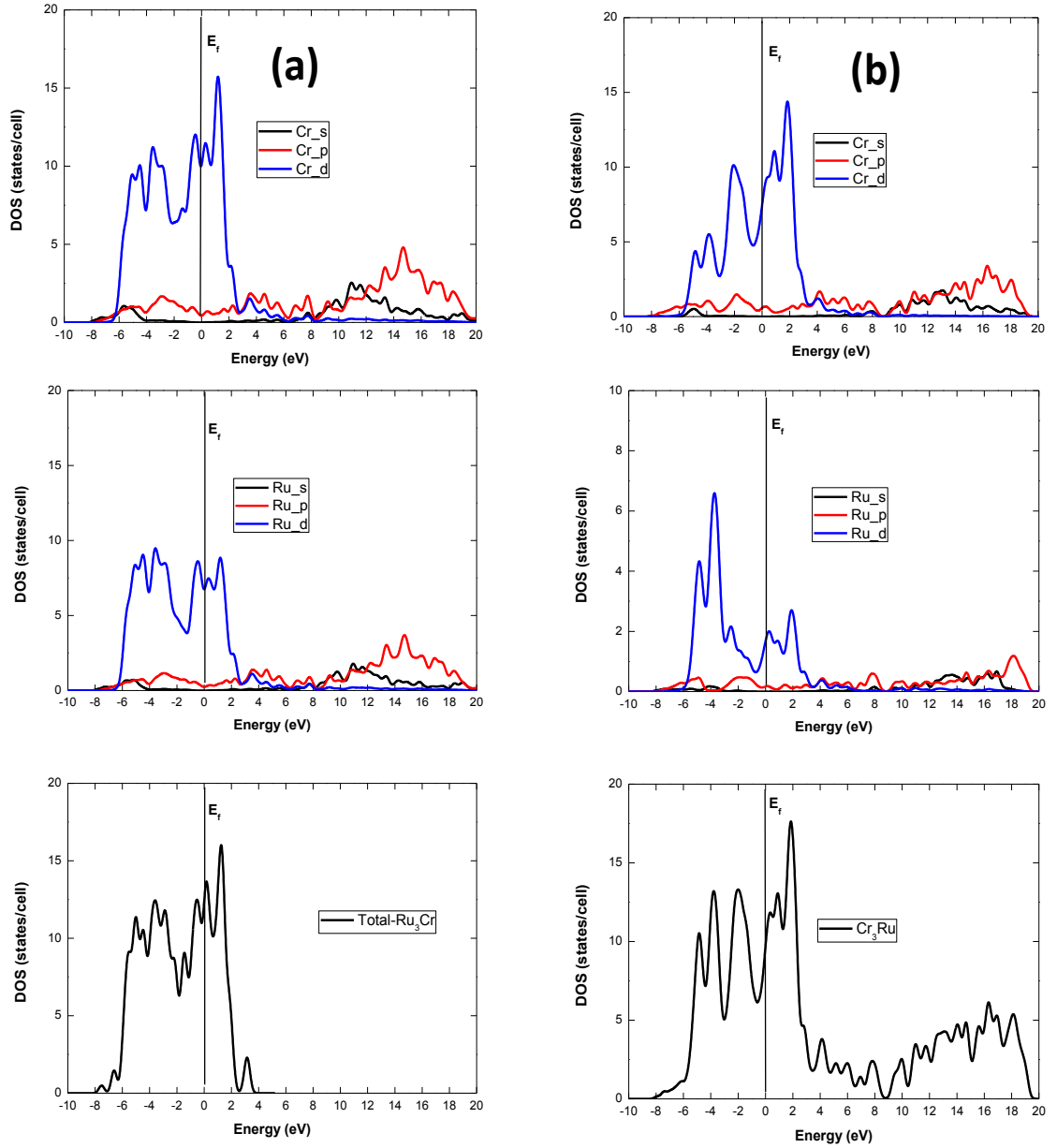


Figure 4.8 : Total and partial DOS for undoped (a) $\text{Ru}_{48}\text{Cr}_{16}$ and (b) $\text{Cr}_{48}\text{Ru}_{16}$ structures. The Fermi energy indicates zero energy.

In Figures 4.8 (a) and (b) a comparison of the calculated density of states for the undoped $\text{Ru}_{48}\text{Cr}_{16}$ and $\text{Cr}_{48}\text{Ru}_{16}$ compounds are shown respectively. The total density of states (TDOS) of the Ru rich and Cr rich binary alloys, and the partial density of states (PDOS) of Ru and Cr are displayed. The solid lines in all the TDOS and PDOS represent the Fermi level. It can be seen from both DOS that there is no band gap at the Fermi level as valence band and conduction bands overlap near the Fermi level, as a result the $\text{Ru}_{48}\text{Cr}_{16}$ and $\text{Cr}_{48}\text{Ru}_{16}$ exhibits the metallic character. All the DOS curves in Figure 4.8 mainly originates from the Cr (3d) and Ru (4d) states, with small contribution from their s and p states.

It is clear from Figure 4.8 (b) that the total DOS of $\text{Cr}_{48}\text{Ru}_{16}$ alloy consist more states in the conduction band than those in TDOS of $\text{Ru}_{48}\text{Cr}_{16}$. We observed low electron density of states at the Fermi level from both the TDOS and PDOS of $\text{Cr}_{48}\text{Ru}_{16}$ and Cr and Ru respectively as shown in Figure 4.8 (b). Meanwhile a higher electron density of states was observed near the Fermi level in the TDOS of $\text{Ru}_{48}\text{Cr}_{16}$ and PDOS of Cr and Ru of Ru rich alloy as indicated in Figure 4.8(a). In both cases, we noted that the PDOS of Ru have fewer states at Fermi level as compared to the PDOS of Cr.

In the PDOS curve of Ru and Cr in $\text{Ru}_{48}\text{Cr}_{16}$ in Figure 4.8(a), the Fermi energy level (E_f) falls on top of a dip due to the presence of their d states. Position of the E_f in relation to the band energy levels is crucial in determining the electrical properties of solids. When we compare the position of E_f in DOS curves of $\text{Cr}_{48}\text{Ru}_{16}$ to $\text{Ru}_{48}\text{Cr}_{16}$, we observed a small shift of E_f to the left in the TDOS and PDOS curves of $\text{Cr}_{48}\text{Ru}_{16}$. This shift gives a large variation in the number of states at the Fermi level that can be used to determine the

stability of alloys. In the next section, we investigate the effect of doping on the electronic stability of $\text{Cr}_{48}\text{Ru}_{16}$ and $\text{Ru}_{48}\text{Cr}_{16}$ alloys.

4.1.4 Density of states for the X- doped $\text{Cr}_{48}\text{Ru}_{16}$ and $\text{Ru}_{48}\text{Cr}_{16}$ Alloys:

Ternary alloying may strengthen the electronic properties of the systems. In this section, we investigate the effect of Mn, Fe, Mo and V dopants on the electronic structure of the $\text{Cr}_{48}\text{Ru}_{16}$ and $\text{Ru}_{48}\text{Cr}_{16}$ alloys. We calculated the density of states for the most stable configurations of the X-(Mn, Fe, V and Mo) doped $\text{Cr}_{48}\text{Ru}_{16}$ and $\text{Ru}_{48}\text{Cr}_{16}$ systems. In both cases, the six X atom-doped systems were predicted as the most thermodynamically stable ternaries. We will also consider the systems doped with six V atoms to develop a better understanding of the electronic properties.

Figure 4.9 (a) and (b) show the calculated TDOS and PDOS of $\text{Ru}_{42}\text{Cr}_{16}\text{Fe}_6$ and $\text{Cr}_{42}\text{Ru}_{16}\text{Fe}_6$ respectively. From the PDOS of Ru and Cr in $\text{Ru}_{42}\text{Cr}_{16}\text{Fe}_6$ we noted that E_f lies in a pseudo-gap. The TDOS of the Ru rich ternary exhibits the same behavior. The E_f in the PDOS and TDOS of Cr rich alloys shifts to the right of the pseudo-gap. As a result, the value of $N(E_f)$ in TDOS of Cr rich alloy is slightly higher than in Ru rich system. The PDOS and TDOS of $\text{Ru}_{42}\text{Cr}_{16}\text{Mo}_6$ and $\text{Cr}_{42}\text{Ru}_{16}\text{Mo}_6$ structures are shown in Figure 4.10 (a) and Figure 4.10 (b) respectively. The main contribution for both configurations comes from the d states of Ru, Cr and Mo atoms. The DOS and PDOS curves of the Mo-doped Ru rich alloy reveal no peaks in the conduction band. The previous statement implies that there is no energy difference between the main peaks of the valence and conduction band of the $\text{Ru}_{42}\text{Cr}_{16}\text{Mo}_6$ ternary alloy. However, the energy

difference between the main peak of valence band and that of conduction band in the TDOS of $\text{Cr}_{42}\text{Ru}_{16}\text{Mo}_6$ was found to be 3.6 eV as shown in Figure 4.10 (b). The DOS of $\text{Ru}_{42}\text{Cr}_{16}\text{Mn}_6$ and $\text{Cr}_{42}\text{Ru}_{16}\text{Mn}_6$ structures are presented in Figure 4.11 (a) and Figure 4.11 (b) respectively. Most of the DOS lie in the valence band for both configurations; the DOS are mainly attributed to the d states of Cr and Ru. It is clear from the PDOS in $\text{Cr}_{42}\text{Ru}_{16}\text{Mn}_6$ that the s, p and d states are moved to lower energy region as compared to the $\text{Ru}_{42}\text{Cr}_{16}\text{Mn}_6$. In addition, the conduction band has shifted to low energy range. From the results of PDOS of Mn in Figure 4.11 (b), we note a narrow peak in the conduction band at 0.5 eV.

The TDOS and PDOS plots for $\text{Ru}_{42}\text{Cr}_{16}\text{V}_6$ and $\text{Cr}_{42}\text{Ru}_{16}\text{V}_6$ are displayed in Figure 4.12 (a) and (b) respectively. The valence band of both V-doped alloys mainly consists of the d states of V, Cr and Ru. The main peak in the PDOS curve of V in Cr rich alloy is higher compared to the PDOS of V in Ru rich alloys.

In general, the conduction band from all the DOS of $\text{Ru}_{42}\text{Cr}_{16}\text{Mo}_6$ is narrower than the DOS of the studied X-doped materials. In both configurations of Mo-doped systems, most of electrons are accumulated in the lower energy region as compared to Mn and Fe-doped systems in Figures 4.11 and 4.9 respectively, indicating higher level of stability for Mo-doped systems. To the best of our knowledge, there are no previous findings to compare with our computed results for the density of states of the six Mn, Mo, V and Fe-doped systems. In the next chapter, we present the results of the calculated elastic properties of the studied alloys.

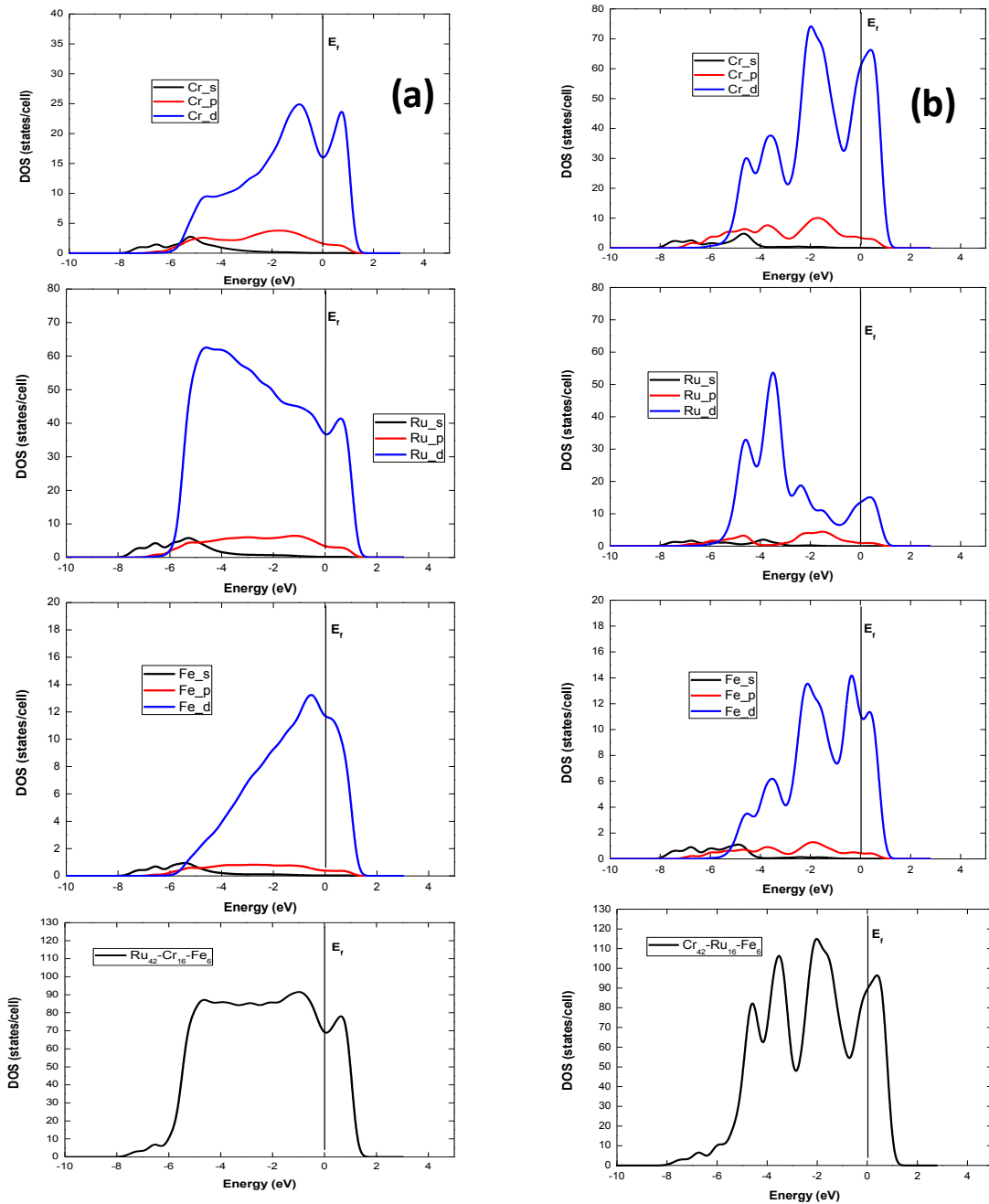


Figure 4.9: Total and partial density of states for (a) $\text{Ru}_{42}\text{Cr}_{16}\text{Fe}_6$ and (b) $\text{Cr}_{42}\text{Ru}_{16}\text{Fe}_6$ alloys.

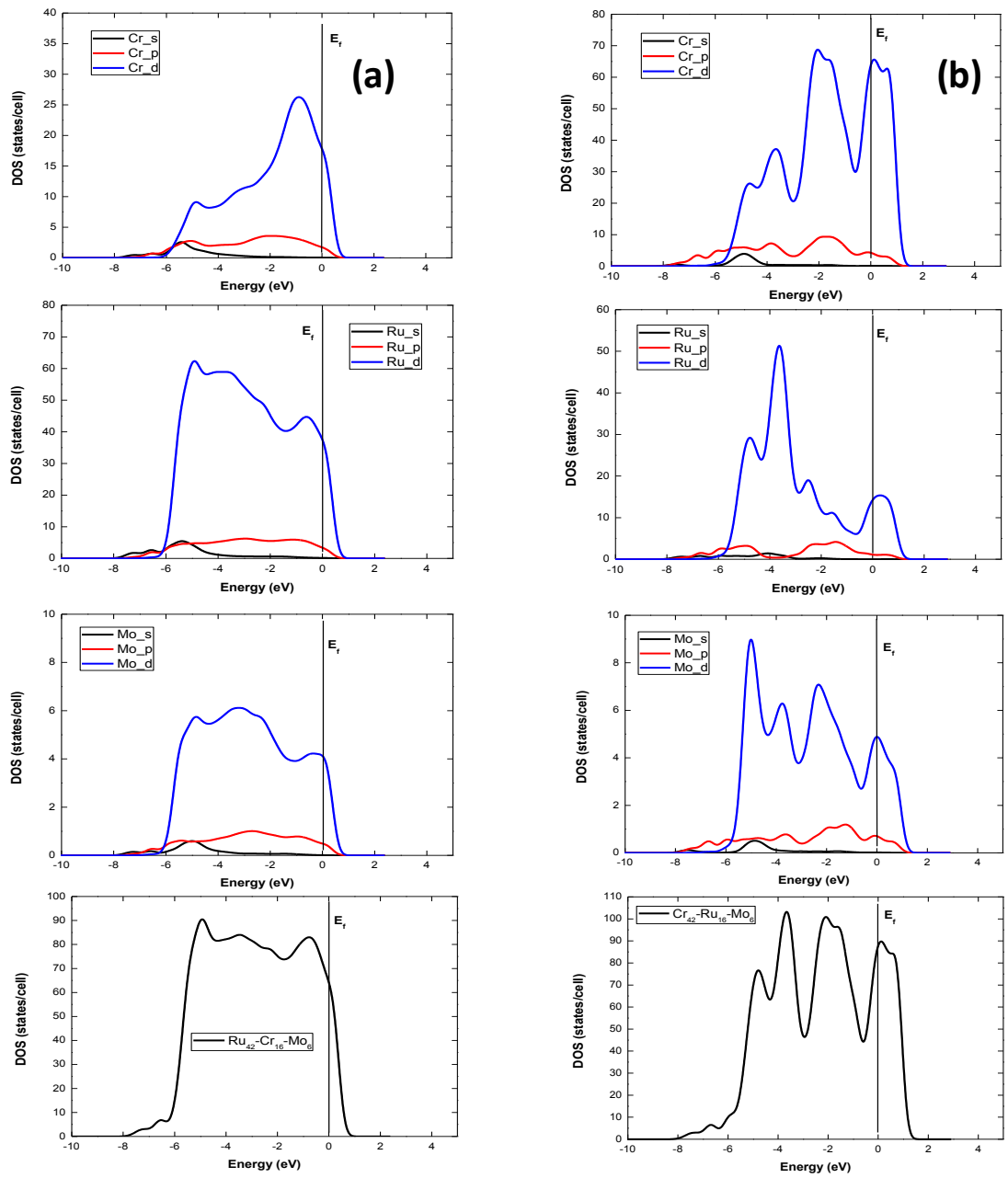


Figure 4.10: Total and partial DOS for (a) $\text{Ru}_{42}\text{Cr}_{16}\text{Mo}_6$ and (b) $\text{Cr}_{42}\text{Ru}_{16}\text{Mo}_6$ alloys. A solid line represents the Fermi energy.

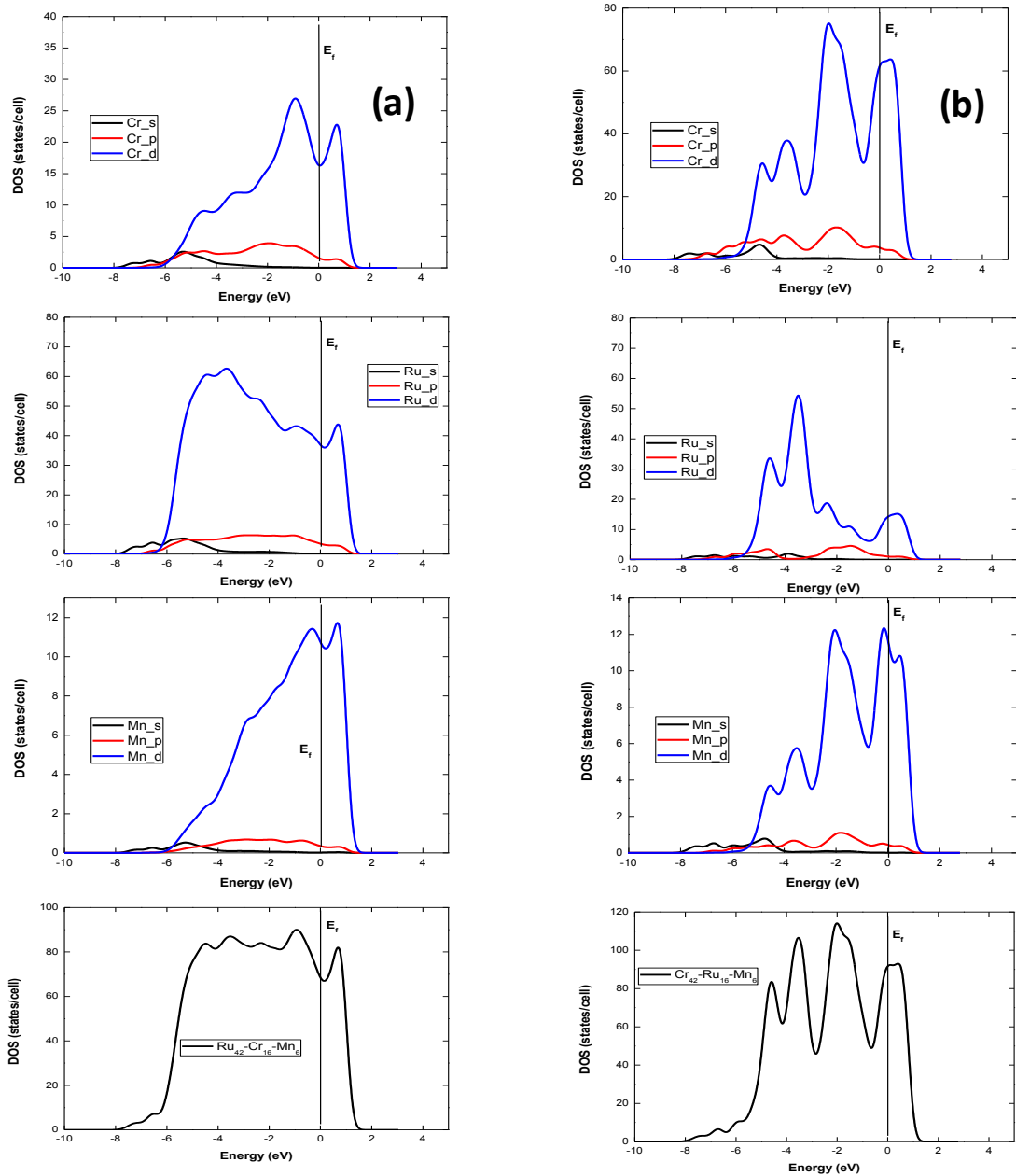


Figure 4.11: The partial and total density of states for (a) $\text{Ru}_{42}\text{Cr}_{16}\text{Mn}_6$ and (b) $\text{Cr}_{42}\text{Ru}_{16}\text{Mn}_6$ alloys. A solid line indicates the Fermi energy.

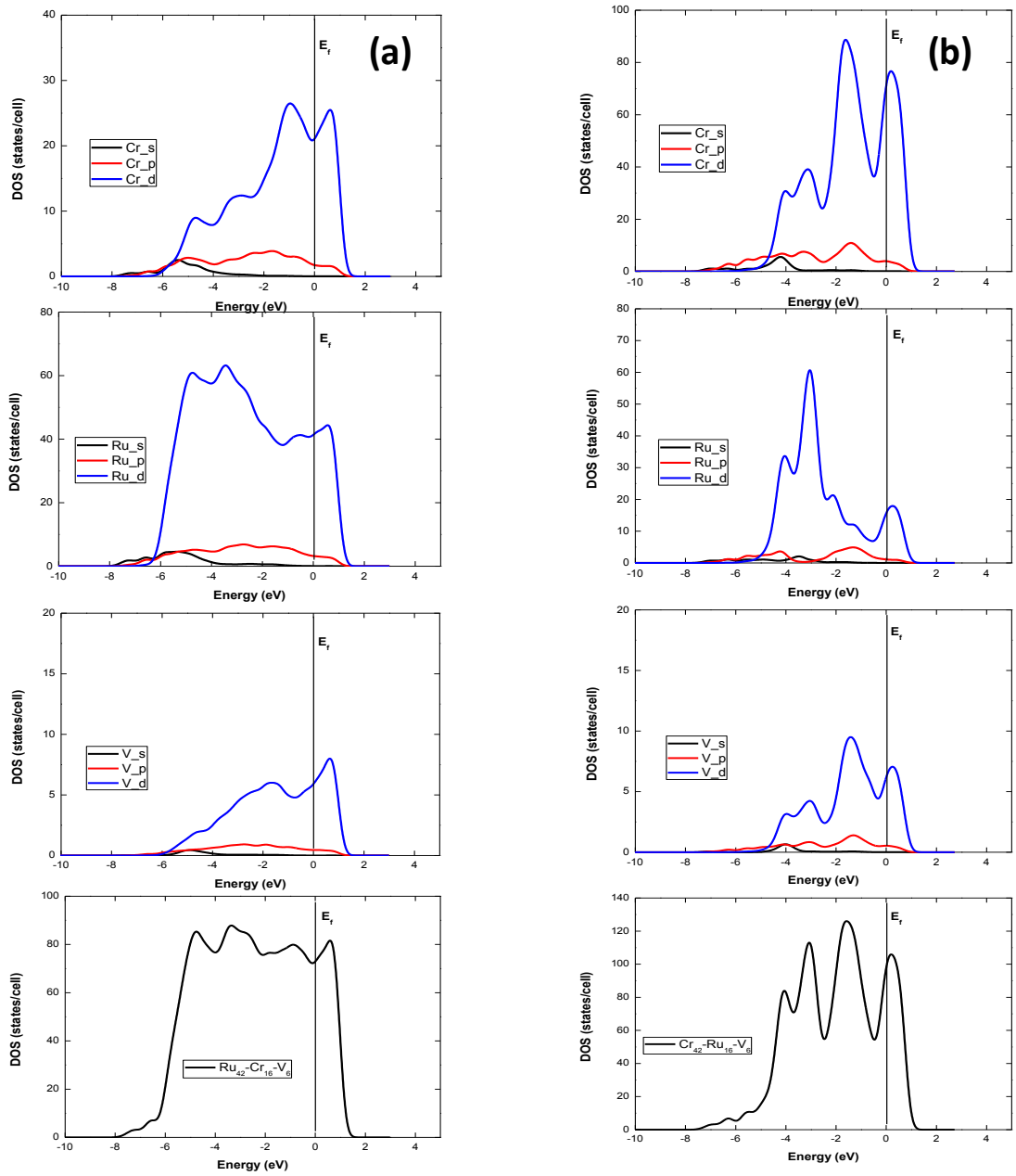


Figure 4.12: Partial and total density of states for (a) $\text{Ru}_{42}\text{Cr}_{16}\text{V}_6$ and (b) $\text{Cr}_{42}\text{Ru}_{16}\text{V}_6$ alloys. The position of the Fermi level is at 0 eV.

Chapter 5

Elastic constants

5.1 Introduction

Elastic properties are of importance to the solids because they relate to different solid-state properties such as interatomic potential, equation of state and phonon spectra. In addition, these properties are linked thermodynamically to the specific heat, melting points and thermal expansion. Furthermore, these elastic properties of a material are well known to be used in characterizing the structural stability and mechanical deformation under external load [158].

Within these properties we are more interested in calculating the, bulk, shear, Young's modulus and Poisson's ratio of pure metals, Ru_3Cr , Cr_3Ru , $\text{Cr}_{42}\text{Ru}_{16}\text{X}_6$ and $\text{Ru}_{42}\text{Cr}_{16}\text{X}_6$ (where X = Fe, Mn and Mo) systems. The bulk modulus represent the average bond strength of a material, shear modulus shows the material's response to shear stress, while Young's modulus is used to determine the stiffness of a material. In addition, the ratio of bulk to shear will assist in order to tell if the material is ductile or brittle.

Important information will be extracted from the properties above (bulk, shear and Young's modulus) of how stable the structures are, furthermore the Stress-Strain relation [159] will be used to compute the elastic constants. In addition, these elastic constants have a stability criterion obtained from Born mechanical stability for cubic, hexagonal and orthorhombic. However, in this study we will concentrate on cubic systems as this are what our structures possess. Moreover, for cubic we have (C_{11} , C_{12} and C_{44}) and the

conditions are stated below as follows: $C_{11} > 0$, $C_{12} > 0$, $C_{11} - C_{12} > 0$, $C_{44} > 0$ [160]. The C_{44} and C_{66} are elastic constants which are more important in giving data for stability of other systems with regard to the hardness of the material. The Poisson's ratio will be calculated using the formula below.

$$\nu = \left[\frac{3B_{VRH} - 2G_{VRH}}{2(3B_{VRH} + G_{VRH})} \right]$$

Where ν is the Poisson's ratio, B_{VRH} is the average bulk for Voigt, Reuss and Hill, and G_{VRH} is the average shear modulus of Voigt, Reuss and Hill. Furthermore, the bulk, shear and Young modulus will be calculated by (CASTEP) code based on density functional theory. From the bulk modulus we will detect the resistance to the change in volume, shear modulus will detect the stiffness on the material and the young modulus will information about the elasticity of the material. In this section the elastic constants, bulk, shear, young moduli, ratio of Bulk to shear and Poisson ratio of pure metals, $A_{15}Cr_3Ru$, $A_{15}Ru_3Cr$, $A_{15}Cr_{42}X_6Ru_{16}$ and $A_{15}Ru_{42}X_6Cr_{16}$ ($X=Mo$, Mn and Fe) systems are analysed. Table 5.1 show the computed elastic constants for the systems mentioned above.

Table 5.1 : Calculated elastic constant C_{ij} in GPa of Pure metals, undoped and X6 doped $A15Ru_{48}Cr_{16}$ and $A15Cr_{48}Ru_{16}$ where (X = Mo, Mn and Fe)

System	C_{11}	C_{12}	C_{13}	C_{16}	C_{33}	C_{44}	C_{66}	$C_{12}-C_{44}$
V	306.13	130.51				94.60		35.91
	281.72[153]	14.63[153]				36.09[153]		88.54[153]
Mo	457.75	163.59						93.75
Mn	5.22	5.21				-0.05		5.26
Ru	569.74	179.18				164.20		14.98
	569.00[15]	223.00[15]				173.00[15]		13.7[15]
Cr	639.39	76.79				63.09		13.7
$Ru_{48}Cr_{16}$	439.75	195.89				44.71		151.18
$Cr_{48}Ru_{16}$	581.66	209.49				128.23		81.26
$Ru_{42}Cr_{16}Mo_6$	426.70	210.38	224.87	-0.141	414.67	91.71	97.71	118.67
$Cr_{42}Ru_{16}Mo_6$	518.06	197.63	194.25	0.158	516.39	103.14	103.66	94.49
$Ru_{42}Cr_{16}Mn_6$	348.33	216.73	180.89	2.655	377.89	73.08	78.71	143.65
$Cr_{42}Ru_{16}Mn_6$	417.44	131.48	146.76	-0.260	454.75	99.07	99.28	32.41
$Ru_{42}Cr_{16}Fe_6$	343.22	190.93	194.87	-1.944	355.78	96.57	98.16	94.36
$Cr_{42}Ru_{16}Fe_6$	424.72	169.70	163.78	-0.545	424.82	87.49	87.17	82.21

5.1.1 Elastic constants of Pure metals and undoped $Ru_{48}Cr_{16}$ and $Cr_{48}Ru_{16}$ systems

The elastic constants of the pure metals were computed and presented in Table 5.1; we noted that all the elastic constants satisfy the Born mechanical stability criterion. Ruthenium has high C_{44} elastic constant value of 164.20 GPa that compare very well with Popoola et.al [15] results, while Manganese has the lowest value of -0.05 GPa.

In comparing the results in Table 5.1 for the Ru₄₈Cr₁₆ and Cr₄₈Ru₁₆ systems, it was found that C₁₁, C₁₂ and C₄₄ are increasing from A15 Ru₄₈Cr₁₆ to A15 Cr₄₈Ru₁₆. However, the C₄₄ in both configurations was observed to have the smaller values than the C₁₁ and C₁₂. The C₄₄ elastic constant is very essential in determining the hardness of a material. The Cr₄₈Ru₁₆ has a large value of C₄₄, which implies that it has strong ability in resisting shear distortion in materials.

More over the C₁₁ and C₁₂ constants of Cr₄₈Ru₁₆ are higher than Ru₄₈Cr₁₆ meaning these materials are strong against compression in a, b and c axis. The Cauchy pressure calculated as (C₁₂-C₄₄) helps to describe the angular character of atomic bonding in metals [161] and show ductility or brittleness of a material. In Table 5.1, the Cauchy pressure values of Ru₄₈Cr₁₆ and Cr₄₈Ru₁₆ systems are positive meaning that there is a sign of metallic bonding and ductility. Furthermore, they follow a Cauchy pressure trend of

$$\text{A15 Cr}_{48}\text{Ru}_{16} < \text{A15 Ru}_{48}\text{Cr}_{16}$$

5.1.2 Elastic constants of X-doped Ru₄₈Cr₁₆ and Cr₄₈Ru₁₆ systems

The elastic constants for the six X atoms doped Ru₄₈Cr₁₆ and Cr₄₈Ru₁₆ structures (X = Mo, Mn and Fe) are discussed in details. The C₄₄ elastic constant play a vital role in describing the hardness of a material. We noted a decreasing trend of C₄₄ from six Mo-doped to six Mn-doped then later, to six Fe-doped Cr₄₈Ru₁₆. It can be seen that the six Cr₄₂Ru₁₆Mo₆ has a high C₄₄ constant of 103.14 GPa, whereas the Cr₄₂Ru₁₆Fe₆ has the lowest value of 87.49 GPa. Further, The Cauchy pressure values are positive predicting

the possibility of metallic bonding. The six Mo-doped $\text{Cr}_{48}\text{Ru}_{16}$ has the highest C_{44} and Cauchy pressure. The trend of decreasing Cauchy pressure for Cr rich alloys is as follows

$$\text{six Mo-doped} > \text{six Fe-doped} > \text{six Mn-doped}$$

For the six X-doped $\text{Ru}_{48}\text{Cr}_{16}$ systems shown in Table 5.1, it is clearly seen that six Fe-doped $\text{Ru}_{48}\text{Cr}_{16}$ has the highest C_{44} elastic constant of 96.57 GPa whilst the six Mn-doped $\text{Ru}_{48}\text{Cr}_{16}$ has the lowest C_{44} of 73.08 GPa. The Cauchy pressure of six Mn-doped $\text{Ru}_{48}\text{Cr}_{16}$ is higher (143.65 GPa) whereas the six Fe-doped $\text{Ru}_{48}\text{Cr}_{16}$ has a lower value of (94.36 GPa). In addition, the Cauchy pressure trend for Ru rich alloys shown below:

$$\text{six Mn-doped} > \text{six Mo-doped} > \text{six Fe-doped}$$

Comparing the six X-doped $\text{Ru}_{48}\text{Cr}_{16}$ and $\text{Cr}_{48}\text{Ru}_{16}$ systems, we observed that the elastic constants C_{11} and C_{44} and C_{66} for six Mo and six Mn-doped $\text{Ru}_{48}\text{Cr}_{16}$ are lower compared to those of the six Mo and six Mn-doped $\text{Cr}_{48}\text{Ru}_{16}$ systems; however, the C_{12} values are decreasing from Ru rich to Cr rich alloys in all configurations. From the above statements it is clear that Mo, Mn doped $\text{Cr}_{48}\text{Ru}_{16}$ can resist shear distortion easily than Mo, Mn, Fe doped $\text{Ru}_{48}\text{Cr}_{16}$ [162-163]. For Fe doped $\text{Ru}_{48}\text{Cr}_{16}$ system tend to have the same trend for C_{12} values decreasing with increasing C_{11} but opposite trend have been noticed for C_{44} and C_{66} .

Table 5.2 : The calculated average bulk (B), shear (G) and young (E) modulus in GPa and Poisson's ratio (ν) of Pure metals, undoped and X_6 doped $Ru_{48}Cr_{16}$, $Cr_{48}Ru_{16}$ systems where ($X = Fe, Mo$ and Mn)

System	B	G	E	B/G	ν
V	189.05	91.82	127.84	2.06	0.29
	176.99[158]	49.56[158]	135.98[158]	3.57[158]	
Mo	261.65	112.37	186.73	2.33	0.31
Mn	5.21	-0.01	5.21	-521	0.50
Ru	308.71	187.42	183.56	2.06	0.25
	338.00[15]	184.00[15]	467.00[15]	1.78[15]	
Cr	264.33	120.92	183.71	2.19	0.30
$Ru_{48}Cr_{16}$	277.18	67.74	232.02	4.09	0.39
$Cr_{48}Ru_{16}$	333.55	148.91	233.61	2.23	0.35
$Ru_{42}Cr_{16}Mo_6$	293.49	94.52	230.48	3.10	0.35
$Cr_{42}Ru_{16}Mo_6$	303.02	123.07	220.98	2.46	0.32
$Ru_{42}Cr_{16}Mn_6$	256.44	82.96	201.13	3.09	0.35
$Cr_{42}Ru_{16}Mn_6$	249.30	114.87	160.73	2.17	0.35
$Ru_{42}Cr_{16}Fe_6$	245.39	88.06	186.68	2.79	0.32
$Cr_{42}Ru_{16}Fe_6$	253.19	101.91	185.25	2.48	0.32

5.1.3 Elastic moduli of Pure metals, undoped and six X doped $Cr_{48}Ru_{16}$, $Ru_{48}Cr_{16}$ structures, ($X = Fe, Mn$ and Mo)

In Table 5.2 we present the calculated bulk, shear, Young's modulus, the ratio of bulk to shear modulus and Poisson's ratio for the pure metals, the six X ($X = Mn, Fe$ and Mo) doped and undoped $Ru_{48}Cr_{16}$ and $Cr_{48}Ru_{16}$. The trend in bulk modulus of pure metals

increases from Mn to Ru as shown in Table.5.2. The compressibility of the pure material increases in a trend as follows:

$$\text{Mn} < \text{V} < \text{Mo} < \text{Cr} < \text{Ru}.$$

The shear modulus has a robust correlation with the hardness of the material. Ruthenium strikes us as having the highest shear modulus of 187.42 GPa while manganese has the lowest value of -0.01 GPa. However, the pure metals are ductile except manganese. From Table 5.2, it can be seen that the average Young's modulus of $\text{Cr}_{48}\text{Ru}_{16}$ is higher than the $\text{Ru}_{48}\text{Cr}_{16}$ hence $\text{Cr}_{48}\text{Ru}_{16}$ system is stiffer.

The bulk modulus will assist in knowing which materials are more resistant to fracture. The $\text{Cr}_{48}\text{Ru}_{16}$ system has high ability to resist fracture due to its high bulk modulus (333.55 GPa) than $\text{Ru}_{48}\text{Cr}_{16}$ (277.18 GPa) system. In addition the shear modulus helps to determine the material's response to shear stress and it is again found that $\text{Cr}_{48}\text{Ru}_{16}$ (148.91 GPa) system has more ability to resist shear stress than $\text{Ru}_{48}\text{Cr}_{16}$ (67.74 GPa) system.

To determine ductility or brittleness we used the ratio of the bulk to shear modulus under the criterion of Pugh [164] that says a material is ductile when B/G ratio is (greater than 1.75) whilst for low B/G ratio (less than 1.75) is brittle. It is clear in Table 5.2 that $\text{Ru}_{48}\text{Cr}_{16}$ has high B/G ratio of 4.09 than $\text{Cr}_{48}\text{Ru}_{16}$ (2.23), the Ru rich ternary alloy is more ductile and can be able to deform under tensile stress. The Poisson's ratio of Frantsevich et.al [165] suggested that the Poisson's ratio (ν) can be used to indicate ductility or brittleness. If the (ν) > 0.3 it is ductile and otherwise it is brittle. The $\text{A15Ru}_3\text{Cr}$ and

A15Cr₃Ru systems are all ductile; however Ru₄₈Cr₁₆ has higher value of 0.39 than Cr₄₈Ru₁₆ (0.35).

The Young's, shear and bulk modulus of the six X (X=Mo, Mn and Fe) atoms-doped Cr₄₂X₆Ru₁₆ and Ru₄₂X₆Cr₁₆ structures are calculated and analysed. The six Mo atoms-doped Cr₄₈X₆Ru₁₆ have high Bulk of 302.03 GPa whilst Mn has a low bulk modulus of 249.30. A high and low Young's modulus of 220.98 GPa and 160.73 GPa were obtained for six Mo-doped Cr rich and six Mn-doped Cr-rich alloys respectively. Lastly, the six Mo-doped Cr rich have a higher shear modulus of 123.07 GPa whereas the six Fe-atom doped-alloy possess a lowest shear modulus of 101.9 GPa. The trend in decreasing ductility based on B/G for the six X-doped Cr₄₈Ru₁₆ is as follows:

Six Fe-doped > six Mo-doped > six Mn-doped

It is apparent that six Fe-doped Cr rich alloy is the most ductile than those of six Mo-doped and six Mn-doped Cr rich alloys.

The results for the six X atoms-doped Ru₄₂Cr₁₆ in Table 5.2 indicate a decreasing trend in bulk and young's modulus from 6Mo-doped to 6Mn-doped then to 6Fe-doped Ru rich alloys. In addition, the Ru₄₂Cr₁₆Mo₆ has the highest bulk and young modulus of 293.49 GPa and 230.48 GPa whereas the Ru₄₂Cr₁₆Fe₆ has the lowest values (245.39 GPa and 186.68 GPa). The ratio of bulk to shear (B/G) decreasing trend is presented below for six X-doped Ru₄₈Cr₁₆:

six Mo-doped > six Mn-doped > six Fe-doped

Moreover, $\text{Ru}_{42}\text{Cr}_{16}\text{Mo}_6$ is more ductile with a value of 3.10 whereas the six Fe atoms-doped Ru rich alloy possess a low value of 2.79. When comparing the ductility of all the six X-atoms doped $\text{Cr}_{48}\text{Ru}_{16}$ and $\text{Ru}_{48}\text{Cr}_{16}$ systems, we observed that the $\text{Ru}_{48}\text{Cr}_{16}\text{Mo}_6$ as the most ductile structure. Due to lack of experimental data, the elastic constant cannot be compared. It is highly suggested that experimental work should be done in order to verify the theoretical data.

In conclusion, the elastic constants for pure metals were computed and found that ruthenium is very hard with a C_{44} value of 164.20 GPa that compare well with the theoretical data of Popoola et.al [15]. As experimental data is limited, we could not compare the other values from the pure metals. The $\text{Ru}_{48}\text{Cr}_{16}$ structure is more ductile with a B/G value of 4.09 than the $\text{Cr}_{48}\text{Ru}_{16}$ structure with 2.23. All the investigated structures were found to be mechanically stable. The elastic moduli for the doped and undoped structures were computed, and the $\text{Ru}_{42}\text{Mo}_6\text{Cr}_{16}$ was predicted to be the most ductile system with a value of 3.10 whereas $\text{Cr}_{42}\text{Ru}_{16}\text{Mn}_6$ has the lowest value of 2.17. The studied six X atoms-doped structures are predicted to be applicable in high temperature structural applications.

Chapter 6

Conclusion and Recommendations

6.1. Conclusion

By means of First-principles calculations, we have investigated the ground state properties of metallic Cr and Ru, their undoped and transition metal doped A15 Cr₃Ru and A15 Ru₃Cr alloys. Convergence tests for the k-points and kinetic energy cut-off were conducted, and the sufficient parameters were selected. The lattice constants for Cr, Ru, undoped and X-doped Ru₄₈Cr₁₆ and Cr₄₈Ru₁₆ (X = Pt, Mn, Fe, Co, Mo, Re, Pd and Zr) were determined based on the plane-wave pseudopotential DFT method. The equilibrium lattice constants for pure metals, Ru₃Cr and Cr₃Ru were calculated using LDA and GGA functionals, the GGA results are in good agreement with the experimental and theoretical results than the LDA. The unrelaxed and relaxed lattice constants of the X-doped Ru₄₈Cr₁₆ and Cr₄₈Ru₁₆ remained the same because the 2x2x2 supercells were constructed from the optimized A15 Ru₃Cr and A15 Cr₃Ru respectively.

The stability of the studied alloys was investigated based on the heats of formation, density of states and elastic properties. The heats of formation of the Cr₃Ru and Ru₃Cr were found to be positive but very close to zero. These results clearly indicate that the studied binary alloys are unstable. We introduced one to six transition metals X dopant atoms to the 2x2x2 supercells of the A15 Cr₃Ru and Ru₃Cr alloys. The doping effect on the heats of formation of the undoped 2 × 2 × 2 Ru₄₈Cr₁₆ and Cr₄₈Ru₁₆ supercells was

investigated. We considered dopants from the first, second and third row transition metals in the periodic table.

Introduction of 1st row transition metal atom (V, Mn, Fe and Co) has an influence in decreasing the heat of formation of the undoped Ru₄₈Cr₁₆. The Mn and Fe doped alloys yielded negative heats of formation. We observed that values for Cr rich ternaries are lower as compared to the Ru rich ternaries. The X-doped Cr₄₈Ru₁₆ compounds (for all doping concentrations) indicated a decreasing trend in the heats of formation as follows: Fe < Mn < V < Co. Furthermore, Fe doped systems were predicted to be more energetically favorable in all studied configurations. The results predicted the six Fe doped Cr₄₈Ru₁₆ as the most stable structure compared to all the studied first-row transition metal Cr-rich and Ru-rich doped systems.

Similar analysis were conducted on the second row transition metal X (Mo < Zr < Pd) doped Ru₄₈Cr₁₆ and Cr₄₈Ru₁₆ systems. We observed a decrease in the heats of formation for all the studied X (second row) doped Ru₄₈Cr₁₆ and Cr₄₈Ru₁₆ alloys. However, the values for Zr and Pd doped systems remained positive. The study predicted negative heats of formation for Mo-doped Cr-rich and Ru-rich alloys, Mo doped structures are predicted as the only stable structures as compared to all studied second-row transition metal doped structures. The six Mo doped Cr₄₈Ru₁₆ was predicted as the most stable structure among all the studied Mo, Zr and Pd doped systems.

We observed positive heats of formation for the studied third-row transition metal (Pt and Re)-doped Ru₄₈Cr₁₆ and Cr₄₈Ru₁₆ systems, indicating the instability of the alloys. The heats of formation for both the Pt and Re doped Cr₄₈Ru₁₆ showed a regular increase with

increasing dopant concentration. Pt and Re dopants do not enhance the stability of $\text{Ru}_{48}\text{Cr}_{16}$ and $\text{Cr}_{48}\text{Ru}_{16}$ compounds.

Magnetic properties of pure metals, the doped and undoped $\text{Ru}_{48}\text{Cr}_{16}$ and $\text{Cr}_{48}\text{Ru}_{16}$ alloys were investigated. We also looked at the effect of smearing width on the magnetic moment (per unit cell) of one Mn doped $\text{Cr}_{48}\text{Ru}_{16}$ alloy. A decrease in the smearing width leads to an increased accuracy of the magnetic moment. We obtained negative magnetic moments for all the studied concentrations of Zr and Re doped Ru-rich systems whereas the positive values were obtained for Zr, Mo, V, Fe, Co and Re doped $\text{Cr}_{48}\text{Ru}_{16}$ systems. These Zr and Re-doped Cr rich alloys are in total contrast with the Ru-rich results. The computed magnetic moments for X (Zr, Mo, V, Pd, and Re) doped $\text{Cr}_{48}\text{Ru}_{16}$ are higher than the corresponding X doped $\text{Ru}_{48}\text{Cr}_{16}$. The results predicted that Mo doped $\text{Ru}_{48}\text{Cr}_{16}$ would couple anti-ferromagnetically with Cr atom. For Ru rich Mn-doped system, we detected high and low magnetization in one Mn- doped and three Mn-doped systems respectively.

The Mo and Fe doped $\text{Cr}_{48}\text{Ru}_{16}$ compounds substituting Cr atom were predicted to couple ferromagnetically with Ru. The Mn doped $\text{Cr}_{48}\text{Ru}_{16}$ was found to be highly magnetized a moment of $2.001 \mu\text{B}$, which is due to high magnetic value of Mn ($5.0 \mu\text{B}$). Some values of magnetic moments of the pure metals compares well with the experimental values. The Mo and Fe in Mo-doped and Fe-doped $\text{Cr}_{48}\text{Ru}_{16}$ were predicted to couple ferromagnetically with Ru. However, a negative moment of $-0.645 \mu\text{B}$ was calculated for five Fe-doped $\text{Ru}_{48}\text{Cr}_{16}$, an indication that Ru contributed more than Cr and Fe. These results caused an antiferromagnetic coupling between Fe-Cr.

The total and partial densities of states for the Cr, Ru, dopants, doped and undoped $\text{Cr}_{48}\text{Ru}_{16}$ and $\text{Ru}_{48}\text{Cr}_{16}$ were calculated. The bands in all TDOS and PDOS curves are found to overlap at Fermi level, indicating metallic character of all the studied systems. The DOS of metallic Fe and Mn indicated the Fermi energy falling on top of a peak, a clear implication of ductility characteristics. Whereas the Ru DOS curve showed a structural stability features arising from the E_f falling on a pseudogap. The high peak of the metallic Cr is located at ≈ 2.0 eV. The DOS of Cr indicated a higher peak of the valence band as compared to the peaks of the conduction band DOS. From the TDOS and PDOS of metallic Mn, we noted that main peak located at the Fermi level.

TDOS and PDOS curves of the undoped $\text{Cr}_{48}\text{Ru}_{16}$ and $\text{Ru}_{48}\text{Cr}_{16}$ indicated that bands mainly originates from the Cr (3d) and Ru (4d) states, with small contribution from their s and p states. Comparing the DOS curves of the undoped binary alloys, we noted more states in the conduction band TDOS of $\text{Cr}_{48}\text{Ru}_{16}$ than those in TDOS of $\text{Ru}_{48}\text{Cr}_{16}$. The stability is associated with low DOS at the Fermi level. We noted low electron density of states at the Fermi level from the DOS of $\text{Cr}_{48}\text{Ru}_{16}$, however, higher electron density of states were observed near the Fermi level in the DOS of $\text{Ru}_{48}\text{Cr}_{16}$.

We investigated the effect of Mn, Fe, Mo and V dopants on the electronic stability of $\text{Cr}_{48}\text{Ru}_{16}$ and $\text{Ru}_{48}\text{Cr}_{16}$ alloys. The s, p and d states in the PDOS of $\text{Cr}_{42}\text{Ru}_{16}\text{Mn}_6$ shifted to lower energy region as compared to the $\text{Ru}_{42}\text{Cr}_{16}\text{Mn}_6$. All the DOS of X doped $\text{Ru}_{48}\text{Cr}_{16}$ compounds displayed high DOS around the E_f whilst X doped $\text{Cr}_{48}\text{Ru}_{16}$ has low DOS. There was no peak in the conduction band DOS and PDOS curves of the Mo-doped Ru rich alloy. On the other hand, the energy difference between the main peak of valence band and that of conduction band in the TDOS of $\text{Cr}_{42}\text{Ru}_{16}\text{Mo}_6$ was found to be 3.6 eV.

The conduction band from all the DOS of $\text{Ru}_{42}\text{Cr}_{16}\text{Mo}_6$ was found to be narrower than the DOS of the studied X-doped materials. In both configurations of Mo-doped systems, most of electrons are accumulated in the lower energy region as compared to Mn and Fe-doped systems. These findings indicated a higher level of electronic stability for Mo-doped systems.

The elastic constants, bulk, shear, Young's moduli for the pure metals, the doped and undoped $\text{Ru}_{48}\text{Cr}_{16}$ and $\text{Cr}_{48}\text{Ru}_{16}$ were calculated. The elastic constant C_{44} is smaller than the C_{11} and C_{12} in all the studied structures.

The values of C_{11} , C_{12} and C_{44} for the undoped Ru-rich alloys are higher as compared to Cr-rich binary alloys. The hardness of the material can be determined from the value of C_{44} elastic constant. The higher value of C_{44} for $\text{Cr}_{48}\text{Ru}_{16}$ alloy indicated that the material is harder than the $\text{Ru}_{48}\text{Cr}_{16}$ and it has strong ability in resisting shear distortion. The $\text{Cr}_{48}\text{Ru}_{16}$ system has high ability to resist fracture due to its high bulk modulus than $\text{Ru}_{48}\text{Cr}_{16}$ system.

From the elastic constants of the $\text{Cr}_{48}\text{Ru}_{16}$ and $\text{Ru}_{48}\text{Cr}_{16}$ alloys doped with six X-atoms (X = Fe, Mn and Mo) alloys, we noted that the C_{11} and C_{44} and C_{66} increased from X (X=Mn, Mo) doped $\text{Ru}_{48}\text{Cr}_{16}$ to $\text{Cr}_{48}\text{Ru}_{16}$ system. The overall comparison predicted that six Mo-doped $\text{Cr}_{48}\text{Ru}_{16}$ can resist shear distortion more than all studied six X atoms-doped Cr rich and Ru-rich alloys. All the structures are mechanically stable according to Bohr mechanical stability criterion for cubic compounds. Among the X-doped Cr-rich systems, the $\text{Cr}_{42}\text{Ru}_{16}\text{Mo}_6$ exhibit the highest shear modulus (303 GPa) and Young's modulus (123 GPa), while $\text{Ru}_{42}\text{Cr}_{16}\text{Mo}_6$ possess the largest shear modulus (230 GPa).

The Cauchy (C_{12} - C_{44}) was used to describe the angular character of atomic bonding in metals. To explore the ductility or brittleness of the material, we referred to the Cauchy pressure and the ratio of bulk to shear modulus. By analyzing the Cauchy pressure, the ratio of bulk modulus to shear modulus, we found that the ductility of X-doped follow the orders of $\text{Cr}_{48}\text{Ru}_{16} < \text{Ru}_{48}\text{Cr}_{16}$, $\text{Cr}_{42}\text{Ru}_{16}\text{Mn}_6 < \text{Cr}_{42}\text{Ru}_{16}\text{Fe}_6 < \text{Cr}_{42}\text{Ru}_{16}\text{Mo}_6$, and $\text{Ru}_{42}\text{Cr}_{16}\text{Fe}_6 < \text{Ru}_{42}\text{Cr}_{16}\text{Mo}_6 < \text{Ru}_{42}\text{Cr}_{16}\text{Mn}_6$.

In summary, we have investigated the effect of transition metal dopants on the structural, thermodynamic, electronic and elastic properties of A15 Cr_3Ru and A15 Ru_3Cr alloys. At first, we successfully used DFT methods to predict the stability based on the heats of formation. The results predicted the $\text{Cr}_{42}\text{Ru}_{16}\text{Mo}_6$, $\text{Cr}_{42}\text{Ru}_{16}\text{Fe}_6$ and $\text{Cr}_{42}\text{Ru}_{16}\text{Mn}_6$ as the more stable structures. Moreover, the results predicted the $\text{Cr}_{42}\text{Ru}_{16}\text{Mo}_6$ as the most stable structure among all the studied structures. In general, the calculated density of states reported metallic behaviour for pure metals and their alloys. The TDOS and PDOS confirmed the stability of Fe-doped, Mo-doped and Mn-doped Cr-rich and Ru-rich alloys. Finally, the elastic properties calculations revealed both the studied Ru-rich and Cr-rich ternaries as mechanically stable structures. These study show that Mn, Fe and Mo dopants play an important role in improving the properties of metal alloys. We conclude that the $\text{Cr}_{42}\text{Ru}_{16}\text{Mo}_6$, $\text{Cr}_{42}\text{Ru}_{16}\text{Fe}_6$ and $\text{Cr}_{42}\text{Ru}_{16}\text{Mn}$ be considered for high temperature applications.

6.2. Recommendation

The heats of formation for $\text{Cr}_{48}\text{Ru}_{16}$ doped with one to six atoms of Re, Pd, Zr and V were predicted as unstable, however the values were positive but very close to zero. We recommend that additional stability tests be conducted on $\text{Cr}_{48}\text{Ru}_{16}$ with higher concentration of dopants (Re, Pd, Zr and V). Different alloy compositions may be beneficial in tuning the performance and the stability of the materials earmarked for high temperature structural applications. Molybdenum (Mo)-doped Cr rich alloys were found to be stable among all the studies configurations. We suggest complete theoretical analysis of the doping effect Niobium (Nb), Technetium (Tc) and Tungsten (W) on the ground state properties of $\text{Cr}_{48}\text{Ru}_{16}$ and $\text{Ru}_{48}\text{Cr}_{16}$. The Nb, Tc and W metals are located on the immediate left, right and below the Mo in the periodic table respectively. The results can have a huge impact on our scientific understanding of the effect of metal dopants (from the same row/column) on the stability of the materials. Exploration of non-metallic dopants is a topic for future work. Due to lack of availability of experimental results, we recommend that stability experiments be conducted for comparison and to develop a deeper understanding.

REFERENCES

- [1] F. Pettit ., Oxid Met., **76**, 1 (2011).
- [2] C.T. Sims., J.Met., **15**, 127-132 (1963).
- [3] I. Gurrappa., surface and coat. Technol., **139**, 272 (2001).
- [4] T.J. Carter, engineering failure analysis., **12**, 237 (2005).
- [5] J.T. DeMasi-Marcin and D. K., Gupta, surface and coatings technology., **68-69**, 1 (1994).
- [6] B.M. Warnes and D.C. Punola, Surf. Coat. Technol., **95**, 1 (1997).
- [7] R.C. Reed, The superalloys: Fundamentals and application, New York, Cambridge University, 1 (2006).
- [8] M. M. Tibane, PhD thesis, University of Limpopo, South Africa, (2011).
- [9] T. Sasaki; T. Mukai and K. A. Hono, Scr. Mater., **189 -192**, 57, (2007).
- [10] L. Glaner, A. Douglas, and S.N. Prins, “Platinum-based alloys for high temperature and special application” 329-336 (2004).
- [11] M. Segersall, Nickel-based single-crystal superalloys, PhD thesis, **1568** (2013).
- [12] N.B. Maledi, “corrosion behavior of Pt-based super-alloys intended for high temperature applications (2007).

- [13] L.A. Cornish and L.H. Chown, "Platinum-based alloys and coating: Material for the future (2009).
- [14] L.A. Cornish, R. Suss, R. Volkl, M. Wenderoth, S. Vorberg, B. Fischer, U. Glatzel, A. Douglas, L.H. Chown, T. Murakumo, J. Preussner, D. Lupton, L. Glaner, N.B. Maledi, J.H. Potgieter, M. Sephton, and . Williams, "Overview of the development of new Pt-based alloys for high temperature application in aggressive environments," 697-711 (2007).
- [15] A.I. Popoola, PhD Thesis, University of Witwatersrand (2013).
- [16] M.B. Shongwe, M. J. Witcomb, L. A. Cornish, and M.J. Papo, "TEM studies of Pt-Al-Cr-Ru alloys," **7**, 12-14 (2012)
- [17] H. Service, B. I. M. Wolff, and P.J. Hill, "Platinum metals-based intermetallic 4, 158-166 (2000).
- [18] J. K. Odusote, L. A. Cornish, and J. M. Papo, "High temperature oxidation of Pt-Al-Cr-Ru alloy: Scale morphology and adherence," 142-149 (2012).
- [19] R. Suss, L. A. Cornish, and M. J. Witcomb, "Investigation of as-cast alloys in the Pt-Al-Cr system, **490**, 124-144 (2010).
- [20] M. C. Gao, Y. Suzuki, H. Schweiger, O. N. Dogan, J. Hawk and M. Widom, Phase stability and elastic properties of Cr-V alloys, *J. Phys. Condens. Matter* **25**, 075402 (2013).
- [21] Q. Feng, T. K. Nandy, L.J. Rowland, B. Tryon, D. Banerjee and T. M. Pollock, TMS superalloys (2004).

- [22] L. A. Cornish, R. Suss, A Watson and S. N. Prins, building a database for the prediction of phases in Pt-based superalloys 91-102 (2006).
- [23] B. M. Venkatraman, and J. P. Newmann, "The Cr-Ru (Chromium-Ruthenium) system **8**, 109-112 (1987).
- [24] L. k. Bernard, Journal of propulsion and power, 20, (2004).
- [25] J.B. Esgar and R. A. Reynolds, technology evaluation report on AGARD conference proceedings 73, (1971).
- [26] L.A. Cornish, R. Suss., L. H., S. Taylor., L. Glaner, A. Douglas and S. N. Prins. International platinum conference "platinum adding value": The South African Institute of Mining and metallurgy, (2004).
- [27] D. Papamoschou, Journal of Propulsion and Power., **20**, 2 (2004).
- [28] G.W. Meetham Materials & Design., **9**, 213 (1988).
- [29] M.P. Boyce, Elsevier, Gas Turbine Engineering Handbook, 3d edn., Burlington USA, 15.
- [30] J.T. DeMasi-Marcin and D. K., Gupta, surface and coatings technology., **68-69**, 1 (1994).
- [31] D.R. Clarke and S.R. Phillpot, Materials Today., **8**, 22 (2005).
- [32] N. Saunders and A.P. Miodownik, "CALPHAD comprehensive guide", ed RW Cahn, Pergamon (1998).

- [33] L. Kaufman and H. Bernstein, computer calculation of phase diagrams, New York, Academic press (1970).
- [34] K. Oikawa, G.W. Qin, T. Ikeshoji, O. Kitakami, Y. Shimida, K. Ishida, K. Fukamichi, J. Magnet. Magnet. Mater., **236**, 220 (2001).
- [35] R.M. Waterstrat, Metall.Trans., **4**, 1585 (1973).
- [36] E. Raub, W. Mahler, Z. Metallkd., **46**, 210 (1955).
- [37] L. Muller, Ann.Phys., **7**, 9 (1930).
- [38] E. Friederich and A. Kussman: Phys. Z., **36**, 185 (1935).
- [39] E. Gebhart and W. Koster: Z. Metallkd., **32**, 253 (1940).
- [40] E. Raub and W. Mahler: Z. Metallkd., **32**, 262 (1940).
- [41] S.J. Pickart and R. Nathans: J. Appl. Phys., **34**, 1203 (1963).
- [42] M.J. Besnus and A.J.P. Meyer: Phys. Status Solidi (B) **58**, 533 (1973).
- [43] T. B. Massalski. Binary phase diagrams, ASM, Ohio, USA. (1990).
- [44] A.K. Butylenko and V.V. Nevdacha, Dop. Akad. Nauk. Ukr. RSR A., Fiz.-Mat.Tekh., **42**, 66 (1980).
- [45] A. Kussman, K. Muller and E. Raub, Z. Metallkd, **59**, 859 (1968).
- [46] A. Oles and A. Bombik, Phys. Status Solidi(b), **92**, K81 (1979).
- [47] P.J. Spencer, Noble Metal Database, Spencer Group Inc, (1996).
- [48] T.B. Massalski, Binary alloy phase diagrams, ASM International, (1990).

- [49] T.B. Massalski: Binary Alloy Phase Diagrams, 2nd ed., ASM, Materials Park, OH, 27 (1992).
- [50] W. Wopersnow, ch.J. Raub, Metall Berlin., **33**, 1261 (1979).
- [51] B.T. Matthias, T.H. Geballe, V.B. Compton, E. Corenzwit and G.W. Hull, J. Phys Rev., **128**, 588 (1962).
- [52] E. Raub and W. Mahler, Z. Metallkd., **46**, 210 (1955).
- [53] P. Greenfield and P.A. Beck, Trans. AIME., **206**, 265 (1956).
- [54] R.M. Waterstrat and J.S. Kasper, Trans. AIME., **209**, 872 (1957).
- [55] R.M. Waterstrat, J. less-Common Met., **80**, 31 (1981).
- [56] E.M. Savitski, V.F. terekhova and N. A. Birun, Russ. J. Inorg. Chem., **6**, 1002 (1961).
- [57] A.K. Shurin and G.P. Dmitrieva, Inst. Metallofiz. Akad. Nauk. Ukr. SSR, **18**,170 (1964).
- [58] F.A. Shunk: Constitution of Binary Alloys. 2nd ed., McGraw-Hill, New York, NY, **278** (1969)
- [59] Y. F. Gu, H. Harada, Y. Ro and T. Kobayashi, Met. and Mat. Trans., 36A, 578 (2005).
- [60] J.J. Lagowski (Ed.). Chemistry Foundations and Applications. Thomson Gale, NewYork, (2004).
- [61] R. David. Handbook of Chemistry and Physics. CRC Press, New York, (2008).

- [62] G.V. Samsonov (Ed.). Handbook of the physicochemical properties of the elements. IFI-Plenum, New York, USA, (1968).
- [63] G.W.C. Kaye and T.H. Laby. Tables of physical and chemical constants. Longman, London, 1993.
- [64] A.H. Sully, Metallurgy of the rarer Metals-1. Chromium 1st ed, Butterworths scientific Publications, London, (1954).
- [65] M. H. Tsai and K. C. Hass. Phys. Rev B., **51**, 14616 (1995).
- [66] Rhodium. www.periodic.lanl.gov. Accessed December., (2010).
- [67] H. K. Zhang and L. L. Chen. Phase diagram of palladium-rich region in Nd-Pd-Ru ternary system, precious metals., **18**, 4 (1997).
- [68] H. A. (ed). Metals in the environment. Academic press Inc., London (1980).
- [69] F. R. (ed). Siegel. Review of research on modern problems in geochemistry. Earth science.,**16**, united nations educational, scientific and cultural organisation.
- [70] Y. Matsumoto, J. Fukumori, M. Moringa, M. Furui and T. Sakaki Scr.mater., **34**, 1685 (1996).
- [71] L.E. Toth, Transition Metal Carbides and Nitrides Academic Press, New York (1971) E.K. Storms The Refractory Carbides Academic Press, New York (1967).
- [72] T. Muroga et. al. Journal of nuclear material 547-554 (2002).
- [73] V.P. Zhukov, V.A. Gubanov, O. Jepsen, N.E. Christensen, O.K. Anderson J. Phys. Chem. Solids., **49**, 841 (1988).

- [74] V.P. Zhukov, V.A. Gubanov, G.G. Mikhailov, G.P. Shveikin Sov. Powder Metall. Met. Ceram., **27**, 329 (1988).
- [75] V. O. Kharchenko and D. O Kharchenko, condensed matter physics., **16**, 1 (2013).
- [76] R. Callaghan, Zirconium and Hafnium statistics and information, (2008).
- [77] O. Levy, M. jahnatek, V. Roman, C. Gus L. W. Hart and S. Curtarolo, J. AM. CHEM. SOC. (2010).
- [78] S. Ali, I. Yaseen and R. Ubic, materials research lab, institute of physics and electronics, university of Peshawar, Pakistan Boise state university, Idaho, USA.
- [79] R.A. Higgins, E. Arnold, Engineering Metallurgy: Part 1 Applied Physical Metallurgy, 1993.
- [80] N. Viswanadham, R. Kamble, A. Sharma, M. Kumar, A.K. Saxena, J.Mol. Catal. A: Chem. **282**, 74-79 (2008).
- [81], A.V. Naumov ,Russian Journal of non-ferrous metals 48, 418-423 9 (2007).
- [82] D.R. Lide, CRC Handbook of chemistry and physics **11**, 87-88 (2006).
- [83] R.C. Reed, A.C. Yeh, S.S. Babu, M.K. Miller, Scripts Materialia **51**, 327-331 (2004).
- [84] K.E. Yoon et al Acta Materialia **55**, 1145-1157 (2007).
- [85] Davis, R. Joseph, heat resistant material 365 (1997).
- [86] A. Holleman, F. Wiberg, Egon. Inorganic chemistry 1384 9 (2001).

- [87] B. Shedd, Kim. Commodity Report: Cobalt United States geological Survey (2008).
- [88] B. lee, R. Alsenz, A. Ignatiev, M. van Hove and A. M. Van Hove, Phys. Rev **B17**, 1510 (1978).
- [89] Properties and facts for cobalt. American elements, retrieved (2008).
- [90] R.N. Jarrett, J.P. Collier and J.K. Tien, effects of Cobalt on the hot workability of nickel-base super-alloys 455-466 (1984).
- [91] B.L. Bramfitt, Benscoter, Arlan O. The Iron Carbon phase diagram 24-28 (2002).
- [92] G. Rugel, T. Faesetermann, K. Knie, G. Korschinek, M. Poutivtsev, D. Schumann, Kivel, N. G. leopard, I. R. Weinreich, Wohlmuther, M. Phys. Rev **103** (2009).
- [93] E. Fawcett, Spin-density-wave antiferromagnetism in chromium". **60**, 209 (1988).
- [94] http://www.efunda.com/processes/heat_treat/introduction/heat_treatment.cfm.
- [95] http://www.efunda.com/processes/heat_treat/softening/annealing.cfm.
- [96] http://www.efunda.com/processes/heat_treat/hardening/direct.cfm.
- [97] Effects of Alloying Elements <http://www.primosknives.com/articles/alloys.htm>.
- [98] D. R. Lide, CRC Handbook of Chemistry and Physics (2005).
- [99] CASTEP Users Guide, San Diego: Accelrys Inc., (2001).
- [100] P. Hohenberg and W. Kohn, Phys. Rev., **136**, 864 (1964).
- [101] W. Kohn and L.J. Sham, Phys. Rev., **140**, A1133 (1965).
- [102] J. Harris and R.O. Jones, J. Phys., F4, 1170 (1974).

- [103] O. Gunnarsson and B.I. Lindqvist, Phys. Rev. B., **3**, 4174 (1976).
- [104] A.D. Becke, Phys. Rev. A., **38**, 3098 (1998).
- [105] D.M. Ceperley and B. J. Alder, Phys. Rev. Lett., **45**, 566 (1980).
- [106] J.P. Perdew, J. A. Chevary, S. H. Vosko, K. A. Jackson, M. R. Pederson, D. J. Singh, and C. Fiolhais, Phys. Rev. B., **46**, 6671 (1992).
- [107] A.D. Becke, J. Chem. Phys., **96**, 2155 (1992), **97**, 9173 (1992).
- [108] P. Hohenberg and W. Kohn, Phys. Rev. **136**, 864 (1964), W. Kohn and L. J. Sham, *ibid.*, **140**, 1133 (1965).
- [109] C. Lee, W. Yang, and R. G. Parr, Phys. Rev. B., **37**, 785 (1988).
- [110] J.P. Perdew and Y. Wang, Phys. Rev. B., **45**, 13244 (1992).
- [111] S. Clark, Complex Structure in Tetrahedral Semiconductors. PhD Thesis, University of Edinburgh, (1994).
- [112] C. Rostgaard. The Projector Augmented-wave Method. www.arxiv.org. Accessed 10 (2012).
- [113] E. Fermi, "Sopra lo spostamento per pressione delle righe elevate delle serie spettrali," Nuovo Cimento., **11**,157 (1934).
- [114] M.C. Payne, M.P. Teter and D.C. Allan, T.A. Arias and J.D. Joannopoulos, Rev. Mod. Phys., **64**, 1045 (1992).
- [115] M.J. Phasha, MSc dissertation, University of Limpopo (2005).
- [116] H.R. Chauke, PhD Thesis, University of Limpopo (2005).

- [117] P.B. Semalty, J. Alloys Compound **419**, 1 (2006).
- [118] K.L. Ng and Q.P. Sun, Mechanics of Materials **38**, 41 (2005).
- [119] A.E. Mattsson, P.A. Schultz, M.P. Desjarlais, T.R. Mattsson and K. Leung, Modelling Simul. Mater. Sci. Eng., **13**, R1 (2005).
- [120] L.P. Bouckaert, R. Smoluchowski, and E. Wigner. The theory brillioun zones and symmetry properties of wave functions in crystals. Phys. Rev., **50**, 50 (1936).
- [121] H.J. Monkhorst and J. D. Pack, Special points for the brillouin zone integrations, phys.rev. B., **13** 5192 (1976).
- [122] R.M. Martin, Cambridge University Press, UK (2004).
- [123] A. Balereschi, Phys. Rev. B., **7**, 5212 (1973).
- [124] S. Froyen, Phys. Rev. B., **39**, 3168 (1989).
- [125] D. Vanderbilt, Phys. Rev. B., **41**, R7892 (1990).
- [126] J.S. Lin, A. Qteish, M.C. Payne and V. Heine, Phys. Rev. B **47**, 4174 (1993).
- [127] S. Hong and C.L, Fu, Intermetallics, **7**, 6 (1999).
- [128] M.J. Mehl and D.A. Papaconstantopoulos, Phys. Rev. B, **54**, 4523 (1996).
- [129] P. Villars and L.D. Calvert, Pearson's Handbook of crystallographic Data for intermetallic phases **3**, 2162 (1985).
- [130] P. Villars, L.D. Calvert, Pearson's Handboook of Crystallographic Data for intermetallic phases **2**, 1736 (1985).

- [131] P. Villars and L.D. Calvin, Pearson's Handbook of crystallographic data for intermetallic phases, 1-3 (1985).
- [132] H.J. Monkhorst and J. D. Pack. Special points for the brillouin zone integrations, *phys.rev. B.*, **13**, 5192 (1976).
- [133] I. Papadimitriou, C. Utton, A. Scott and P. Tsakirooulos, *metallurgical and materials transactions*, 46 566-576 (2015).
- [134] S. Chelli, S Touam, L Hamjoud, H Meradji, S Ghemid and F El Haj Hassan, *Mater. Sci*, **33**, 880 (2015).
- [135] L.I. Schiff, *Quantum Mechanics*. McGraw-Hill. p. 440 (1968).
- [136] R. Shankar, *Principles of Quantum Mechanics*. Plenum_Press. pp. 398–400. ISBN 0306403978 (1980).
- [137] H. Adachi and H. Ino, *Nature.*, **401**, 148 (1999).
- [138] B. Wang and S.T. Pantelides, *Phys. Rev.*, **86**, 165438 (2012).
- [139] M.C. Gan, Y. Suzuki, H. Schweiger, O.N Dogan, J. Hawk and M. Widom, *J. Phys.:Condens. Mater* **25**, 075402 (2013).
- [140] Y Mao, J Yuan and J Zhong, *J.Phys.,Condens. Matter* **20**, 115209 (2008).
- [141] G. S. Neumann and L. Stixrude, *Phys.Rev B*, **60**, 791 (1999).
- [142] H.P. Meyer.W. Sucksmith, *Proc. R. Soc. London, Ser. A* **207**, 427 (1963).
- [143] G.L. High, H.L. Alberts and P.Smit, *Journal of magnetism and magnetic material*, **78**, 384-386 (1989).

- [144] H.C. Kandpal, G.H. Fecher and C.Felser. *J.Phys.*, **40** 1507-1523 (2007).
- [145] M. Shiga, *journal of the physical society of japan*, **22**, 539-546 (1967).
- [146] T. Moriya, *progress of theoretical physics*, **23**, 157-183 (1965).
- [147] R.B Patel, A. J. Liddiard and M. D. Crapper, *J. Phys.:Condens. Matter* **6**, 9973-9979 (1994).
- [148] T. Hong, T.J.W. Yang, X.Q. Guo, A.J. Freeman, T. Oguchi and J.H. Xu. *Phys. Rev.B*, **43**, 1940 – 1947 (1991).
- [149] J.H. Xu and A.J. Freeman. *Phys. Rev. B*, **41**:12553 – 12561 (1990).
- [150] J.H. Xu, T. Oguchi and A. J. Freeman. *Phys. Rev. B*, **36**:4186 – 4189 (1987).
- [151] P. Ravindran and R. Asokamani. *Bull. Mater. Sci.*, 20:613 – 622 1997.
- [152] M.E. Eberhart, D.P. Clougherty and J.M. Maclaren. *J. Mater. Res*, **8**, 438 – 448 (1993).
- [153] P.W. Thrush. *A Dictionary of Mining, Mineral, and Related Term*. U.S. Dept. Interior Bur. Mines Washington D.C, (1968).
- [154] R.L. Bates and J.A. Jackson. *Glossary of Geology*. American Geol. Inst, (1980).
- [155] R.J. Goble and S.D. Scott. *Canadian Minerologist*, **23**, 273 – 285 (1985).
- [156] Dmitri Kopeliovich. *Hardness test methods*. www.substech.com. Accessed May 8, (2012).
- [157] M. Hebbache. *Sol. St. Commun.*, **113**, 427 – 432 (2000).
- [158] Li, Xiaoqing, H. Zhang, Lu. Song Wei Li, Jijun Zhao, B. Johansson and L. Vitos. *Phys.Rev*, **86**, 014105 (2012).

- [159] E. Ateser, H. Ozisik, K. Colakoglu , E. Deligoz, *com.mat.sci*, **50**, 3208-3212 (2011), H. Ozisik, E. Deligoz, K. Colakoglu, Y.O. Ciftci, *com.mat.sci*, **50**, 1057-1063 (2011).
- [160] D.C. Wallace, *Thermodynamics of crystals*, Wiley, New York, (1972).
- [161] D. Pettifor, *Mater. Sci. Technol.*, **8**, 345 (1992).
- [162] H. Koc, Anirullah M. mamedov, E. Deligoz and H. Ozisik, *Condensed matter*, 1-17 (2012).
- [163] H Wu, T. H. Wu, T. Yildirim, and W. Zhou, *J. Phys. Chem. Lett.*, **4**, 925-930 (2013).
- [164] S.F Pugh, *Philos. Mag.* **45**, 823 (1954).
- [165] I.N. Frantsevich, F.F. Voronov and S.A. Bokuta, *Elastic constants and elastic moduli of metals and insulators Handbook*, 60-180 (1983).